



LUND UNIVERSITY

Development of Magnetomotive Ultrasound Imaging

Evertsson, Maria

2016

Document Version:

Publisher's PDF, also known as Version of record

[Link to publication](#)

Citation for published version (APA):

Evertsson, M. (2016). *Development of Magnetomotive Ultrasound Imaging*. [Doctoral Thesis (compilation), Department of Biomedical Engineering].

Total number of authors:

1

General rights

Unless other specific re-use rights are stated the following general rights apply:

Copyright and moral rights for the publications made accessible in the public portal are retained by the authors and/or other copyright owners and it is a condition of accessing publications that users recognise and abide by the legal requirements associated with these rights.

- Users may download and print one copy of any publication from the public portal for the purpose of private study or research.
- You may not further distribute the material or use it for any profit-making activity or commercial gain
- You may freely distribute the URL identifying the publication in the public portal

Read more about Creative commons licenses: <https://creativecommons.org/licenses/>

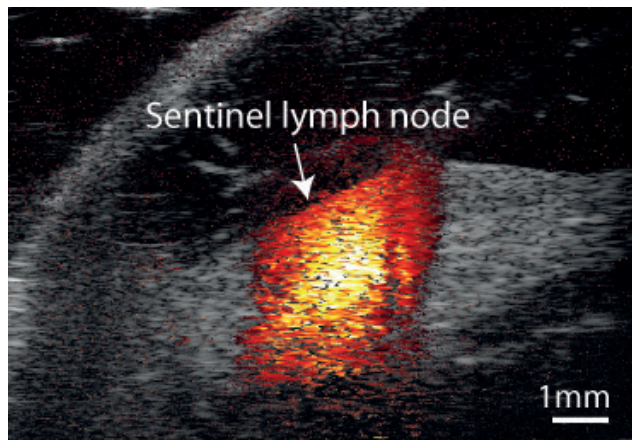
Take down policy

If you believe that this document breaches copyright please contact us providing details, and we will remove access to the work immediately and investigate your claim.

LUND UNIVERSITY

PO Box 117
221 00 Lund
+46 46-222 00 00

Development of Magnetomotive Ultrasound Imaging



Maria Evertsson

Department of Biomedical Engineering
Faculty of Engineering
Lund University

Development of Magnetomotive Ultrasound Imaging

Maria Evertsson



LUND
UNIVERSITY

DOCTORAL DISSERTATION
by due permission of the Faculty Engineering, Lund University, Sweden.
To be defended in E:1406, Ole Römers väg 3, Lund, on April 22 at 09:15.

Faculty opponent
Dr Helen Mulvana

School of Engineering, University of Glasgow, Scotland

Organization: Lund University Department of Biomedical Engineering P.O. Box 118, SE-221 00 Lund, Sweden	Document name: Doctoral Dissertation
	Date of issue: April 22, 2016
	Sponsoring organization: The Kamprad Family Foundation and The Swedish Research Council
Author: Maria Evertsson	
Title: Development of Magnetomotive Ultrasound Imaging	
Abstract: <p>The earlier abnormalities coupled with disease can be discovered in the body, the larger is the chance to survive the disease. Molecular imaging is a growing research field which aims to detect these abnormalities at a molecular level, when the chance of survival is still high. The main idea of molecular imaging is to use target specific contrast agents that accumulate at the diseased region at a detectable concentration. Nanoparticles have shown to be very suitable as molecular imaging contrast agents due to their small size, which enable them to cross biological barriers and to bind to the biological entity of interest.</p> <p>In this thesis has the potential of magnetomotive ultrasound (MMUS), a new ultrasound imaging technique which enables detection of superparamagnetic iron oxide nanoparticles (SPIONs), been examined. Nanoparticles are too small to be detected with conventional ultrasound since their small size make them unable to backscatter ultrasound at a detectable level. Instead, MMUS imaging makes profits of the induced movement, created when a time-varying magnetic field is applied to a sample containing SPIONs. As the particles start to move, their surrounding will move and ultrasound is used to detect this motion.</p> <p>In the first study (paper I), was a frequency and phase tracking MMUS algorithm developed. The algorithm is able to filter out the nanoparticle movement from other artifactual movements and the location of the nanoparticles may then be revealed. To evaluate the potential of the developed algorithm, phantom studies (paper I, II and IV) were performed. Different parameters such as the nanoparticle concentration and the magnetic field frequency were altered in order to examine their impact on the magnetomotive displacement. Simulations were performed, where models of experimental setups were created. The results from the simulations were verified with the experimental findings (paper II and IV) and a good agreement was found.</p> <p>Moreover, to evaluate the potential of MMUS to be used in health care, animal studies have been performed (paper III, V and VI). In this thesis, the MMUS technique was evaluated in a clinical relevant model, where SPION-laden sentinel lymph nodes (SLNs) in rats were imaged. In this model MMUS was thought to serve as a complementary imaging modality to standard methods, providing high-resolution bedside surgical guidance during SLN surgery in breast cancer or malignant melanoma. In order to test the model in a clinical scenario, prestage of the SPION-laden SLNs was done with MRI or PET (paper III and VI, respectively), thereafter MMUS imaging was performed.</p> <p>The results, both from the phantom and the animal studies, have shown to be very promising. Displacement in the sub-micrometer range has been detected in all studies. Although displacement artifacts have been more than two orders of magnitudes larger than the MMUS signal, the algorithm has been able to provide a clear representation of the location of the SPION-laden regions (e.g. paper III and V). This indicates that the MMUS technique has potential for future clinical use.</p>	
Keywords: Magnetomotive ultrasound, molecular imaging, contrast agents, multimodal imaging, sentinel lymph node	
Classification system and/or index terms:	
Supplementary bibliographical information: ISRN: LUTEDX/TEEM - 1103 – SE Report nr: 4/16	
ISSN and key title:	
Recipient's notes:	Number of pages: 123
	Price:
Security classification:	

I, the undersigned, being the copyright owner of the abstract of the above-mentioned dissertation, hereby grant to all reference sources permission to publish and disseminate the abstract of the above-mentioned dissertation.

Signature:

Date: 2016-03-15

To my family

Cover illustration

Magnetomotive ultrasound image of a superparamagnetic iron oxide nanoparticle (SPION) laden sentinel lymph node (Study VI).

Public defence

April 22, 2016, 09.15 in E:1406, E-huset, Faculty of Engineering, LTH

Advisors

Associate Professor Tomas Jansson

Associate Professor Magnus Cinthio

Professor Hans W Persson

Lund University, Sweden

Faculty Opponent

Dr Helen Mulvana

School of Engineering James Watt South Building University of Glasgow, Scotland

Board of Examination

Professor Olof Lindahl

Department of Radiation Sciences, Biomedical Engineering, and the Centre for Biomedical Engineering and Physics, Umeå University, Sweden

Professor emeritus Dick Killander

Department of Oncology, Institute of Clinical Sciences Lund University, Sweden

Associate Professor Sigrid Leide Svegborn

Medical Radiation Physics, Malmö, Lund University, Sweden

Deputy members

Associate Professor Nina Reistad

Atomic physics, Faculty of Engineering, LTH, Lund University, Sweden

Associate Professor Dmitry Grishenkov

Technology and Health, Royal Institute of Technology, Stockholm, Sweden

Chairman

Associate Professor Johan Nilsson

Department of Biomedical Engineering, Faculty of Engineering, LTH, Lund University, Sweden

ISBN: 978-91-7623-745-8 (printed version)

ISBN: 978-91-7623-746-5 (electronic version)

Report nr: 4/16

ISRN: LUTEDX/TEEM - 1103 – SE

Printed in March 2016 by Tryckeriet i E-huset, Lund, Sweden

© 2016 Maria Evertsson, except where otherwise stated

ACKNOWLEDGMENTS

First of all I would like to thank my main supervisor Tomas Jansson for guiding me through the research world during my time as a PhD student. Thank you for sharing your knowledge, for your encouragement and support, for your enthusiasm, for your caring and understanding, for your sense of humour and for your ability to be accurate and to “vrida och vända på varje ord” (even if I not always seem to appreciate it at that precise moment). I would also like to give a special thanks to my co-supervisor Magnus Cinthio. Thank you for your support, for your help, for your encouragement, for your kindness and caring and for pushing me to summarize the most important things in a paper in one sentence. I have learned a lot from both of you and I see you not only as my supervisors but also as good friends. I am very grateful that I have had you by my side these years!

A special thanks also to my roommates; Tobias Erlöv and John Albinsson, which I have spent most time together with during these years. Thank you for your friendship, for your help, and for all discussions. I have really enjoyed your company, both in office and during our conference trips, and I am glad that I have had the opportunity to share my PhD-time together with you! Thank you also Simon Segstedt, I really enjoyed the “veckans YouTube-klipp” –time together with you and hope to see you here soon again. Thank you Roger Andersson for your optimism and your ability to always see things from the bright side. I am happy that you have joined the MMUS project and that I have the opportunity to collaborate with you. I also wish to thank Hans W Persson and Monica Almqvist for your help, valuable comments, and for sharing your ultrasound knowledge during these years.

Many thanks also to Pontus Kjellman, Sarah Fredriksson, René in't Zant, Hanna Toftevall and Sven-Erik Strand, for good collaborations and for always answering my never ending questions.

Thanks to Anders Wahlström and Göran Nybom for all your various magnetic field generating constructions. To Gustav Grafström and Thuy Tran for your help with the PET measurements. To Esayas Atile, Malin Eriksson and Stina Andåker for doing their master thesis within this MMUS project, contributing to my research.

Many thanks also to all my other colleagues at the department, for contributing both with knowledge and help whenever I have been in need of it, and for creating a nice atmosphere, making it fun to go to work!

I would also like to take the opportunity to thank my family, relatives and friends for enriching my life.

A special thanks to my Mum and Dad for your love, your support and for believing in me. And also to my brother Mikael for always being by my side. I am very thankful that I have you as my brother!

Finally, I would like to thank my beloved husband Pontus and our wonderful son Edvin. Thank you both for all your love, for lighting up my life and for bringing me a lot of joy!

The work in this thesis has been sponsored by the Kamprad Family Foundation, VINNOVA, The Swedish Research Council, The Knut and Alice Wallenberg foundation, The Royal Physiographic Society in Lund and The IEEE UFFC society.

POPULÄRVETENSKAPLIG SAMMANFATTNING

Ju tidigare man kan upptäcka sjukdomskopplade förändringar i kroppen, desto större är chansen att bli frisk och överleva sjukdomen. Molekylär avbildning är ett nytt forskningsfält som vuxit fram de senaste årtiondena som svarar mot detta önskemål. Målet är att så tidigt som möjligt kunna avbilda de förändringar som ger upphov till sjukdomen, snarare än att som idag, avbilda effekterna av dem (t ex förändringar i anatomi eller i blodflöde). Målsökande molekyler, så som exempelvis antikroppar, binds in till ett kontrastmedel som i sin tur binder in till exempelvis tumörvävnad. På så sätt kan förändringar som sker på en cellulär eller molekylär nivå tidigt i sjukdomsprocessen detekteras. Tekniken förväntas ha stor betydelse inom t.ex. cancerdetektion, individanpassad behandling, läkemedelsutveckling samt för att få förståelse för hur sjukdomar som cancer uppkommer.

Medicinska avbildningstekniker som MRI, PET och optiska tekniker har utvecklats mest då det gäller molekylär avbildning, medan utvecklingen för ultraljud inte varit lika stark. Anledning till detta är att ultraljudskontrastmedel idag består av mikrometerstora bubblor som p.g.a. sin storlek är begränsade till att befina sig i blodbanan och därför inte kan användas för att avbilda och detektera processer utanför denna. Bubblorna tenderar att släppa från de stället de fäst in till då kraften från blodflödet drar loss dem, vilket försvårar detektionen av sjukdomsdrabbade områden.

Ultraljud är den avbildningsteknik som används mest inom sjukvården idag. Tekniken är lättillgänglig, billig, helt ofarlig och bilderna visas direkt på skärmen istället för att man skapar dem i efterhand som man gör med de flesta andra avbildningstekniker. Ska molekylär avbildning bli en del i rutinundersökningarna i framtidens sjukvård bör ultraljud vara med som en av standard-avbildningsteknikerna inom området.

För att kunna komma runt problemen med kontrastmedelsbubblorna är nya ultraljudstekniker under utveckling. Denna avhandling behandlar en sådan ny ultraljudsmetod; magnetomotorisk ultraljudsavbildning. Då det här doktorandarbetet påbörjades hade tekniken mer eller mindre precis presenterats och teknikens möjligheter var outfitskade. Istället för att använda sig av mikrobubblor används magnetiska järnoxid-nanopartiklar som kontrastmedel i magnetomotorisk ultraljudsavbildning. Samma typ av nanopartiklar används idag som MRI-kontrastmedel och partiklarna är lagom stora för att kunna användas för molekylär avbildning. Dock är partiklarna för små för att avbildas med ultraljud, men genom att förflytta dem med ett magnetfält skapar man en rörelse i partiklarnas omgivning som går att detektera med ultraljud. En matematisk metod, en algoritm, som kan filtrera ut denna rörelse och undertrycka andra rörelsestörningar har

utvecklas och algoritmen kan visa var partiklarna finns i form av färg i den i övrigt svartvita ultraljudsbilden.

Den magnetomotoriska tekniken och den utvecklade algoritmen undersöktes först grundligt i ett plastmaterial som har samma materialegenskaper som mänsklig vävnad (så kallade fantomstudier). Detta gjordes för att se hur rörelsen från de magnetiska järnoxid-nanopartiklarna betedde sig då olika parametrar, så som styrkan på magnetfältet och dess frekvens, ändrades. För att få ännu bättre förståelse för vad som påverkade rörelsen byggdes en modell av den experimentella uppställningen i ett datorprogram. Därefter jämfördes resultaten från datamodellen med resultaten från den experimentella modellen.

För att utforska möjligheten att kunna använda den nya ultraljudstekniken i sjukvården så undersöktes sedan om järnoxid-nanopartiklar i lymfnoder, eller mer specifikt i portvaktkörteln, gick att detektera i råttor. Lymfnoder är en del av lymfssystemet som har till uppgift att dränera överflödig vätska, lymfa, från kroppens vävnader och att föra den tillbaka till blodsystemet. Lymfnoderna sitter i grupper längs med lymfkärlsnätverket i vilket lymfan färdas och de har till uppgift att filtrera lymfan från mikroorganismer och andra små partiklar. Portvaktskörtlen är den första lymfnoden som dränerar tumörer hos cancerformer som sprids via lymfssystemet, exempelvis bröstcancer och malignt melanom (hudcancer). Om cancer har spridit sig är sannolikheten över 99 % att det finns cancerceller i portvaktskörtlen. Därför är det viktigt att hitta denna och undersöka den.

Djuren i studierna i den här avhandlingen var råttor som injicerades med nanopartiklar i ena baktassen. Lymfnoden i knäet som dränerade injektionsstället, filtrerade ut nanopartiklarna från lymfan så att de samlades upp i lymfnoden. Därefter undersöktes djuren med magnetomotoriskt ultraljud.

Resultaten från både fantomstudierna och djurstudierna har sett mycket lovande ut. Även om rörelsestörningarna från t.ex. hjärtslag och andning hos djuren har varit mer än 150 gånger större än nanopartikelrörelsen så har algoritmen klarat av att filtrera ut denna och tydligt kunnat visa vart partiklarna har befunnit sig.

I studierna som ingått i den här avhandlingen har inte några antikroppar eller andra molekyler som kan binda in till sjukdomsdrabbade områden använts, utan det är teknikens kapacitet som har testats. Genom att koppla inbindningsmolekyler till järnoxid-nanopartiklarna skulle en ny dimension av möjligheter och tillämpningar kunna öppnas upp i morgondagens vård.

SUMMARY

The earlier abnormalities coupled with disease can be discovered in the body, the larger is the chance to survive the disease. Molecular imaging is a new research field, which aims to detect these abnormalities at a molecular level, when the chance of survival is still high. The main idea of molecular imaging is to use target specific contrast agents that accumulate at the diseased region at a concentration detectable with the imaging modality used. Nanoparticles have shown to be very suitable as molecular imaging contrast agents due to their small size, which enable them to cross biological barriers and to bind to the biological entity of interest.

Ultrasound is the most widely used imaging technique in health care today. It is cost effective, safe and provide real-time images with high temporal resolution. The development in the molecular imaging field has not been as strong for ultrasound as for other imaging modalities, since ultrasound contrast agents consist of micrometer-sized bubbles, which are confined to the vascular system. To image nanoparticles with conventional ultrasound is not possible as the small size of the particles make them unable to backscatter ultrasound at a detectable level. To overcome this limitation, new ultrasound imaging approaches have been developed which indirectly image nanoparticles. In this thesis the potential of one such imaging technique; magnetomotive ultrasound imaging (MMUS), has been examined. The principle of MMUS is to displace magnetic nanoparticles by applying a time-varying magnetic field. As the particles start to move, their surrounding will move as well. Ultrasound is then used to detect the induced tissue motion.

When this doctoral work begun, only a few MMUS studies had been presented. The aim with this thesis was set to evaluate the potential of MMUS concept and investigate its potential of *in vivo* use.

In the first study in this thesis (paper I), a frequency and phase tracking MMUS algorithm was developed. The algorithm is able to filter out the nanoparticle-induced movement and suppress other artifactual movements in the ultrasound images. The nanoparticle movement is then superimposed as a color code on the grayscale B-mode ultrasound images to visualize the nanoparticle location.

To evaluate the potential of the developed algorithm, phantom studies were performed (paper I, II and IV). Polyvinyl alcohol (PVA), a plastic material with similar mechanical material properties as tissue, was used as phantom material. Different parameters such as the nanoparticle concentration and the frequency of the applied magnetic field were

altered in the phantom studies in order to examine their impact on the magnetomotive displacement. To obtain an even better understanding of the magnetomotive displacement, data simulations were performed. Models of experimental setups were created and the experimental findings were compared with the simulation results (paper II and IV) and a good agreement was found.

Moreover, to evaluate the potential of MMUS to be used in health care, animal studies have been performed (paper III, V and VI). In this thesis the MMUS technique was evaluated in a clinical relevant model, where SPION-laden sentinel lymph nodes (SLNs) in rats were imaged. In this model, MMUS was thought to serve as a complementary imaging modality to standard methods, to add high-resolution bedside surgical guidance during SLN surgery in breast cancer or malignant melanoma patients. In order to test the model in a clinical scenario, pre-staging of the SPION-laden SLNs was done with MRI or PET (paper III and VI, respectively), after which MMUS imaging was performed.

The results both from the phantom and the animal studies have shown to be very promising. Displacement in the sub-micrometer range has been detected in all studies. Although displacement artifacts have been more than two orders of magnitudes larger than the MMUS signal, the algorithm has been able to successfully pinpoint the location of the SPION-laden regions (e.g. paper III and V). This indicates that the MMUS technique has potential for future clinical use.

LIST OF PUBLICATIONS

Included

- I. **Frequency and Phase Sensitive Magnetomotive Ultrasound Imaging of Superparamagnetic Iron Oxide**
Maria Evertsson, Magnus Cinthio, Sarah Fredriksson, Fredrik Olsson, Hans W Persson and Tomas Jansson
IEEE Transactions on Ultrasonics, Ferroelectrics, and Frequency Control, vol 60, no.3, pp 481-491, 2013. Front cover illustration

Author's contribution: Major part of method development, phantom manufacturing, measurements, data analysis of the results and authoring the manuscript.
- II. **Normalization of Magnetic Field Effects: Towards Quantitative Magnetomotive Ultrasound Imaging**
Maria Evertsson, Magnus Cinthio, Sarah Fredriksson, Fredrik Olsson, Hans W Persson and Tomas Jansson
IEEE International Ultrasonics Symposium, Orlando, USA, 2011: 775-778

Author's contribution: Major part of method development, phantom manufacturing, simulation development, measurements, data analysis and authoring the manuscript.
- III. **Multimodal detection of iron oxide nanoparticles in rat lymph nodes using Magnetomotive ultrasound imaging and Magnetic Resonance Imaging**
Maria Evertsson, Pontus Kjellman, Magnus Cinthio, Sarah Fredriksson, Rene in't Zandt, Hans W. Persson, Tomas Jansson
IEEE Transactions on Ultrasonics, Ferroelectrics, and Frequency Control, vol 61, no.8, pp 1276-1283, 2014 (Invited paper)

Author's contribution: Responsible for the magnetomotive ultrasound technology part, method development, data analyzing and authoring the manuscript.

- IV. **Induced tissue displacement in magnetomotive ultrasound imaging - simulations and comparison with phantom and *post mortem* experiments**
Tomas Jansson, Maria Evertsson, Esayas Atilé, Roger Andersson, Sarah Fredriksson, Hans W Persson, Ingrid Svensson, Magnus Cinthio
Submitted

Author's contribution: Responsible for the experiments and simulations, parts of the data analysis and parts of writing the manuscript.

- V. ***In vivo* magnetomotive ultrasound imaging of rat lymph nodes – a pilot study**
Maria Evertsson, Magnus Cinthio, Pontus Kjellman, Sarah Fredriksson, Roger Andersson, Hanna Toftevall, Hans W. Persson, Tomas Jansson
Proceedings of the IEEE International Ultrasonics Symposium. Taipei, Taiwan. 2015 (Selected as finalist in the student paper competition)

Author's contribution: Study design, experimental setup, data analysis and authoring the manuscript.

- In vivo* detection of ^{68}Ga -labelled superparamagnetic iron oxide in rat sentinel lymph nodes using PET/CT, Magnetomotive ultrasound and MRI**
Maria Evertsson, Pontus Kjellman, Magnus Cinthio, Roger Andersson, Thuy Tran, René in't Zandt, Gustav Grafström, Hanna Toftevall, Sarah Fredriksson, Christian Ingvar, Sven-Erik Strand, Tomas Jansson
Submitted

Author's contribution: Study design, responsible for MMUS and MRI imaging, animal handling, all data analysis and main author of the manuscript.

Related

Phase-locked magnetomotive ultrasound imaging of superparamagnetic iron-oxide nanoparticles

Maria Holst, Magnus Cinthio, Sarah Fredriksson, Fredrik Olsson, Hans W Persson and Tomas Jansson

Proceedings of the IEEE International Ultrasonics Symposium. San Diego, USA, 2010: 1007-1010

**Magnetomotive ultrasound imaging of rat lymph nodes in situ:
Assessment of imaging parameters**

Maria Evertsson, Magnus Cinthio, Sarah Fredriksson, Pontus Kjellman, Rene in't Zandt, Hans W. Persson, Tomas Jansson

Proceedings of the IEEE International Ultrasonics Symposium. Prague. 2013: 604-607

Multimodal detection of iron oxide nanoparticles in rat lymph nodes using Magnetomotive ultrasound imaging and Magnetic Resonance Imaging,
Maria Evertsson, Magnus Cinthio, Sarah Fredriksson, Pontus Kjellman, Rene in't Zandt, Hans W. Persson, Tomas Jansson

World Molecular Imaging Conference, Savannah, USA, 2013: Sep. 18-21

Induced tissue displacement in magnetomotive ultrasound imaging - simulations and experiments

Tomas Jansson, Maria Evertsson, Esayas Atile, Roger Andersson, Sarah Fredriksson, Hans W Persson, Ingrid Svensson, Magnus Cinthio

Proceedings of the IEEE International Ultrasonics Symposium. Chicago, USA 2014: 639-642

B-field energy dependent phase lag dispersion in magnetomotive ultrasound imaging

Roger Andersson, Magnus Cinthio, Maria Evertsson, Hanna Toftevall, Anders Wahlström, Sarah Fredriksson, Göran Nybom, Tomas Jansson

Proceedings of the IEEE International Ultrasonics Symposium. Taipei, Taiwan 2015

Effect of nanoparticle size on the displacement signal in magnetomotive ultrasound imaging

Roger Andersson, Maria Evertsson, Magnus Cinthio, Hanna Toftevall, Sarah Fredriksson, Tomas Jansson

European Molecular Imaging Meeting, Utrecht, Netherlands, 2016

Patent

Magnetomotive probe system and method of use thereof

Magnus Cinthio, Maria Evertsson, Tomas Jansson, Hans W Persson, Fredrik Olsson, Sara Fredriksson (WO2014/180854)

ABBREVIATIONS

CCD - Charge-coupled device

CT - Computed tomography

DLS - Dynamic light scattering

FDG - Fluorine 18 (F^{18}) fluorodeoxyglucose

IQ - In-phase quadrature

NIR - Near infrared

MMUS - Magnetomotive ultrasound imaging

MRI - Magnetic resonance imaging

PEG - Polyethylene glycol

RES - Reticuloendothelial system

PET - Positron emission tomography

PVA - Polyvinyl alcohol

RF - Radio frequency

SLN - Sentinel lymph node

SPECT - Single-photon emission computed tomography

SPIO - Superparamagnetic iron oxide nanoparticle

TEM - Transmission electron microscope

AIM

The overall aim of this thesis was to investigate the concept of MMUS and whether it could be used for *in vivo* imaging. More specifically to:

- Develop a MMUS algorithm capable to pinpoint regions containing superparamagnetic iron oxide nanoparticles and suppress unwanted motion artifacts
- Evaluate how various parameters, such as frequency of the magnetic field and SPION concentration, affect the magnetomotive nanoparticle displacement
- Verify experimental findings in simulations
- Evaluate the feasibility to use MMUS *in vivo*
- Evaluate the potential for using SPIONs in multimodal imaging including MMUS in a clinically relevant scenario

CONTENTS

Acknowledgments	V
Populärvetenskaplig sammanfattning.....	VII
Summary.....	IX
List of publications	XI
Abbreviations.....	XV
Aim	XVI
1. Background	1
1.1 Molecular imaging.....	1
1.2 Medical imaging modalities	2
1.2.1 Computed tomography	2
1.2.2 Optical imaging.....	3
1.2.3 MRI	3
1.2.4 Nuclear imaging	4
1.2.5 Ultrasound	5
1.2.6 Ultrasound contrast agents.....	7
1.3 Multimodal imaging.....	9
1.4 Nanoparticles as contrast agents.....	9
1.4.1 Superparamagnetic iron oxide nanoparticles (SPIONs).....	11
1.5 Magnetomotive ultrasound imaging	12
1.5.1 Other contributions to the MMUS research field	14
1.6 Cancer	16
1.6.1 Lymphatic system and lymph nodes	17
1.6.2 Current clinical procedure of SLN surgery.....	17
1.6.3 Multimodal detection of sentinel lymph nodes	18

2.	Methodology	19
2.1	Nanoparticles.....	19
2.2	Polyvinyl alcohol phantoms	19
2.3	Animals and animal model.....	20
2.4	Experimental setup	20
2.5	Frequency sensitive and phase gated algorithm.....	21
2.6	Simulations.....	22
2.7	Multimodal studies	23
2.7.1	Magnetic resonance imaging	23
2.7.2	Positron emission imaging	23
2.8	Displacement calculations.....	23
3.	Description of included papers	24
3.1	Paper I.....	24
3.2	Paper II.....	26
3.3	Paper III	27
3.4	Paper IV	29
3.5	Paper V.....	31
3.6	Paper VI	33
4.	Discussion	35
5.	Future work.....	41
6.	Conclusion	42
7.	References.....	43

1. BACKGROUND

1.1 Molecular imaging

Molecular imaging; the ability to visualize, quantify and characterize biological processes *in vivo* at a molecular and cellular level, is expected to change today's health care. It is of great importance to detect abnormalities in an early stage of disease in order to give the right diagnosis and treatment and increase patient survival. Conventional imaging modalities mostly detect macroscopic changes in anatomy and physiology between normal and pathological tissue, e.g. morphology or blood flow and contractile function. Instead, molecular imaging aims to probe molecular abnormalities that are the basis of disease, rather than to image the end effects of these molecular changes [1, 2].

Advances in genomics and molecular biology, have opened up the ability to identify suitable molecular entities that can be targeted to appropriately prepared contrast agents. Together with the progress of noninvasive, high-resolution *in vivo* imaging technology, molecular imaging has become a growing research field during the past two–three decades [3, 4].

The key idea of molecular imaging is to use molecular probes to detect biological processes *in vivo*, without disturbing their function. The probes need some sort of ligand, e.g. an antibody, peptide or small molecule, which promotes accumulation of the probe at the target of interest, e.g. a tumor. Moreover, the probe needs a label system which allows it to be imaged with medical imaging techniques and which makes it possible to distinguish the diseased targeted tissue from the surrounding normal tissue [2, 5].

Molecular imaging has been clinical reality for some time, e.g. by imaging targeted radionuclides with positron emission tomography (PET) [6]. While much of the technology remains on a proof-of-principle stage, the potential of molecular imaging is considerable [5]. Imaging the molecular changes which underlie disease may provide a much earlier detection of disease, potentially it may be possible to detect changes today defined as "prediseased state", which most likely is the key of a better outcome for patients. Moreover, there may be potential to directly image the effect of therapy, facilitate development of new pharmaceuticals and provide individualized treatment [2, 4, 7].

1.2 Medical imaging modalities

To image molecular events *in vivo*, put some, often contradictory, demands on the imaging technique. Ideally, the imaging modality should: create a strong signal-to-background ratio, have high spatial resolution, have low or no depth limitations, and have reasonable cost [2-4]. In this chapter, an overview of the most common medical imaging techniques is presented. Their fundamental imaging principles are described as well as their present capability to be used for molecular imaging. Since this dissertation deal with a novel ultrasound technique, more attention will be given to ultrasound imaging

1.2.1 Computed tomography

In computed tomography (CT), a low energy X-ray source and a detector, positioned at opposite sides of the patient along a straight line, are rotated around the patient. X-ray projections are obtained in different angles and thereafter reconstructions of 2D and 3D anatomical images are performed.

X-rays are attenuated differently in various tissues, which shows as contrast in the CT images. The attenuation is similar in different soft tissues such as blood, muscle and brain but for bone and air the attenuation differs more markedly. The contrast between soft tissues is thereby relatively low whereas air-tissue and bone-tissue interface provide excellent contrast.

Modern CT scanners are very fast; a 3D cross section image can be created in matter of seconds. Additionally, resolution as good as 50-200 μm can be achieved and the imaging technique is considered to have no imaging depth limitation. Drawbacks with CT imaging are that the radiation is ionizing, expensive examination and low contrast between soft tissues, that often leads to requirement of an iodinated contrast agent. These contrast agents have the drawback that they tend to create allergic reactions. [1, 8].

CT anatomical images are commonly used to complement functional molecular imaging images from nuclear imaging techniques [9-11], but CT is usually not used as a stand-alone molecular imaging modality [1].

1.2.2 Optical imaging

There are two major types of optical imaging techniques; bioluminescence and fluorescence.

In bioluminescence imaging, visible light with a specific wavelength is emitted as a product of an enzymatic catalyzation (luciferase enzymes) in a living organism [12].

In fluorescence imaging instead, an external light source is used to excite fluorophores or fluorescent proteins, which in turn emit detectable light with a specific wavelength.

The emitted light in both techniques is usually detected with a sensitive charge-coupled device (CCD) camera [1]. Optical imaging is very sensitive and quantitative, it is cost-effective, rapid and easy to use. The main drawback with the technique is the limited penetration depth which is due to the absorption and scattering of light in tissue and blood as well as auto fluorescence in tissue [13]. The penetration depth is limited to a few millimeter/centimetre. Another drawback is a spatial resolution of several millimeters [5].

Optical imaging has been widely used in animal *in vivo* studies. For example non-invasive studies, where tracking of tumor growth in animals and the efficacy of new therapeutic agents in individual animals, have been published. To improve the penetration depth, near infrared (NIR) fluorophores have been developed. These fluorophores emit light with a longer wavelength (700-900 nm) compared to other commonly used fluorophores e.g. green fluorescent protein (FGP) (wavelengths < 600 nm). Photons with a longer wavelength are less absorbed by blood and tissue and enables thereby a deeper penetration depth [13].

1.2.3 MRI

Magnetic resonance imaging (MRI) utilize the alignment of the protons of the hydrogen atoms in water inside a strong external magnetic field. Temporary radiofrequency pulses are used to force the protons' spins to change their alignment in the field and emit detectable signal to the MRI scanner. After a radiofrequency pulse duration, the spins will return to their relaxed equilibrium state in the magnetic field. The contrast in the MR image is given either by how fast the protons spin out of phase (T_2) or how much time is required for the protons to return to their equilibrium state in the magnetic field (T_1). This information is used to generate highly tissue specific MR images. By applying a magnetic field gradient at the same time as radio frequency pulses are emitted, spatial information in the MR-image can be obtained. This can be done due to the change in spin resonance frequency along the magnetic field gradient.

MRI is a radiation free imaging modality producing soft-tissue images with very high diagnostic value [1, 8]. MRI benefit from high spatial resolution, around 1mm for a 1.5 Tesla scanner [14]. Drawbacks with MRI are high examination costs, long examination time and a temporal resolution in the order of seconds [8]. The sensitivity of MRI is also low compared to nuclear and optical imaging methods [1].

MRI contrast agents can either be T₁ or T₂ weighted, creating bright or dark contrast in the MR images, respectively. The most commonly used MRI contrast agents in the clinic are gadolinium chelates (T₁) and superparamagnetic nanoparticles (SPIONs) (T₂). One imaging application is to use SPIONs to highlight tumors in the liver. This can be achieved with the aid of varying SPION uptake in tumor tissue compared to non-diseased liver tissue. Many studies, where SPIONs coupled with ligand molecules that bind to specific targeting molecules, have been presented [15, 16]. For example, Chen et al. have showed imaging of SPIONs linked with a monoclonal antibody, binding only to tumor cells expressing a certain type of receptors. For tumor cells lacking the receptor, no uptake was observed in the T₂-wieghted MR images [17].

1.2.4 Nuclear imaging

Single-photon emission computed tomography (SPECT) and positron emission tomography (PET) both visualize physiological activity. Radioactive compounds are injected into the body and act as radiation sources. Mostly, the radioactive compound is linked to a specific physiologically relevant molecule which will accumulate at specific sites in the body, e.g. a tumor. It is desirable to use radionuclides with fast radioactive decay to reduce patient exposure. Since both imaging techniques lack anatomical information they are preferably used in combination with CT or MRI.

SPECT

In SPECT gamma emitters (^{99m}Tc, ^{81m}Kr) are generally used. A gamma camera is rotated around the patient and projection images of radioactive decays are collected in different angles and thereafter reconstructed to 2D/3D tomographic emission images. To determine the origin of the decays, a lead collimator is used. The collimator limits detection of photons, only to be detected when traveling perpendicular towards the camera sensor. Off-angle photons are attenuated by the collimator. In the camera the γ -photons interact with a scintillation crystal and visible light is formed. The light hits a photomultiplier tube which generates an electrical signal that can be detected.

PET

The radionuclides in positron emission tomography (PET) are positron (β^+) emitters (e.g., ^{18}F , ^{15}O). After the decay event, the positron travels a very short distance before positron annihilation. Two γ -photons with energy of 511 keV are emitted and travel exactly in opposite directions. The PET camera consist of a stationary detector ring and only almost simultaneous detection of two γ -photons, on opposite sides of the detector ring, is registered as a valid signal, whereas a single detection is rejected as noise. The line between the two detectors that registered the photons, serve as the direction of the projection. The signal-to-noise ratio is thus dramatically better for PET than SPECT. The conversion of γ -photons to a detectable signal is performed in the same way as for SPECT [8].

SPECT and PET have been the main molecular imaging modalities and have the advantage of being very sensitive and provide whole body imaging. However, both techniques suffer from a significant lower resolution than MRI and CT (approximately 1 cm), ionizing radiation from radioactive labels and high examination costs [2, 8].

PET imaging of the radionuclide fluorine 18 fluorodeoxyglucose (FDG) is the molecular imaging approach, most commonly used in the clinic today. FDG PET is especially used for cancer staging and restaging [18]. Due to the increased metabolism in tumors, a larger uptake of glucose molecules can be seen in tumor cells. When transported into the cell, the glucose molecule becomes trapped in its phosphorylated form. Imaging is then performed after 30-60 minutes. Nearly all tumors show a significant increase in FDG metabolism and their location in the body can thereby be revealed in the PET images. The imaging approach draws on passive targeting, i.e. no antibody or other molecule enabling specific binding to the cancer cells, is attached to the radionuclide. Only the increased metabolism of the cells is responsible for the increased FDG accumulation. Thus, false-positive results in benign lesions with increased glucose metabolism may occur [19].

1.2.5 Ultrasound

Ultrasound is a mechanical wave with a frequency above 20 kHz, inaudible for the human ear. In diagnostic imaging, frequencies between 2-15 MHz are most commonly used. To generate an ultrasound image, a short pulse of ultrasound is transmitted into tissue by an ultrasound transducer, positioned in contact with the skin. At boundaries between different tissues, parts of the energy will be reflected back to the transducer whereas the remainder will be transmitted further into the tissue media. The amplitude of the reflected pulse is determined by the difference in acoustic impedance between two media i.e.

difference in density and compressibility. If the difference in acoustic impedance is small, as it is for soft tissue, most of the wave will be transmitted further into the next medium. Between media with a large difference in acoustic impedance, such as soft tissue/bone and especially soft tissue/air, there will be a large or nearly total reflection of the ultrasound pulse. This limits the penetration depth of the pulse and thereby also the imaging depth.

The speed of sound in human tissues is usually approximated to 1540m/s. By measuring the time from transmit to receive of an ultrasound pulse, the location of the reflecting echo can be determined by multiplying the sound speed with the time and divide by two. This, so called pulse-echo technique, is used when generating an ultrasound image.

The transducer, transmitting the ultrasound pulse, consist of an array of piezoelectric micrometer sized elements, usually hundreds. When applying an electrical voltage, these elements will expand or contract (depending on if the electrical voltage is positive or negative) and thus, produce a mechanical pressure wave. Conversely, an electrical voltage is produced when the piezo elements are compressed or stretched by an external force, in this case the returning ultrasound wave. The ultrasound raw data is called radio-frequency (RF) data and is derived from reflected oscillating ultrasound waves on the transducer interface. By mixing the RF-data with a complex sinusoid signal and thereafter down sampling it, in-phase quadrature (IQ) data is obtained. The advantage is that the amount of data is reduced while information is preserved. In this thesis, IQ-data is used in the signal processing.

2D ultrasound images, called B-mode images, are created line-by-line. For each line, a number of piezo elements (a subset of the array) are electrically excited and the transmitted pulses combine to an ultrasound wavefront. By applying electrical time delays on the elements, the ultrasound wavefront can be focused and/or steered. The amplitude of the received echoes is converted into gray scale, where an echo with larger amplitude is represented as brighter than an echo with a smaller amplitude. Once all echoes have been received from one scanning line, a new group of elements transmit a new ultrasound pulse, producing the next line in the B-mode ultrasound image.

Within most biological tissues there are small scale variations in acoustic properties. When these small anatomical irregularities are in the same range or smaller than the ultrasound wavelength, the ultrasound pulse will be scattered over a large range of angles. The scattered waves will interfere with each other, either constructively or destructively, and lead to random fluctuations in brightness in the B-mode image, called speckle.

Doppler ultrasound is commonly used to measure blood velocity. When a reflecting object is moving relatively a transmitting ultrasound source, there will be a change in observed frequency of the sound wave compared to the transmitted frequency. The difference

between the transmitted (f_t) and received (f_r) frequency, is known as the Doppler frequency (f_D). The relation can be described by the Doppler equation:

$$f_D = f_r - f_t = \frac{2f_t v \cos\theta}{c} \quad (1)$$

Where v is the velocity of the blood, c is the speed of the ultrasound in tissue and θ is the angle between the ultrasound beam and the direction of the blood flow.

There are two main classes of Doppler techniques, continuous-wave (CW) and pulsed wave (PW). CW systems transmit and receive ultrasound continuously and the transmitter and receiver must be separate. The blood velocity can be determined using Eq. (1). In PW systems, short consecutive pulses are transmitted. As the target moves, there will be a difference in phase between the received pulses from a specific depth, which is used to determine the velocity of the moving object. The region, from which the Doppler signals are obtained, is with CW Doppler determined by the fixed region where the transmit and receive ultrasound beam overlap. For PW Doppler, the depth is controlled by the operator. When using PW Doppler, aliasing of high blood velocities can occur when the number of transmitted ultrasound pulses per time unit (pulse repetition frequency, prf) is too low to reconstruct all Doppler frequencies of the moving blood. In CW systems, there will be no aliasing.

Color Doppler and Power Doppler are two types of Doppler that are commonly used in health care. Both these Doppler methods give a representation of movement as a color code, superimposed on the B-mode image. Color Doppler, color code frequencies/velocities of the Doppler signal, whereas power Doppler instead color codes the energy of the Doppler signal rather than velocity. Both color Doppler and power Doppler use pulsed waves, formatting images [20].

Ultrasound is the most widely used imaging tool for clinical practice due to its low cost, availability, temporal resolution, safety and lack of ionizing radiation [1, 21]. Ultrasound images show good soft tissue contrast but as bone and air reflects the ultrasound strongly, some parts of the body are inaccessible. The effective imaging depth is limited to approximately 10 cm in most organs [8, 22].

1.2.6 Ultrasound contrast agents

Commercially available ultrasonic contrast agents

Commercially available ultrasound contrast agents are encapsulated gas filled microbubbles with an average size range of 2-6 μm , which are intravenously injected into the bloodstream [20]. High-molecular-weight gases, such as sulphurhexafluoride or

perfluorocarbon, are used as filling gas and to stabilize the bubble. The gas is encapsulated in a biocompatible shell consisting of e.g. simple phospholipid micelles, biocompatible polymers or albumin. The large difference in acoustic impedance between the microbubbles and their surrounding results in increased backscattering of the ultrasound waves, and hence, an increased magnitude of the received echo. Moreover, bubbles can be seen as a mechanically resonant system, and thereby possessing a resonant frequency. When a microbubble is insonated with ultrasound, the bubble is forced to oscillate. If the ultrasound wave is at the microbubble resonant frequency, the bubble will oscillate at its maximum degree enabling the scattering cross section to become two to three orders of magnitudes larger than the geometrical cross section of the bubble. This is exploited so that bubbles are designed to have a resonant frequency in the range for diagnostic ultrasound. By a fortunate coincidence, bubbles then end up with sizes that are small enough to pass the capillary bed in the pulmonary circulation, enabling intravenous injection. In addition to the increased scattering cross section due to resonance, several detection schemes that exploit non-linear phenomena, add to the detectability of microbubbles [23].

Molecular imaging ultrasound contrast agents

Due to the relatively large size of the microbubbles, they are confined to the intravascular system [7, 24]. Hence, ultrasound molecular imaging has been engineered to target disease on intravascular endothelial cells such as angiogenesis, inflammation and thrombus formation [25]. Targeting could either be non-specific or specific. Non-specific targeting can be achieved by modifying the contrast agent shell in order to increase the affinity to specific disease molecules. For example, both albumin and lipid-shelled bubbles can attach to microvasculature endothelium adherent leucocytes, which have been activated by inflammation. In specific targeting, ligand molecules e.g. antibodies or peptides, are conjugated to the microbubble shell. These ligand molecules then bind specifically to one target only [26, 27]. The number of bonds and the bond strength between the ligand molecule and its target are important since large shear stresses from the vascular flow are acting on the targeted bubbles, tending to drag them away [7].

To enter the extravascular space, new types of submicrometer sized ultrasound contrast agents for molecular imaging such as liposomes [28] and perfluorocarbons droplets [29] have been developed. Some of these particles are small enough to migrate through injured or leaky vasculature where the permeability is abnormally high [7]. However, because of their small size, these submicrometer contrast agents produce a much weaker echo than gaseous microbubbles [29].

1.3 Multimodal imaging

As described above, all imaging modalities possess both advantages and limitations. To enable accurate visualization of molecular events places great demands on an imaging technique, and one imaging modality alone may not be capable to shoulder this task. One method to solve the problem is to combine two or more imaging modalities and in that way utilize their respective advantages and overcome their limitations, so called multimodal imaging [30, 31]. Today PET/CT and PET/MR systems are available for human use. These system combines high resolution anatomical CT or MRI images with excellent metabolic and molecular information from PET [32]. In animal studies many multimodal combinations have been presented, such as MR/optical [33, 34] where the optical technique provides high sensitivity images, PET/US where ultrasound images complements with morphological information to the PET images [35] and CT/PET/optical where the optical technique was thought to act as bedside guidance for the surgeon during surgery [36]. In Fig. 1 below is a schematic sketch over a multimodal SPION contrast agent.

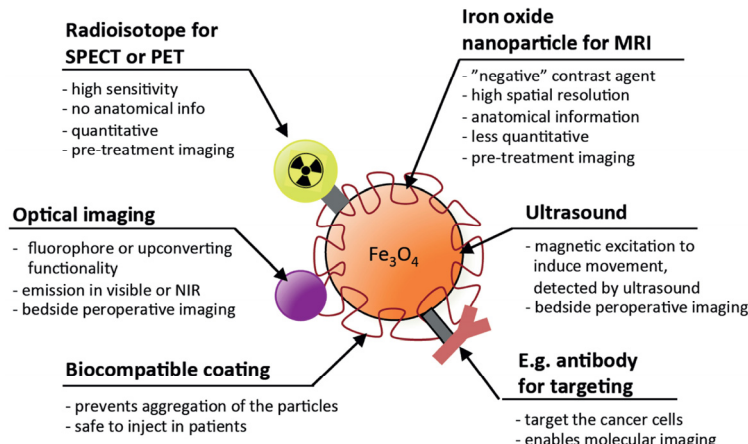


Figure 1. A schematic illustration of an example of a multimodal and multifunctional superparamagnetic iron oxide nanoparticle. By labeling the nanoparticle with different type of markers, e.g. fluorophores or radionuclides, visualization can be performed with more than one imaging modality, allowing simultaneous functional and anatomical imaging. Moreover, target specific molecules such as antibodies and peptides can be bound to the particle surface to enable specific binding of a target of interest.

1.4 Nanoparticles as contrast agents

The growing interest in molecular imaging as well as multimodal imaging has led to an increasing development of new imaging probes/contrast agents. Several key criteria must generally be fulfilled for the imaging probe to enable molecular imaging *in vivo*. The probe

should; have high specificity and binding efficacy to the target of interest, be non-toxic, generate high signal-to-background ratio, be biocompatible, possess circulation times long enough to enable accumulation at the target site at an adequate concentration and it should be able to overcome biologic barriers (vascular, interstitial, cell membrane) [2-4, 15].

In recent years there has been a significant increase in development of nanoparticles as contrast agents for molecular imaging. The small size of nanoparticles allow them to overcome biological barriers in the body and make them proper for binding to a biological entity of interest [5, 15, 37]. The nanoparticles' large surface-to-volume ratio, allow a large number of potential sites for targeting molecules. For example, a protein can have around ten sites of modification before loss of biological functionality whereas a nanoparticle similar in size can have in excess of 1500 [5]. Due to the large number of potential targeting sites, more than one type of molecule can be conjugated to the nanoparticle surface, making the nanoparticle multifunctional, enabling e.g. both specific binding, contrast enhancement and therapy. The functionality of nanoparticles make them also suitable to be used as multimodal contrast agents [5, 15, 38].

The size, the shape and the surface chemistry of the nanoparticles are three important parameters strongly affecting the particles' behavior in biological systems [39, 40]. To ensure the highest possible delivery efficiency of the probes, it is of great importance to understand how these parameters affect the biological interactions and functions. In the occasion of intravenous nanoparticle injection, a long circulation time is often desirable to enable nanoparticle accumulation of adequate concentrations at the desired target site e.g. inside tumor tissue. In the bloodstream, serum proteins will bind to the nanoparticles' surface and enhance their recognition by the immune surveillance system. The particles will then be removed from the bloodstream by phagocytic cells in the reticuloendothelial system (RES) inside the liver and spleen. A charged nanoparticle will be removed faster from the bloodstream than a neutral.

In case of target specific particles, this removal is a large problem since the circulation time may not be enough for the particles to encounter the desired target. To avoid rapid clearance of the nanoparticles, polyethylene glycol (PEG) can be added to the nanoparticle surface. Also other coating molecules, such as polysaccharide dextran, have shown to prolong the circulation time. However, regardless of coating material, the reticuloendothelial system still remains the site of greatest nanoparticle accumulation. Depending on the situation, this may not always be a disadvantage. Many studies profiteer from this to image the liver or macrophages associated with disease such as cancer, inflammation or cardiovascular disease [5, 40].

The nanoparticle size has shown to be important for cellular uptake. For intravenously administrated nanoparticles, particles with a diameter smaller than 6 nm will quickly be cleared from the body due to excretion by the kidneys [40], whereas particles exceeding 1000 nm will rapidly be eliminated by the reticuloendothelial system [41]. In the case of tumor imaging, a particle diameter of 30 - 200 nm is desirable to enable a long circulation time and to give the particles a chance to pass through the leaky vasculature around a tumor and penetrate into tumor tissue. Moreover, it has been found that particles larger than 100 nm do not extravasate far beyond the blood vessels, as they will be trapped in the extracellular matrix between cells. As the particles decrease in size, a larger amount of nanoparticles can be found in a tumor, but as a consequence the particles will be retained for a shorter time [40]. In subcutaneous injections, intended for lymphatic uptake, the ideal size of a particle is between 10 and 100 nm. A smaller particle will leak directly into the bloodstream while a larger particle will remain at the site of injection [42].

The shape also affects the cellular uptake of nanoparticles. Studies have shown that an increased uptake of rod-shaped particles compared to spheres was found when the size of the particles exceeded 100 nm, whereas for particles less than 100 nm the relationship was the reverse. Moreover, rods-shaped micelles have shown to have a ten time longer circulation time than spherical micelles [40].

Some nanoparticles have shown to be cytotoxic to human cells, causing oxidative stress or elicit immune response. The toxicity could either be caused by the particles themselves or by individual components of the particles as they are degraded. It is thereby of great importance to evaluate the particles' possible toxicity in parallel to their potential [5].

1.4.1 Superparamagnetic iron oxide nanoparticles (SPIONs)

Metal-based nanoparticles are being extensively used as imaging contrast agents [43]. One commonly metal nanoparticle used, is the superparamagnetic iron oxide nanoparticle (SPION). These particles have been approved as MRI contrast agents for two decades [38, 44] and are e.g. used to image liver tumors and metastases in the clinic [15]. The particles are considered to be non-toxic [45, 46] and have been frequently used in molecular imaging studies [42, 46-49].

Iron oxide is a ferromagnetic material but when the core size of a ferromagnetic particle becomes smaller than a characteristic magnetic domain for that specific material (generally of the order tens of nanometers), the particle will contain a single magnetic domain only and behave as a paramagnetic material. The particles will then attract toward regions of stronger field strength and no hysteretic behavior will be noticeable i.e. no remanent magnetization will be present when the magnetic field is removed. Only thermal energy is needed to allow the particles to freely reorient their spins, making the net magnetic flux of the particles zero. This makes the particles more colloidal and physiologically stable,

e.g. occlusion of particles in vessels may be prevented since no accumulation due to remanent magnetization will occur. When the size of the nanoparticle cores becomes larger, the thermal energy will not be enough to reorient the spins of the particles, thereby the particles will start to exhibit ferromagnetic properties [38, 50, 51].

Since iron oxide cores are not colloidally stable in an aqueous solution, a coating of a biocompatible material, such as PEG or lauric acid, is needed to enable *in vivo* use [42, 51].

1.5 Magnetomotive ultrasound imaging

The scattering cross section of an insonated particle is proportional to the sixth power of the radius of the particle [52]. This makes it virtually impossible for nanoparticles to backscatter ultrasound at a detectable level. To overcome this limitation new ultrasound imaging techniques, which indirectly employ nanoparticles as contrast agents, have been developed. One such technique is photoacoustic imaging, where nanoparticles with a well-characterized absorption spectrum, absorb pulsed laser light. The absorbed laser energy creates a small temperature increase and in turn, upon the thermoelastic expansion that follows, an acoustic wave, detectable with an ultrasound [53].

Another such imaging technique is magnetomotive ultrasound (MMUS) imaging that was first demonstrated by Oh et al. in 2006 [44]. The technique is built on the same key principle as magnetomotive optical coherence tomography, which Oldenburg et al. presented in 2005 [54]. In MMUS a time-varying magnetic field is used to create a movement of magnetic particles deposited in a surrounding material. As the particles start to move, their closest surrounding will move as well and this movement can be detected with ultrasound.

The magnetomotive force, \mathbf{F} , acting on a nanoparticle in a magnetic field, \mathbf{B} (magnetic flux density), may be written as:

$$\mathbf{F} = (\mathbf{m} \cdot \nabla) \mathbf{B} \quad (2)$$

where \mathbf{m} is the dipole moment of the particle.

If the magnetization, \mathbf{M} , is uniform over the object, as can be assumed for a nanoparticle, $\mathbf{m} = V\mathbf{M}$ where V is the volume of the magnetic portion of the nanoparticle. V can be rewritten as $V = V_{np} * f_m$, where V_{np} is the total size of a nanoparticle and f_m is a dimensionless factor, representing the volumetric ratio of magnetic material in a nanoparticle. The magnetization can be written as $\mathbf{M} = \chi\mathbf{H}$, where \mathbf{H} is the magnetic field strength and χ is the difference in susceptibility between the nanoparticle core material, χ_{np} , and the susceptibility of the surrounding material, χ_{sur} (in other words $\chi = (\chi_{np} - \chi_{sur})$). Since the surrounding material in the context of this thesis can be

considered weakly diamagnetic, $|\chi_{np}| \gg |\chi_{sur}|$ and consequently $\chi = \chi_{np}$. By assuming that the magnetic field, \mathbf{B} , does not change significantly over nanoparticle due to its small size, \mathbf{H} can be defined as $\mathbf{H} = \frac{\mathbf{B}}{\mu_0}$, where, μ_0 is the permeability of free space ($4\pi \times 10^{-7}$ N/A²). The magnetic dipole can then be expressed as:

$$\mathbf{m} = \mathbf{M}V = \chi \mathbf{H}V = \frac{\chi V_{np} f_{np}}{\mu_0} \mathbf{B} \quad (3)$$

The magnetic force acting on the nanoparticle due to the magnetic field can then be expressed as:

$$\mathbf{F} = \frac{\chi V_{np} f_{np}}{\mu_0} (\mathbf{B} \cdot \nabla) \mathbf{B} \quad (4)$$

Since the magnetic field is applied along the z-axis Eq. (4) can be simplified:

$$\mathbf{F} = \frac{\chi V_{np} f_{np}}{2\mu_0} (\mathbf{B}_z \cdot \nabla) \mathbf{B}_z \quad (5)$$

As $(\mathbf{B}_z \cdot \nabla) \mathbf{B}_z = \frac{1}{2} \nabla(\mathbf{B}_z \cdot \mathbf{B}_z) \approx \mathbf{B}_z \frac{d\mathbf{B}_z}{dz}$, Eq. (5) can be rewritten as:

$$\mathbf{F} = \frac{\chi V_{np} f_{np}}{\mu_0} \mathbf{B}_z \frac{d\mathbf{B}_z}{dz} \quad (6)$$

A time-varying sinusoidal magnetic field has been applied as excitation field

$$\mathbf{B}_z(\mathbf{r}, t) = \sin(2\pi f_{mod} t) \mathbf{B}_z(\mathbf{r}) \quad (7)$$

where f_{mod} is the modulation frequency on the applied magnetic field, \mathbf{r} is the spatial position of the nanoparticle and t is time.

The magnetic force acting on the nanoparticles, the magnetomotive force, becomes:

$$\mathbf{F} = \frac{\chi V_{np} f_{np}}{\mu_0} \sin^2(2\pi f_{mod} t) \mathbf{B}_z(\mathbf{r}) \frac{d\mathbf{B}_z(\mathbf{r})}{dz} = \frac{\chi V_{np} f_{np}}{\mu_0} \frac{(1 - \cos(4\pi f_{mod} t))}{2} \mathbf{B}_z(\mathbf{r}) \frac{d\mathbf{B}_z(\mathbf{r})}{dz} = \frac{\chi V_{np} f_{np}}{2\mu_0} (1 - \cos(4\pi f_{mod} t)) \mathbf{B}_z(\mathbf{r}) \frac{d\mathbf{B}_z(\mathbf{r})}{dz} \quad (8)$$

From Eq. (8) it can be seen that the amplitude of the force is proportional to the magnetic flux density (\mathbf{B}) times its gradient. The force can be increased by increasing the magnetic field, the susceptibility of the particles or the particle core size (to the extent that the nanoparticle still keeps superparamagnetic properties) and also by changing the magnetic field distribution. Moreover, Eq. (8) also shows that the frequency of the magnetic force acting on the particles will be twice the applied magnetic field frequency. That is, the particles will vibrate with twice the magnetic field modulation frequency, as long as sinusoidal magnetic field with no offset is used [55-57].

From Eq. (8), which gives the magnetic force acting on a nanoparticle, it follows that the total force acting on the particle in a surrounding material can be written as:

$$\mathbf{F}_{\text{tot}} = \frac{\chi V_{np} f_{np}}{2\mu_0} (1 - \cos(4\pi f_{mod} t)) \mathbf{B}_z(\mathbf{r}) \frac{d\mathbf{B}_z(\mathbf{r})}{dz} - k z(t) - s \frac{dz}{dt} \quad (9)$$

where $-k z(t)$ is an elastic restoring force of the medium and $s \frac{dz}{dt}$ is a viscous drag force [44].

1.5.1 Other contributions to the MMUS research field

In the first proof-of-concept MMUS study, Oh et al. [44] demonstrated the technique in murine livers ex vivo. Mice were intravenously injected with SPIONs and the particles were taken up by macrophages in the liver. After two days, the livers were removed from the animals and imaged with MMUS. A sinusoidal magnetic field was used to create a MMUS movement and simultaneously imaging with standard M-mode and Doppler techniques were performed. In 2007 Mehrmohammadi et al., from the same research group, used a single-element transducer (25 MHz) to image tissue-mimicking PVA phantoms with inclusions containing different concentration of nanoparticles [46]. The phantoms were positioned in a water cuvette, which was mechanically moved in micrometer steps in order to obtain a cross sectional ultrasound image. Using a cross-correlation algorithm when post-processing the RF-data, MMUS images were obtained. Also, SPION-laden macrophages mixed in a gelatine solution were imaged with M-mode and Doppler techniques, in this study. Next, the group developed a magnetomotive system generating a pulsed magnetic field. The setup was evaluated in PVA-phantoms and also in a mouse kidney which was removed from the animal and then injected with a gelatine solution containing SPIO-laden macrophages [48]. A single-element transducer was used together with a cross-correlation algorithm to construct the ultrasound data. Mehrmohammadi et al. then focused on increasing the pulsed magnetomotive signal. In phantom studies they showed that clusters of SPIONs induced a larger magnetomotive displacement than the same amount of SPIONs not arranged in clusters [50]. Later they also showed that the same behavior occurred in cells, by comparing MMUS displacement from macrophages containing SPION aggregates with a solution of macrophages mixed with free SPIONs [58]. In 2013 the group published the first *in vivo* pulsed MMUS study [59]. High susceptibility zinc-doped SPIONs were injected intratumorally in three nude mice bearing xenograft tumors. A permanent magnet was placed close to the tumor for two hours to increase the concentration of nanoparticles. Thereafter the tumors were imaged with pulsed MMUS using a linear array transducer, in contrast to the single-element transducer used in their previous studies. In order to obtain a higher framerate, the transducer was unfocused in transmit. MMUS displacement was calculated from the B-mode data.

In 2013, Pope et al. imaged SPION-laden platelets in agar phantoms analyzing RF-data with a frequency- and phase-locked MMUS algorithm. In this study, the solenoids creating the magnetic field, were positioned at the same side on the sample as the ultrasound transducer. This was made for the first time in a MMUS study and is of large importance in potential clinical translation of the MMUS technique [60].

Ultrafast plane wave pulsed MMUS imaging was introduced in SPION-laden gelatin phantoms by Ting et al in 2014 [61]. The relation between three phantoms with different elasticities and their dynamic response after MMUS excitation pulses was investigated. Later in 2015, Huang et al [62] from the same research group presented an *in vivo* study where presence of SPIONs was shown in rat SLNs.

In 2015, Fink et al. presented a MMUS algorithm, enabling imaging of SPIONs in weak echogenic tissue by using the variation of magnitude of the RF-data. The algorithm was evaluated in phantom studies but aiming to visualize the concentration of accumulated nanoparticles in magnetic drug targeting. The research group have also evaluated other MMUS algorithms, using both RF-data and B-mode images [51, 63].

Mariappan et al. demonstrated in the end of 2015 magneto acoustic tomography, where MMUS was used to create tomographic images. Tumors injected with SPIONs, were imaged by rotating an ultrasound transducer 180° and taking MMUS images every second degree. Four different cross sections per tumor were obtained to investigate the nanoparticle distribution [45].

Thiago et al. have recently presented a new elastography method called Shear wave dispersion MMUS. The magnetomotive force was used to induce shear waves within SPION-laden gelatin phantoms, and the mechanical properties of the phantoms with different gelatin concentration were estimated. To evaluate the results, Shear wave dispersion MMUS was compared with transient elastography and the elasticity and viscosity were in good agreement [64]. The research group has also used the MMUS technique to image micrometer sized particles. In 2012 Pavan et al. imaged magnetomotive induced shear waves using micrometer sized ferrite particles [65]. Bruno et al. developed in 2014 a hybrid transducer, where an AC biosusceptometer was combined with an ultrasound transducer. Displacement of ferrite particles dispersed in yoghurt was examined with the two techniques when a sinusoidal magnetic field was generated by the AC biosusceptometer [66]. Later the hybrid transducer was used to image initial stomach emptying in rats, which had been injected with ferrite-yoghurt solution in their stomach. 3D-images were also created by moving the transducer in 1mm steps in the craniocaudal direction [67].

Furthermore, MMUS has been combined with photoacoustic imaging; Magnetomotive photoacoustic imaging [68, 69]. Dual contrast agents are used to enable visualisation with both imaging techniques e.g. nanoparticles with magnetic core surrounded by a gold nanoshell. The MMUS and photoacoustic signals are combined and the photoacoustic signals generated from the background material can be suppressed as well as an improved nanoparticle distribution map may be obtained.

1.6 Cancer

Cancer is one of the leading causes of morbidity and mortality world-wide, with approximately 14 million new cases in 2012. Around 8.2 million of those ends with fatal outcome, which corresponds to approximately 13 % of all deaths. During the next two decades, the number of annual cancer cases, are expected to increase from 14 million in 2012 to 22 million. Key factors for patient survival are early detection, accurate diagnosis, and effective treatment [70]. Conventional biomedical imaging techniques detect cancerous tumors at a size of approximately one centimeter in diameter, the tumor then consist of around 10^9 cancer cells. A mile stone would be to detect the tumor before angiogenesis takes place, when the tumor leaves the state of diffusion limited nutrition. The number of cancer cells are then approximately 10^5 [22]. Molecular imaging is expected to play a central role in this transformation since physiological information, specific for each patient, may be combined with the anatomical information from conventional imaging modalities used in health care today [71]. The use of nanoparticles may likely be needed in order to enable the contrast agents to cross the biological barriers in the body [15].

In order to evaluate the potential of *in vivo* use for magnetomotive ultrasound and the developed algorithm, imaging of SPION-laden sentinel lymph nodes (SLN) was chosen as a clinical relevant model in this doctoral thesis. The sentinel lymph node is the first lymph node draining the primary tumor in cancer types which spread through the lymphatic system, such as breast cancer and malignant melanoma [72]. Breast cancer is the most common cause of cancer deaths among women, yearly killing 500 000 women [70] and the incidence of malignant melanoma is steadily growing and has doubled in the past 20 years [73]. In case of malignant cancer dissemination, the SLN is the first place cancer cells will anchor to a certainty of more than 99.9 %.

The last two decades sentinel lymph node biopsy has developed to be the standard diagnostic procedure, staging breast and melanoma cancer. The technique helps to identify the SLN and examination of cancer cells is performed. In case of cancer infiltration, dissection of all lymph nodes in the draining nodal basin is performed.

The earlier surgical procedure was to remove all lymph nodes in the draining nodal basin and then, after surgery, look for cancer spread. SLN biopsy has shown to be as good as the old method [74]. Since most cancer patients do not have lymphatic metastases, and removal of the whole nodal basin may cause acute wound problems, chronic lymphedema, nerve injury anesthetic complications as well as large increase of health care cost, sentinel biopsy has become the gold standard technique [75]. In order to provide right diagnosis and treatment, it is of great importance to find the SLN.

1.6.1 Lymphatic system and lymph nodes

The lymphatic system transport the interstitial fluid, the lymph, back to the blood system. The lymph enter though the lymphatic capillaries and is propelled though the lymphatic vessels by contraction of smooth muscle cells in the inner walls of the vessels, together with external forces from skeletal muscle pump and respiration. Valves in the lymph vessels force the interstitial fluid in the vessels only to move in one direction. Lymph nodes are scattered along the lymphatic vessels. They are a part of the immune system and filter the lymph from microorganisms, cells and other particles. Each node consists of lymph filled sinuses and between the sinuses, large clusters of lymphocytes, called lymphatic nodules, are present. The lymph nodes also contain macrophages and dendritic cells, which together with the lymphocytes take care of the elements in the lymph, and if needed, activates an immune response [76].

1.6.2 Current clinical procedure of SLN surgery

Today lymphoscintigraphy is the gold standard technique to localize the SLN in breast cancer and melanomas. Approximately 2-24 hours before surgery, ^{99m}Tc -labeled nanocolloids are injected into or around the tumor. Two to four hours prior to surgery, planar or tomographic images are obtained using a gamma camera to localize the SLN. Then intraoperatively, a handheld gamma probe is used to find the SLN [77, 78]. In most cases a blue dye is injected 5-20 minutes before surgery to visualize the SLN during surgery [78, 79]. When detected, the SLN is removed and examination of cancer infiltration is, during ongoing surgery, performed using histology [47]. If cancer cells are found, the remaining lymph nodes in the draining nodal basin are removed.

As the nanocolloid and the blue dye may migrate to adjacent lymph nodes, it may be hard to identify the SLN. Additional lymph nodes, also being radioactive, are thereby removed, to make sure not to miss the SLN [75]. Another drawback with the current detection procedure is the lack of precise anatomical information in the pre-operative scintigraphic

images, leaving the detection of the SLN to be determined by the experience of the surgeon [47].

1.6.3 Multimodal detection of sentinel lymph nodes

As an alternative to the standard procedures, SPIO nanoparticles have been used as a multimodal contrast agent in the sentinel lymph node model used in this doctoral thesis. At most the SPIONs have been imaged with three modalities; MMUS, MRI and PET/CT. The first two imaging modalities use the magnetic properties of the SPIONs to create an image, whereas imaging with PET, was possible first after labelling the particles with a ^{68}Ga -isotope. The suggested setup is to do pre-operative staging with high sensitive and quantitative PET together with high resolution anatomical MRI, then some days later, as beside guidance for the surgeon, MMUS will be used to visualize the SLN (see Fig. 2). Since the retention time of the SPIONs in the SLN is longer than the commercial contrast agents used today, together with the fact that the MMUS signal is only dependent on the concentration of the SPIONs, intraoperative SLN detection can be performed several days after nanoparticle administration, when the radioactivity has decayed. In addition, the blue dye currently in clinical use to guide the surgeon at SLN resection can be excluded and thus the risk of anaphylaxis associated with the dye [17]. Because of the relative fast uptake of SPIONs in the SLN, a radionuclide with a shorter half-life can be used. This will result in a lower absorbed dose to the patient and omit radiation exposure to the surgical staff. It would be optimal to improve the localization even further by labelling the SPIONs with tumor specific markers, but this need to be investigated in future studies.



Figure 2. Suggested clinical workflow. 1) Injection of ^{68}Ga -labeled SPIONs around/into the tumor. 2) Prestaging with PET/MR, localizing the SLN. 3) Bedside surgical guidance using MMUS imaging, visualizing the SLN.

2. METHODOLOGY

2.1 Nanoparticles

The superparamagnetic nanoparticles used in all papers were obtained from Genovis AB (or its subsidiary GeccoDots AB), Lund, Sweden. The particles consisted of solid iron oxide cores of Fe_3O_4 (magnetite), coated with polyethylene glycol (PEG) to make the particles biocompatible and to prevent aggregation. The production protocol is described by Kjellman et al [42].

The properties of the particles used in the different papers can be seen in Table 1 below. The sizes of the particles were measured either by Transmission Electron Microscope (TEM) or Dynamic Light Scattering (DLS). TEM measurements always return the core size of the particles, whereas with DLS, both the core size and the whole particle size, i.e. core plus coating can be obtained.

In paper III, two sizes of particles were used in order to examine the difference in nanoparticle uptake in the SLN of the animals in the study.

Paper	Core size (nm)	Total size, core plus coating (nm)	Magnetic saturation (emu/g)
I	18 ± 2	30	80
II	18 ± 2		80
III	11	31 or 67	80
IV	18 ± 2		80
V	10 ± 2	40 ± 2	80
VI	10 ± 5	40 ± 5	80

Table 1. Sizes of nanoparticles used in the thesis.

2.2 Polyvinyl alcohol phantoms

In paper I, II and IV, phantoms were used to evaluate the nanoparticle movement and our frequency and phase sensitive algorithm. Elasticity parameters, similar to human tissue, were obtained using polyvinyl alcohol (PVA). Crystallized PVA was dissolved in water using a Nüve FN300 oven (Nüve, Ankara, Turkey) to melt the crystals. The PVA solution was poured into phantom molds, which underwent two freeze/thaw cycles, to crosslink the polymer so that solidification of the PVA solution could occur. By adding nanoparticles in the PVA solution and employing the same solidification procedure, nanoparticle inserts were formed. Graphite was added in all phantoms to act as ultrasound scatterers.

2.3 Animals and animal model

To evaluate the MMUS technique and the algorithm's potential to be used *in vivo*, a clinically relevant sentinel lymph node model was employed in this thesis. The motivation was the idea to use MMUS as a bedside surgical guidance, to help the surgeon localize the SLN. In paper III, V and VI, animal studies were performed using such a model. 6-weeks-old female Wister rats were injected with 100 μ l nanoparticle solution in their right hind paw, and the popliteal lymph node in the animals' right knee, the SLN in this model, was imaged with the MMUS setup. The electromagnet was placed under the animals' knee and the ultrasound transducer was placed on the opposite side of the knee. To allow optimal contact with the transducer, the animals' legs were shaved. During the measurements, the animals were anesthetized and kept warm on a heating bed, while their body temperature was controlled with a rectal probe. All studies were performed in compliance with the Swedish regulations for the conduct of laboratory animals.

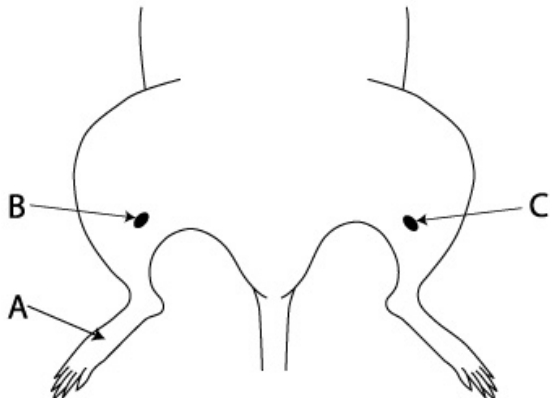


Figure3. Schematic illustration of the animal with relevant sites. (A) Injection site. The injections were given subcutaneously on the dorsal side of the right hind paw. (B) and (C), popliteal lymph nodes, located at the posterior surfaces of the knees. (B) is the SLN and (C) the control lymph node in the contralateral leg.

2.4 Experimental setup

A high-frequency ultrasound scanner, VisualSonics Vevo 2100 (VisualSonics Inc., Toronto, ON, Canada), together with two transducers with different center frequencies, MS 250 (bandwidth 13-24 MHz, center frequency 21MHz) and MS 550D (bandwidth 25-35 MHz, center frequency 32MHz), was used to capture ultrasound images in all studies in this thesis. To generate a time-varying magnetic field, a solenoid surrounding an iron-core was used as electromagnet. A time varying electrical signal, either sinusoidal or square-wave, was produced using a function generator and then amplified by a power amplifier or controlling a power switch, respectively. The signal was fed to the solenoid producing a time-varying magnetic field. An oscilloscope was used to monitor the amplitude of the electrical signal applied to the solenoid. In all studies, the solenoid was excited with various voltages, from 5 to 60 V_{pp}, and frequencies, from 4 to 16 Hz, to give an indication how these parameters affected the nanoparticle displacement. The magnetic flux density, measured immediately above the iron core, was 0.18 or 0.42 mT depending on the setup used. Using the Visualsonics Vevo 2100 research interface the radio

frequency in-phase quadrature (RF-IQ) data could be collected. The data was then exported to Matlab (The MathWorks Inc., Natick MA), where our algorithm was implemented, and processed offline.

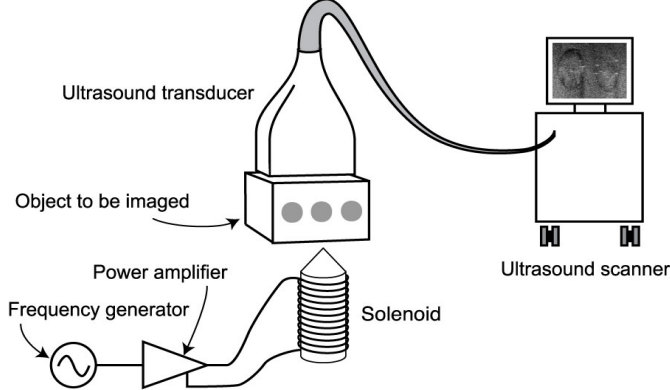


Figure 4. Schematic illustration of the experimental setup. By applying a time-varying electrical signal to a solenoid with a cone-shaped iron core, a magnetic field, which varies in time, will be created. The object containing nanoparticles (in this case a PVA-phantom) is positioned just above the iron-core tip from which the magnetic field is extended. When the magnetic field is applied, the nanoparticles within the object will start to move, and thereby the particles immediate surrounding. A high frequency ultrasound scanner is used to detect this movement.

2.5 Frequency sensitive and phase gated algorithm

In the practical experiments in this doctoral work, post-processing of the RF-IQ ultrasound data was performed, using our frequency tracking and phase gated algorithm. The algorithm calculates the magnitude of the movement in each pixel at frequency f_0 , the frequency with which the nanoparticles oscillate. It is based on quadrature detection and phase gating at precisely the same frequency and phase as the nanoparticles (paper I-IV), or the applied magnetic field (paper V and VI). Movements at all other frequencies and phases will be suppressed, making the algorithm very robust to motion artifacts. The main steps of the algorithm are outlined below:

From the phase of the ultrasound IQ-data, the nanoparticle oscillation frequency (f_0), was tracked at each pixel position through all frames in the ultrasound cineloop.

Let $r(x, y, m) + j r_Q(x, y, m)$ ($m = 1, 2, \dots, M$) represent the IQ-data from a cineloop of M frames, as exported from the Vevo 2100. Here, r_I denotes the real part and r_Q the imaginary part, and (x, y) corresponds to the lateral and axial coordinates, respectively, of a pixel position in the image. The phase $r(x, y, m)$ for each pixel position throughout all frames was extracted from the argument of the received IQ-data, $r(x, y, m) = \arg(r_I(x, y, m) + j r_Q(x, y, m))$.

After unwrapping, the phase was quadrature detected with f_0 :

$$R(x, y, m) = r(x, y, m) \times e^{j2\pi f_0 m \Delta t} = I(x, y, m) + jQ(x, y, m) \quad (9)$$

where Δt corresponds to the time interval between two frames. (Note that I and Q , as denoted here, are different from what is considered IQ-data in the RF-data acquisition.) To obtain the displacement amplitude at frequency f_0 for each pixel, a mean value of the quadrature detected sequence $R(x, y, m)$, was calculated. The mean value was used instead of a low-pass filter because we were interested to detect only the displacement magnitude at f_0 :

$$\overline{R(x, y)} = \overline{I(x, y)} + j\overline{Q(x, y)} \quad (10)$$

The displacement amplitude, $A(x, y)$, was then obtained as:

$$A(x, y) = 2|\overline{R(x, y)}| = 2\sqrt{\overline{I(x, y)^2} + \overline{Q(x, y)^2}} \quad (11)$$

To compare $A(x, y)$ (i.e., at f_0 only) with the total motion (i.e., displacement at all frequencies), the rms deviation of the phase $r(x, y, m)$ was calculated, and denoted r_{rms} . To make the numbers comparable, the displacement magnitude A was divided by a factor of $\sqrt{2}$.

As the magnetomotive displacement (i.e. the displacement at the precise frequency and phase of the nanoparticles) in the nanoparticle-laden areas induces a displacement with opposite phase in its adjacent surrounding in the horizontal direction (especially in the phantom studies (Fig. 5), the phase P in each pixel at frequency f_0 was calculated in order to enable separation with regard to phase. The phase was calculated as:

$$P(x, y) = \arg\left(\frac{Q(x, y)}{I(x, y)}\right) \quad (12)$$

2.6 Simulations

Simulations in COMSOL (Comsol AB, Stockholm, Sweden) were made in paper II and IV to evaluate experimental findings. Experimental setups, of both phantoms (paper II and IV) and a SLN (paper IV), were modelled in COMSOL and the nanoparticle induced magnetomotive displacement was investigated and compared to the experimental results. In paper IV, the magnetic field (\mathbf{B}), within the phantom was first calculated. The result was used to calculate the magnetic field gradient and then, by multiplying the magnetic field times its gradient, the magnetomotive force acting on the particles was obtained. To get hold of movement in the modelled setups, the magnetomotive force was applied as a body load on the nanoparticle-laden areas.

2.7 Multimodal studies

The sentinel lymph node model employed to evaluate the *in vivo* use of MMUS in this thesis, was in paper III and VI, applied in multimodal imaging studies. MRI or PET/CT was used as pre-staging imaging technique to localize the particles in the SLN, and then afterwards, MMUS imaging was performed. The following medical scanners were used:

2.7.1 Magnetic resonance imaging

Two types of MRI scanners were used. In paper III, a 2.4 T Bruker Avance II system, (Bruker Corp., Billerica, MA) and in paper VI, an 11.7 T vertical wide bore MR scanner (Agilent Technologies). The 2.4 T scanner is a small animal scanner, with a chosen imaging field of view of $60 \times 50 \times 50$ mm and a pixel resolution of $234 \times 234 \times 468$ μm for whole body scans of the animals.

The 11.7 T scanner is a micro system scanner designed to image small samples. The imaging field of view in the 11.7 T scanner for 3D imaging was $20 \times 10 \times 10$ mm³ and the pixel resolution $39 \times 39 \times 39$ μm^3 . With this scanner, the excised SLN and control lymph node from each animal were imaged.

2.7.2 Positron emission imaging

A dual-modality PET/CT system (NanoPET/CT, Bioscan, USA) was used in paper VI to obtain whole-body PET images of the rats. The injected paw was placed in a lead cylinder during the measurements to shield the injection site from adding too much background counts in the lymph node image. A five minute CT scan was first performed, followed by a PET scan where images were collected in 45 minutes. The reconstructed images were exported to VivoQuant (inviCRO, Boston, USA) for co-registration and analysis.

2.8 Displacement calculations

The magnetomotive displacement in the nanoparticle-laden inserts or sentinel lymph nodes was calculated in all studies. The nanoparticle containing areas were outlined in the B-mode images. Thereafter, the magnetomotive displacement was calculated in all pixels in the outlined area, using the frequency and phase gating algorithm described earlier. An average displacement for all pixels within the selected region was then calculated to represent the magnetomotive displacement in that specific area. This was done in all papers except in paper I, where an area consisting of 9×9 pixel in the center of the nanoparticle insert, was used.

3. DESCRIPTION OF INCLUDED PAPERS

The MMUS technique was in the thesis evaluated both in phantom studies (paper I and II, IV) and in animal studies (paper III, V and VI). Simulations of the experimental findings were also made (paper II and IV). Here follows a summary of the separate studies.

3.1 Paper I

In paper I, a frequency sensitive and phase gated MMUS algorithm was developed. The algorithm analyses the RF-IQ-data, and it is based on quadrature detection and phase gating at the frequency of interest. Thereby, effective suppression of displacements at other frequencies is achieved, which makes the algorithm very robust to motion artifacts. This is crucial in *in vivo* measurements. The ultrasound data was collected with a high-frequency linear-array ultrasound scanner, which never had been done in a MMUS study before. To evaluate the algorithm, a PVA phantom with three SPION-laden inserts (concentration 0.3, 0.45 and 0.6 mg Fe/ml), was used. By applying a sinusoidal magnetic field, displacement of the nanoparticles and thereby also displacement in the rest of the phantom, was induced. The voltage and frequency applied to the solenoid, which created the magnetic field, were altered (10, 20 and 30 V_{pp} and 4, 8, 12 and 16 Hz, respectively) and the impact of the nanoparticle displacement was investigated. Displacements outside nanoparticle-laden regions, similar in magnitude to displacements in the nanoparticle containing regions, were found. These displacements had the same frequency as the nanoparticles, but they were phase shifted approximately π radians. The algorithm was designed to eliminate these displacements by restricting the phase interval to the nanoparticle phase (± 1.15 radians) only. A clear representation of the location of the SPION-laden regions could then be made after superimposing the magnitude of the nanoparticle displacement as color code on the B-mode ultrasound image, see Fig. 5. An increased nanoparticle displacement was found for a higher nanoparticle concentration (5 times larger for the high concentration SPIO-laden insert), an increased magnetic field and a lowered frequency. A median signal-to-clutter ratio improvement using the proposed algorithm was 36 dB compared with simply summing the movement energy at all frequencies. The algorithm presented, was used to evaluate data in paper I-VI.

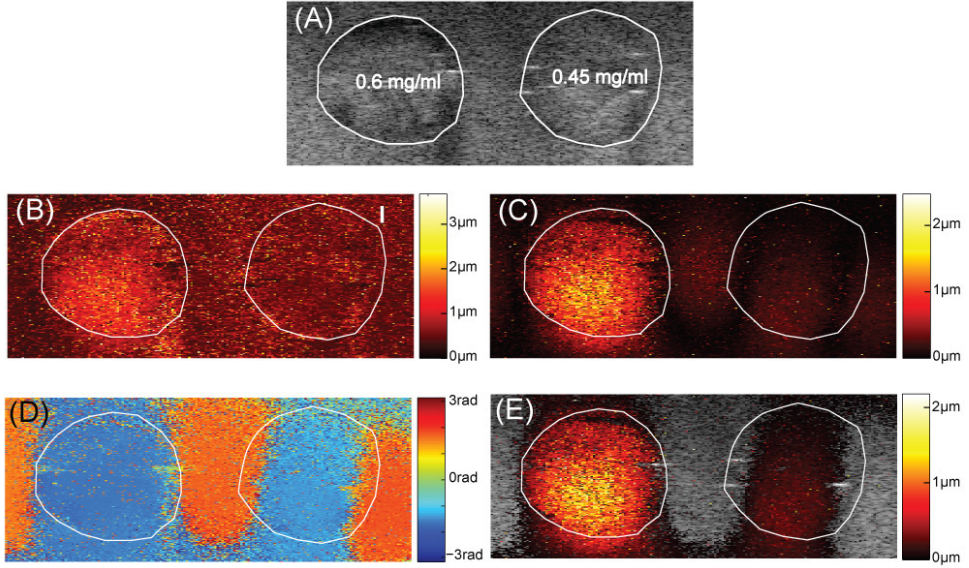


Figure 5. These images show a polyvinyl alcohol (PVA) phantom with two SPION-laden inserts during magnetomotive ultrasound imaging. The magnetic field excitation was 4 Hz 30 V. The images are color-coded with regard to displacement magnitude (panel B, C and E) or phase (panel D), according to the color bars at the right hand side of each image, respectively. Panel A shows a cross sectional B-mode ultrasound image of the phantom, the SPION-laden inserts are outlined and their concentration is denoted in the image. Panel B displays the total displacement in the image, i.e. the movement at all frequencies and phases. Panel C is a frequency-tacked but phase insensitive image, i.e. displacement at the nanoparticle frequency only, f_0 (two times the applied magnetic field frequency, see Eq. 8), is color-coded. In panel D is the phase distribution at the nanoparticle frequency f_0 shown. A frequency shift of approximately π radians between the nanoparticle-laden regions and the areas in-between can be seen. The MMUS image is presented in panel E. This image is color-coded with regard to both frequency and phase. Displacement, only occurring with frequency f_0 and a phase difference less than ± 1.15 radians relative to the center phase in the nanoparticle-laden regions, was color-coded.

3.2 Paper II

Since the movement of the nanoparticles depend not only on the magnetic field (**B**), but also on the field gradient plus material parameters (Eq. 8), a first step trying to make the MMUS technique more quantitative was done in paper II. A PVA phantom with a homogenous distribution of nanoparticles was made to investigate the nanoparticle movement across the image plane. Then a comparison with simulations of the magnetic force was performed, to evaluate the potential for image normalization of magnetic field effects. Both the experimental and the simulation result showed a decreased movement with distance to the iron core tip, from which the magnetic field was extending. However, both at the transducer face and at the edges of the phantom, the displacement reached zero due to the rigid boundaries (see Fig 6A). This finding did not agree with the simulation result where only the magnetic field was considered. Hence, quantification may be difficult if not taking the surrounding material properties into consideration.

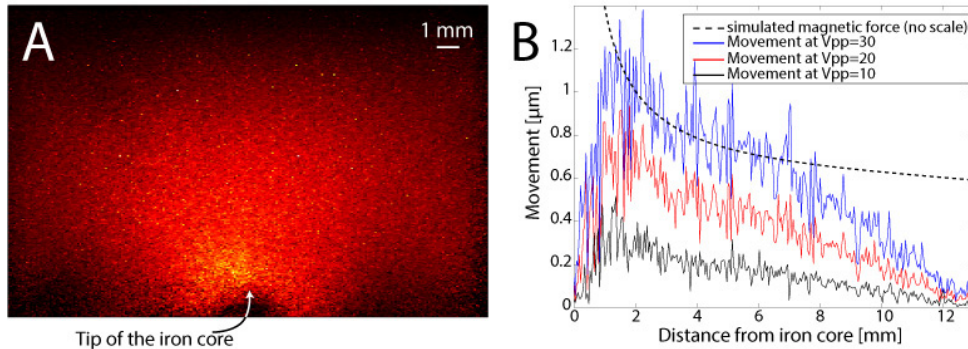


Figure 6. Panel (A) shows a MMUS image of the PVA phantom with displacement as color code. The image is a mean of three different cross sections, all obtained at magnetic field excitation 5 Hz 30 V. The tip of the iron core, from which the magnetic field is extending, is located at the bottom center, and the transducer is positioned along the top. The maximum displacement was measured to be 2.9 μm and is color-coded as white. Panel B shows displacement in micrometers along the vertical axis extending from the tip of the magnet for three voltages (10, 20 and 30 V), all obtained at 5Hz. Each solid line is a mean of three measurements. The dotted line represents the simulated magnetic force (field times its gradient) and is scaled to fit in the figure.

3.3 Paper III

In this paper, a multimodal animal study, combining MRI (*in vivo*) and MMUS (*post mortem*), was presented. The sentinel lymph node model described earlier (section 2.3) was used. Eight Wistar rats were injected with two sizes of nanoparticles (31 and 67 nm, each size were given to four rats) in order to investigate the dependence between particle size and SLN uptake. The nanoparticles were given in two different concentrations (0.3 and 3 mg Fe/ml). As in paper I, the frequency and voltage of the signal applied to the solenoid were altered (10, 20, 30 Vpp and 5–15 Hz, in steps of 2.5 Hz, respectively). MRI and MMUS signals were found in all animals (except from one animal in the MMUS measurements, where loss of information in the RF-IQ data made it impossible to evaluate the data). For both higher nanoparticle concentration and smaller nanoparticles, we found that the MMUS data showed a larger magnetomotive displacement (1.56 ± 0.43 and 1.94 ± 0.54 times larger, respectively) and that the MR-images were affected to a higher degree. The MMUS displacement also increased with lower excitation frequency (1.95 ± 0.64 times larger for 5 Hz compared with 15 Hz) and higher excitation voltage (2.95 ± 1.44 times larger for 30 V compared with 10 V). The out-of-phase motion found in the paper I, was also present herein (Fig. 7 D). This was the first multimodal study where MMUS and MRI was combined and also the first study where harmonic MMUS was demonstrated in animals.

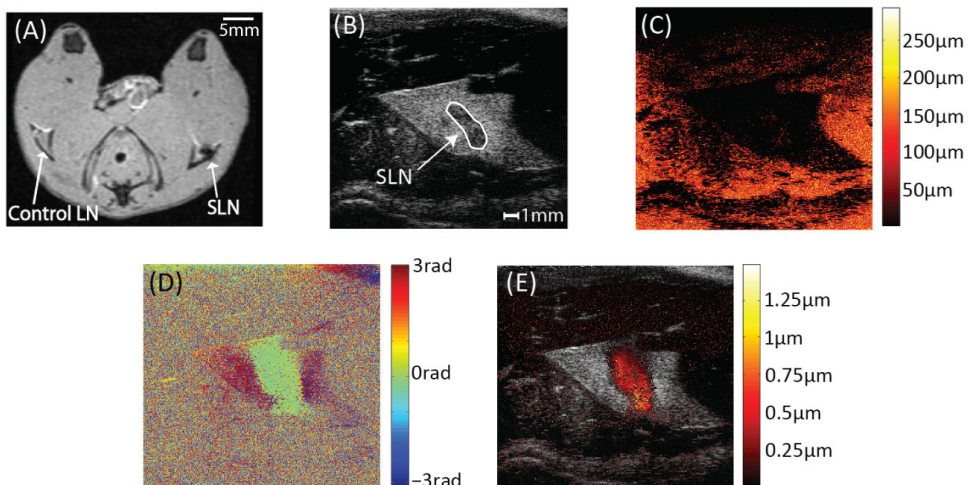


Figure 7. A T2*-weighted MR image of the popliteal nodes (SLN and control node) of a rat, injected with small particles and low concentration is shown in panel A. The hyperenhancement in the SLN, shown as black, indicates the presence of SPIONs. Panel B is a B-mode image of the SLN and the SLN is outlined in the image. Note the different scale bars in panel A and B. The total movement at all frequencies and with all phases is shown in panel C as a color code, superimposed on the B-mode. In panel D is the phase distribution on nanoparticle displacement frequency only, shown as a color code, overlaid on the B-mode image. The π radians phase shift

between the SPION-laden region and its surrounding found in the first study, was also present in the animal model. The MMUS image is displayed in panel E. Only displacement occurring at nanoparticle frequency and phase (± 0.35 radians) is accepted as magnetomotive displacement and its magnitude is displayed as color-code. Note the different color bars in panel C and E.

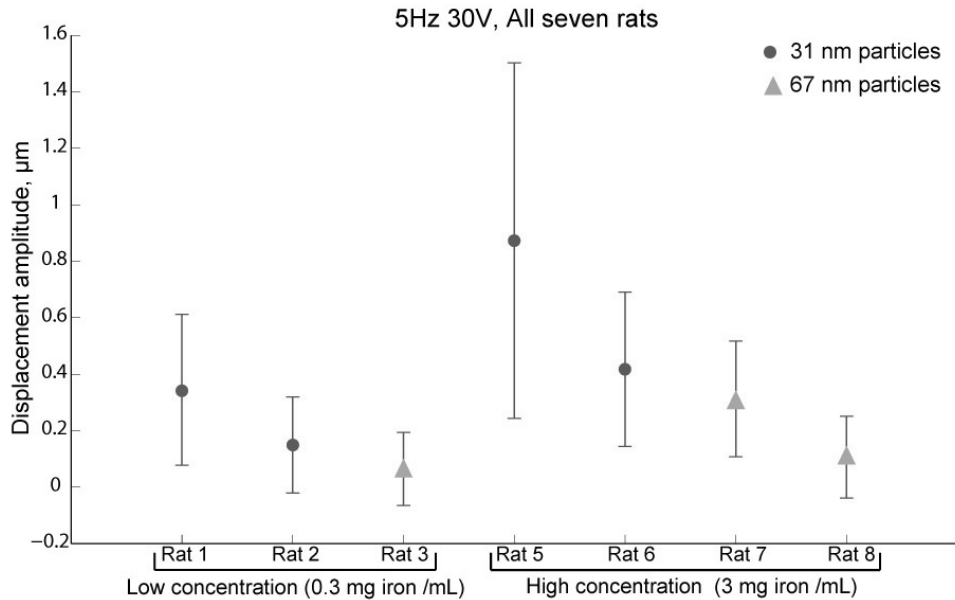


Figure 8. The magnetomotive displacement magnitude for each rat at 5 Hz, 30 V is seen in the image. A larger displacement for both higher nanoparticle concentration and a smaller particle can be seen. The error bars indicate sample standard deviation.

3.4 Paper IV

In this study, experimental data, from both the phantom model in paper I, and the post mortem lymph node in paper III, was compared with data from simulations with the same geometry as the experimental setups. The sinusoidal magnetic force acting on particles was in the simulation modeled as deriving from a coil with a cone shaped iron core, and applied as a body load in nanoparticle-laden regions. The out-of-phase movement, next to the nanoparticle-laden regions found in study I and III, was also present in the simulations. This indicated that the displacement is a result of mechanical coupling from movement of nanoparticle-laden regions, and not diamagnetic response, which was previously suggested by Oldenburg et al [80]. In the phantom, there was a minor mismatch in the alignment of the movement. Potential sources of errors can be that simulated slip condition at the boundaries is probably a combination of slip and stick due to friction, a slight difference of the nanoparticle laden inserts in horizontal position between the phantom and simulation and also difference in material parameters (Fig. 9). Both the experimental and simulation results showed the largest movement in the insert with the lowest particle concentration, which was positioned just above the iron core tip. The results from lymph node model were in agreement (Fig. 10).

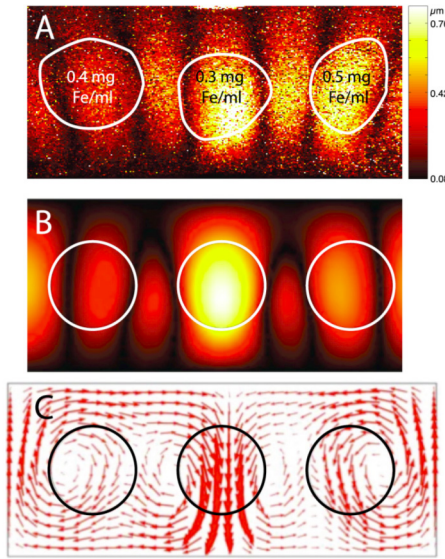


Figure 9. Detected magnetomotive displacement in the experimental setup (A) and in the simulation (B and C). Panel A and B are color-coded in regard with displacement, where white is maximum displacement. In Panel C, the arrows show the direction of the displacement and the size of the arrow indicates the magnitude of the displacement at the given location. The black open triangle below the center insert indicates the position of the iron core tip from which the magnetic field is extending. The largest displacement was found in the insert with the lowest concentration of SPIONs, which was positioned just above the iron core tip. A slight mismatch in the alignment of the tilt of the SPION-laden areas can be seen between the experimental and simulation results,

attracting towards or tilting away from the tip, respectively. This is probably a result of the modeled slip condition tangentially to the surface, which in reality presumably is a combination of slip and stick due to friction.

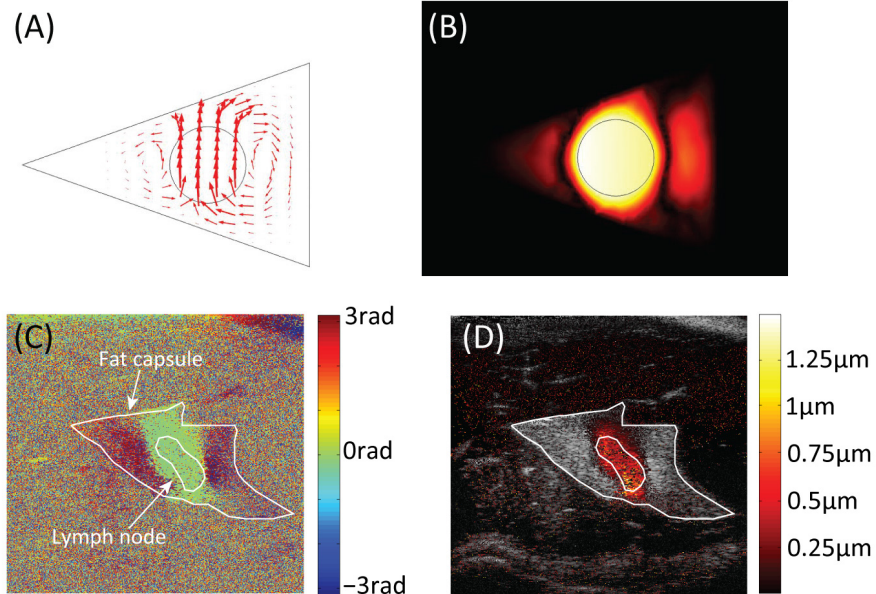


Figure 10. Detected magnetomotive displacement in simulation (A and B) and experiment (D) and the phase distribution at the nanoparticle displacement frequency (C) in the *post mortem* lymph node. The sphere in panel A represents the SPION-laden lymph node, whereas the triangular region represents the surrounding fat capsule. The arrows show the direction of the displacement and the size of the arrows indicate the magnitude of the displacement. Panel B shows the simulated MMUS displacement as a color code, where black is no displacement and white is maximum displacement. MMUS displacement can be seen in the fat capsule in both panel A and B. Panel A reveals that the main component of this displacement has opposite direction (i.e. opposite phase) compared to the displacement in the lymph node. In panel C, the phase distribution at the nanoparticle oscillating frequency is shown. A π radians phase shift can be seen between the outlined lymph node and the surrounding fat capsule. Panel D shows a MMUS image, color-coded according to the bar on the right hand side of the panel. Only pixels with displacements with the same frequency and phase (± 0.35 radians) as the nanoparticles are color-coded.

3.5 Paper V

In paper V, the algorithm was for the first time evaluated *in vivo* and it was the first *in vivo* study where imaging of SPIONs was made with a harmonic magnetic field. The same clinical SLN model as in paper III was used. All three Wistar rats included in the study were successfully imaged with MMUS. The rats were injected with different concentrations of nanoparticles (0.1, 0.2 and 0.3 mg Fe/ml) and the magnetic field was varied by applying an electrical signal with different voltages and frequencies to the solenoid, creating the magnetic field. The study showed that for a higher concentration of nanoparticles, a lower magnetic coil excitation voltage could be used in order to create a magnetomotive displacement of a certain amplitude (e.g. increasing the voltage from 20V to 50V resulted in a 56.6% larger MMUS displacement). The mean signal-to-clutter-ratios (SCR), defined as magnetomotive displacement magnitude in the lymph node divided by that in the rest of the ultrasound image, were calculated to 15.5 ± 5.1 dB, 17.4 ± 6.9 dB and 16.8 ± 6.2 dB for the three rats (conc. 0.1, 0.2 and 0.3 mg Fe/ml), respectively.

For each lymph node, ultrasound images in six different cross sections were collected. An uneven concentration distribution of nanoparticles in the SLN was found when analyzing the data. The maximum MMUS displacement difference between two different cross sections within the same SLN was 9.76 times.

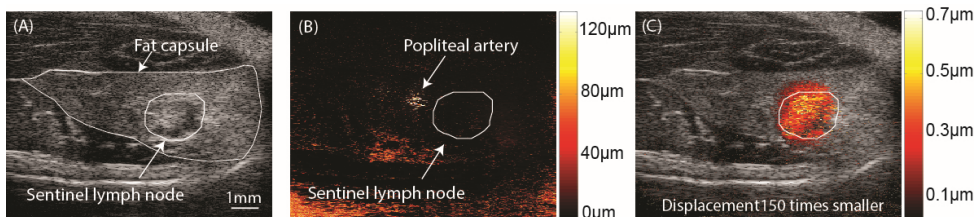


Figure 11. The SLN in the animal injected with the highest concentration (0.3 mg Fe/ml) at magnetic field excitation voltage 5 Hz 35 V. Panel A shows a B-mode image of the SLN and its surrounding fat capsule. The total movement, i.e. movement at all frequencies and phases is superimposed as a color code on the B-mode image in panel B. The white area to the left of the SLN is the popliteal artery. By using the algorithm, the MMUS image in panel C is obtained. Only pixels showing displacements with the same frequency and phase (± 0.35 radians) as the applied magnetic field are color-coded. Note the scales on the color bars, the maximum displacement is more than 150 times larger in panel B than panel C. The SCR in panel C was 23.3 dB.

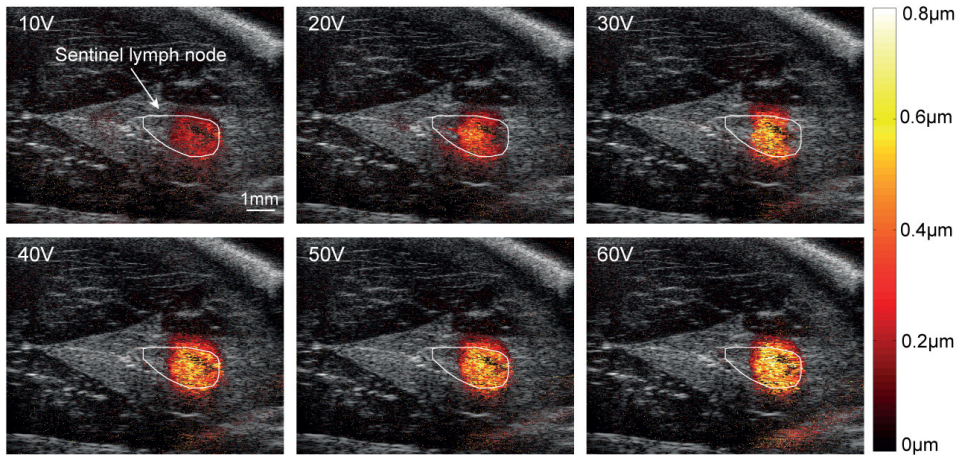


Figure 12. MMUS images of one cross section in the rat injected with the middle concentration of SPIONs, when the voltage is altered from 10V or 60 V. To give the ability to compare the magnetomotive displacement at different voltages, the color scale is identical for all images with the brightest color corresponding to a displacement magnitude of 0.8 μm . All pixels showing larger displacements were set to 0.8 μm . It can be seen from the images that the MMUS signal increases with a higher magnetic field voltage.

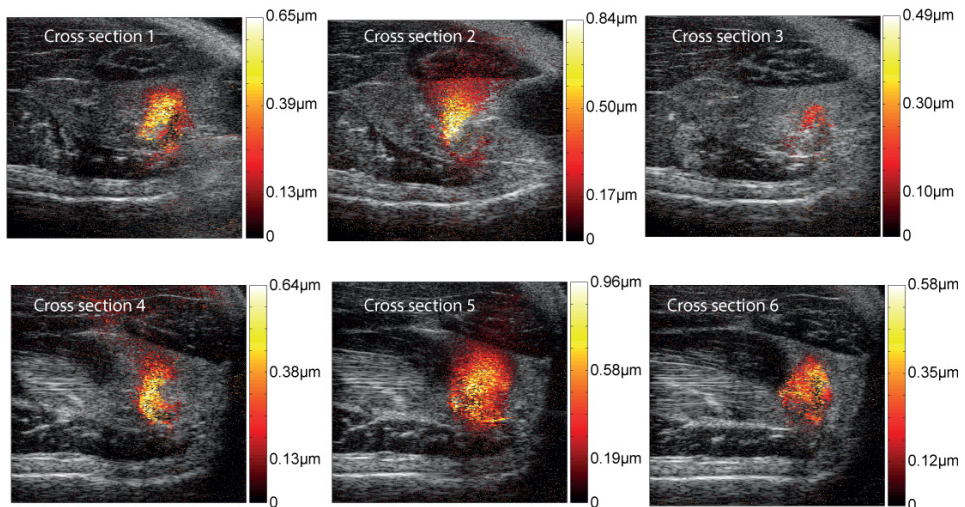


Figure 13. MMUS images of six different cross sections in the high concentration animal, three horizontal and three vertical. The images clearly indicates an uneven concentration of SPIONs, since the magnetomotive signal varies a lot between the different cross sections.

3.6 Paper VI

A multimodal *in vivo* study, combining MMUS with PET/CT and MRI was demonstrated herein. A clinical relevant situation for SLN surgery was set up; one hour post ^{68}Ga -SPIONs injection, whole body PET/CT scanning was performed, then two to four days later, the SPION-laden SLNs were imaged with MMUS. To evaluate the nanoparticle content in each lymph node, MRI scanning of the removed lymph nodes was performed. To our knowledge, this was the first time these techniques were used together. All SLNs were detectable in the PET images. Four of six SLNs could be detected with MMUS. In turn, the MRI measurements showed that the two lymph nodes undetectable with MMUS, contained the lowest concentrations of particles. The four rats detectable with MMUS, were in close agreement with the MRI measurements (correlation coefficient of 0.999 and p-value = 0.001). Also in this study, an uneven distribution of nanoparticles was found in the SLN when analysing the MMUS images. By examination of the eviscerated SLNs, it could be seen that the particles were disseminated in the rim of the SLN as black stripes, see Fig. 15.

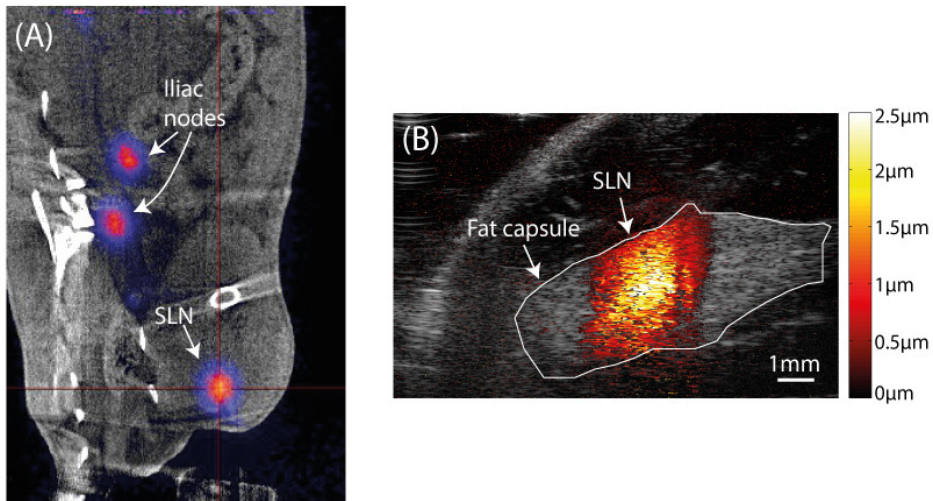


Figure 14. Panel (A), a coronal PET/CT image of animal 1. The center of the red cross shows the position of the SPION-accumulated SLN. SPION accumulation is also seen in two iliac lymph nodes. Panel (B), MMUS image of the SLN in same animal. The fat capsule surrounding the lymph node is outlined in the image. The induced magnetomotive displacement, shown as color code in the image, reveals the location of the SLN.

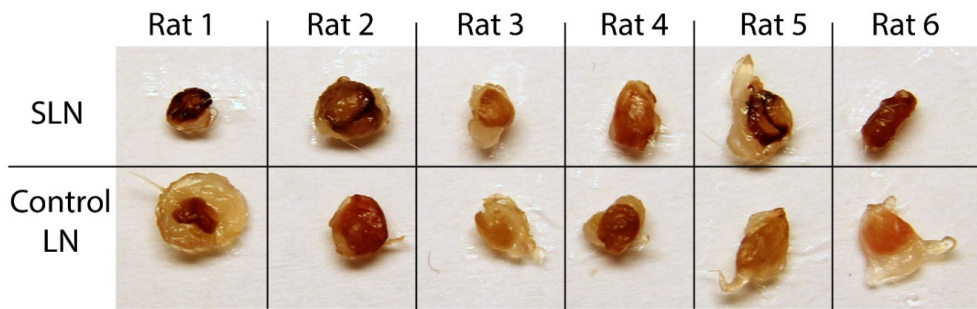


Figure 15. Photographic image of the eviscerated SLNs (top row) and control nodes (bottom row). The SLN is darker in all cases except from in animal 4. The darker color indicates the presence of SPIONs. Black stripes of SPIONs can be seen in animal 1, 2 and 5. The semi-transparent parts, that partly surround some of the lymph nodes, are remains of the fat capsule.

4. DISCUSSION

In the beginning of 2010, when this doctoral work begun, MMUS had more or less just been presented and only a few studies were performed with this novel technique [44, 46, 48]. The possibilities and potential of the technique was thereby unknown and the overall aim of the thesis was set to investigate the concept of MMUS and evaluate its feasibility for *in vivo* use.

The algorithm developed paper I, has shown to be very sensitive. In all studies, displacement in the sub-micrometer range has been detected. Although displacement artifacts have been more than two orders of magnitudes larger than the MMUS signal, the algorithm has been able to clearly highlight the location of the nanoparticles (e.g. paper III and V).

The magnetomotive displacement is affected by many parameters such as the magnetic field excitation, nanoparticle concentration, the geometry and size of the particles, susceptibility of the particles and the elasticity of the surrounding medium. In the studies here within, the first three parameters have been altered in order to obtain a better understanding of their influence on the nanoparticle displacement.

Both the frequency and the voltage applied on the solenoid creating the magnetic field have been altered. The displacement was observed to decrease with frequency. The main reason is most likely due to the solenoid's increasing impedance with frequency. The contribution from the viscoelastic response of tissue may also be a part of explanation.

An increased displacement was found with increased voltage. In study V and VI, the solenoid and iron core was exchanged and the magnetic flux density could be increased from 0.18 T to 0.41 T. The shape of iron core was also reformed in order to form a more homogeneous field in the image plane. These changes also resulted in a higher magnetomotive displacement.

In 2013, Mehrmohammadi et al. presented a study where they used zinc-doped SPIONs with a saturation magnetization of 161 emu/g (Zn+Fe) instead of around 50 emu/g (Fe) which is a typical saturation magnetization of clinically used Fe_3O_4 particles (e.g. Feridex). Phantoms with nanoparticle inclusions (concentration of 0.5 and 1.0 mg Fe/ml) were made, one containing zinc-doped nanoparticles and one containing Feridex nanoparticles. Signal increments of 277 % and 225 % respectively, were found using zinc-doped particles [59]. Metal-doped SPIONs may be a better MMUS contrast agent of choice instead of ordinary SPIONs. However, these nanoparticles come with higher safety concerns since their toxicity profile is not as well studied as the non-doped SPIONs, already in use in the clinic.

The magnitude of the displacement in all the papers included in this thesis, is noteworthy smaller than what other MMUS groups have presented. The maximum MMUS displacement detected by us has been barely 3 μm (but usually around 0.5 μm), whereas others in the field, who have presented their results in units of length, have reported displacements of tens [50, 58, 59, 61] or even up to hundreds of micrometers [48, 56]. The reason for the difference in displacement is not fully understood. Two main factors differentiating these groups from us are the magnitude of the magnetic flux density (**B**) and the applied signal to the coil generating the magnetic field, being pulsed or harmonic. The magnetic flux density used by other groups was approximately 2-3 times larger (except from the setup in paper V and VI where the magnetic flux density was doubled, when using a new solenoid and iron core). This affects the resulting MMUS displacement, but not possible to the degree reflected in the difference in magnitude. By applying a pulse instead of a harmonic signal, a larger amount of instantaneous energy can be applied on the solenoid due to the smaller amount of total heat developed. This also affects the magnitude on MMUS displacement.

An additional factor affecting the magnitude of the displacement is the viscoelasticity of the nanoparticle-laden regions and their surroundings. The viscoelasticity is an unknown parameter in most MMUS studies, both others, and ours, and is thereby not possible to take in to account in this discussion. Nevertheless, since malignant tissue is harder than healthy tissue, this is a parameter that could have potential diagnostic value. As the MMUS technique induces a displacement in the tissue, a dynamic response will follow. Translating this response to viscoelasticity, may open up non-invasive detection of metastatic infiltration with the MMUS technique.

In potential clinical use, the increased generation of heat created when a harmonic field is used (produced by inductance in the solenoid), may make it necessary to introduce some sort of solenoid cooling system. But in the studies included in this thesis no cooling of the magnet has been needed. Advantages using a harmonic magnetic field are the ability to obtain a better signal-to-noise/background ratio and also make the measurement more robust against motion artifacts. As a very high framerate is needed to sample the tissue movement produced by a pulsed magnetic field (kHz), new ultrasound scanners (or implementation of software) and transducers are required since conventional ultrasound machines operate at a framerate of approximately 100 Hz. This might not be a problem in the future since other ultrasound applications, such as vector Doppler, also require high framerate, but for the moment these machines are not in clinical use.

Simulations were performed in order to verify experimental findings (paper II and IV) and to obtain a better understanding of the MMUS displacement. In paper II an attempt to normalize the inhomogeneous magnetic field was done with the purpose to provide more accurate information about the magnetic particle content throughout the ultrasound image during MMUS imaging. But the simulation and experiments did not agree as well as predicted. The absence of displacement at the edges of phantom showed that a more

complex simulation model has to be developed in order to obtain a better accuracy of the nanoparticle concentration. This model has to take the boundary conditions in to account.

In paper IV, both the phantom model from paper I and post mortem lymph node from paper III were evaluated in a simulation model. The π radians out of phase movement found in the experimental setups was also found in the simulations. It has been discussed whether this movement is a result of mechanical coupling between the nanoparticle-laden areas and their surrounding or if it is a diamagnetic response of the background material, where we have argued for the first viewpoint. In the simulation the magnetic force was applied as a body load on the nanoparticle-laden areas and a large out of phase displacement was still present. In addition, no diamagnetic response was found when examining a phantom free from SPIONs (paper I), as well as in the control lymph node in the *post mortem* case (paper III). Thereby, we believe that the mechanical coupling is the main contributor to the movement. Whether the out-of-phase movement can contribute with elasticity information of the SPION-laden tissue is still an open question.

The SPION-laden inserts in the phantom (both experimental and simulations) were arranged with the insert containing the lowest concentration SPIONs positioned just above the iron core tip, whereas inserts with higher concentration were positioned on the sides. The result showed that the highest MMUS-displacement was found in the low concentration insert. This indicates, as suggested in paper II, that a normalization of the magnetic field is needed in order to achieve a fair representation of the concentration distribution of nanoparticles. However, considering the effect of boundary conditions the normalization process may need to be more complex than first assumed and the approach to solve this remains to be found out.

An investigation of the potential for *in vivo* use of the algorithm and MMUS, was performed in three animal studies (paper III, paper V and paper VI), where two of them also were multimodal (paper III and VI). The sentinel lymph node rat model, described earlier in section 2.3, was used. In all three studies SPION-laden lymph nodes were successfully imaged, showing that the algorithm and the MMUS technique have the potential to be used *in vivo*.

To exclude artifactual movements, such as respiration and heart beats, which could interfere with the magnetomotive displacement, the experiments in study III were made *post mortem*.

In the study, two sizes of the PEG-coating, surrounding the 11 nm iron core were used, resulting in particles with diameters of 31 or 67 nm. For the smaller particles, a larger MMUS displacement in the ultrasound data and a larger hypoenhancement in the MRI images, were found. This indicated a higher accumulation of 31 nm particles in the SLN. The reason for this is probably due to faster accumulation of the smaller particles in SLN, which have earlier been seen by Kjellman et al. [42].

Study V was performed to investigate the algorithm's potential to suppress those *in vivo* artifacts which were avoided in study III. It was shown that motion artifacts more than 150 times larger than the MMUS signal, could be suppressed and the SPION-laden SLNs were clearly highlighted in the ultrasound images using the algorithm. To be able to take the technique to the clinic in the future, this is necessarily.

In the last animal study (paper VI), a clinical scenario was implemented, where preoperative staging with PET/CT was performed one hour post injection of SPIONs, followed by MMUS imaging 2-4 days later. Thereafter the SLNs were removed from the animals and imaged with high-resolution MRI. All animals were detected with PET/CT whereas MMUS-signal was found in four of six animals.

The concentration of the 100 μ l injected SPION solution, was varied between 0.1 and 4 mg Fe/ml, in the *in vivo* studies. All animals in paper V, injected with 0.1-0.3 mg Fe/ml could be imaged with MMUS, whereas in paper VI, no MMUS signal was found in two out of six animals, injected with 1 and 2mg Fe/ml respectively. The actual amount of nanoparticles accumulated in the SLN is not known, but considering the injected concentrations, the accumulation is assumed to be larger in the animals in study VI. The PET images of the two not detectable animals showed a radioactive contamination on the belly of one of these animals and in the other animal, PET signal was observed in the liver, indicating leakage of the ^{68}Ga -labeled SPIONs into the bloodstream. The MRI images confirmed that the concentration of accumulated SPIONs was lowest in these two animals, where no MMUS signal could be observed.

It would be desirable to determine a lower SPION detection limit for *in vivo* MMUS imaging. Thereby the particle concentration in all studies has been altered, with the purpose obtain an indication of what this limit could be. But since a multitude of parameters affect the displacement (e.g. magnetic flux density, the elasticity of the surrounding media, the properties of the magnetic probes) and the accumulation of the nanoparticles (e.g. drainage from the injection site, the nanoparticle uptake in the SLN), as well as unpredictable events as in study VI may occur, it may be hard to determine.

In the phantom setup in study I, no MMUS displacement was found in the 0.3mg Fe/ml insert. The detection limit was in this study set to 0.45g Fe/ml, as this was the second lowest concentration used. Instead, in study V, MMUS-displacement was found in the animal injected with 0.1 mg Fe/ml. As approximately less than 10 % of the injected dose of SPIONs ends up in the SLN [36], the concentration in the SLN should be around 0.01 mg Fe/ml. There seems to be other factors in play and additional measurements have to be made in order obtain a better understanding of the detection limit.

The MMUS images in study V (Fig. 13) and VI showed an uneven distribution of nanoparticles in the SLN. In study VI, the SLNs and control lymph nodes (node in the contralateral knee) were removed from the animals to investigate the distribution. A color

difference between SLN and control node could be seen in all animals (Fig. 15). In the SLNs with the highest concentration of particles according to the MRI measurements (animal 1, 2 and 5), the SPIONs appeared as black stripes on the outer rim. This type of SPION distribution has earlier been reported by Kjellman et al. [13]. As a result of the uneven distribution, more than one cross section should be imaged with MMUS, not to miss the MMUS signal.

The progress in the molecular imaging field has resulted in an increased need to combine several imaging modalities to obtain both the high sensitivity and the high anatomical resolution which are required [32]. In paper III, MRI and MMUS were combined. This paper was a proof of principle for harmonic MMUS imaging in animals, and it showed that it was possible to use the same contrast agent with these two modalities.

In paper VI, MMUS, PET/CT and MRI were combined. The aim with the paper was to build up a possible clinical scenario and evaluate the possibility of MMUS to be used as an intraoperative guide during sentinel lymph node surgery after preoperative staging with combined PET/CT. MRI was in this study only used to evaluate the amount of SPIONs in the lymph nodes, so a comparison against the MMUS results could be made. But to obtain a better soft tissue resolution in the preoperative images, PET/MRI would preferably be used as the preoperative staging technique instead of PET/CT, as employed in this study.

Both study III and IV presented positive MMUS results, whereas study VI showed that MRI and PET were more sensitive detecting the ^{68}Ga -SPIONs than MMUS. There seems to be a detection threshold in MMUS, which does not occur to the same extent in the other modalities, but above this limit the results are in good compliance (MRI and MMUS - to compare PET and MMUS is not relevant since they image different processes and at different times). However, the MMUS technique is still developing and additional studies are required to obtain a better understanding how various parameters affect the displacement and detection of SPIONs. All animal studies performed in this thesis are more or less a proof-of-concept of *in vivo* use of the technique and our algorithm, and investigations how to make the imaging setup more sensitive have to be done. Examples of areas of improvements are algorithm modification, enhancement of the magnetic flux density and using nanoparticles with properties increasing the magnetic force acting on the particles, e.g. higher susceptibility.

The design of the sentinel lymph node model used herein sets the popliteal lymph node to be the SLN. In breast cancer, the SLN is located in the draining nodal basin in the axilla whereas the position of the SLN in malignant melanoma, especially if located at the abdomen, might be in many locations stretching from the neck to the groin [78]. Depending on the situation, the choice of imaging modalities used to identify the SLN/SLNs may be altered. In case of malignant melanoma whole-body preoperative staging would probably be preferable (performed with e.g. PET/MRI or PET/CT),

whereas in breast cancer, where the SLN location is restricted to a smaller area, MMUS may in the future be able to work as a stand-alone imaging technique.

Since the SLN model was used to evaluate MMUS *in vivo* in this thesis, much attention has been given to this application of using MMUS. However, the results in this thesis point in the direction that MMUS has potential to be used as a standalone modality for other imaging applications aside from a pre-operative guide for the surgeon during SLN detection and removal. Especially if the magnetic nanoparticles are functionalized with targeting molecules, so they can be used target specific molecular imaging. Such potential applications is e.g. in cardiovascular research, monitoring the progression and treatment of atherosclerotic plaque, and also to image stem cell propagation and migration.

5. FUTURE WORK

Even though the results from this thesis show a promising future for the MMUS technique, there is some way to go before clinically use may be possible. Many more measurements and simulations have to be performed in order to develop an understanding how different parameters affect the displacement and also to be able to build up a sensitive system with a low nanoparticle concentration detection dose. Also a safety analysis has to be performed.

The dynamic response of the nanoparticle-induced displacement is most likely coupled with the viscoelasticity of the surrounding media. Since malignant tissue is stiffer than normal tissue, finding a relationship between the magnetomotive tissue response and elasticity could result in a non-invasive way, analyzing malignancy of tissue using only MMUS as a standalone technique.

In order to obtain a better estimation of the distribution of the nanoparticles a normalization of the magnetic field needs to be performed, either by software or hardware solutions. This may for example be of importance when evaluating the concentration nanoparticles in drug-delivery applications.

Further, to be able to take the technique to the clinic, a new probe design that would facilitate the magnetic field excitation has to be developed. Since the magnetic field decreases with distance from the magnet field generator, it is desirable to have the nanoparticle-laden area as close to the magnet field generator as possible. Thus, a design is needed where the magnetic field is applied from the same side as the ultrasound probe.

6. CONCLUSION

In this thesis, a magnetomotive ultrasound imaging algorithm has been developed and evaluated successfully in phantom studies (study I, II and IV) and animal studies, both post mortem (paper III) and *in vivo* (study V and VI). Additionally, to investigate the induced magnetomotive displacement, the experimental findings have been verified in simulations (paper II and IV).

In all studies the algorithm has been capable to sort out the MMUS signal and pinpoint the location of the SPION-laden areas, even though the nanoparticle displacement has been small (in the order of sub-micrometers) and the motion artifacts from heart and blood flow have been substantially larger.

To evaluate MMUS in a clinical relevant situation, a sentinel lymph node model was in this thesis chosen, where MMUS served as a complementary imaging modality to standard methods, providing high-resolution bedside guidance for the surgeon during SLN surgery. However, the MMUS technique has also shown to have potential to be used as a non-invasive stand-alone imaging technique. Labelling the magnetic nanoparticles with disease targeting molecules, a new dimension of possibilities and field of applications would open up for MMUS. Both in cancer research, localizing metastatic infiltration prior to cancer surgery and also in other clinical applications such as cardiovascular research and drug-delivery.

7. REFERENCES

1. Massoud, T.F. and S.S. Gambhir, *Molecular imaging in living subjects: seeing fundamental biological processes in a new light*. Genes Dev, 2003. 17(5): p. 545-80.
2. Saraste, A., S.G. Nekolla, and M. Schwaiger, *Cardiovascular molecular imaging: an overview*. Cardiovasc Res, 2009. 83(4): p. 643-52.
3. Hauff, P., et al., *Molecular targeting of lymph nodes with L-selectin ligand-specific US contrast agent: a feasibility study in mice and dogs*. Radiology, 2004. 231(3): p. 667-73.
4. Weissleder, R. and U. Mahmood, *Molecular imaging*. Radiology, 2001. 219(2): p. 316-33.
5. Minchin, R.F. and D.J. Martin, *Nanoparticles for molecular imaging--an overview*. Endocrinology, 2010. 151(2): p. 474-81.
6. O'Donnell, M., et al., *Can molecular imaging enable personalized diagnostics? An example using magnetomotive photoacoustic imaging*. Ann Biomed Eng, 2013. 41(11): p. 2237-47.
7. Christiansen, J.P. and J.R. Lindner, *Molecular and Cellular Imaging With Targeted Contrast Ultrasound*. Proceedings of the IEEE, 2005. 90(4): p. 809-818.
8. Haidekker, M.A., *Medical Imaging Technology*. 2013: Springer
9. Beyer, T., et al., *The future of hybrid imaging-part 2: PET/CT*. Insights Imaging, 2011. 2(3): p. 225-34.
10. Beyer, T., et al., *The future of hybrid imaging-part 1: hybrid imaging technologies and SPECT/CT*. Insights Imaging, 2011. 2(2): p. 161-9.
11. Beyer, T., et al., *A combined PET/CT scanner for clinical oncology*. J Nucl Med, 2000. 41(8): p. 1369-79.
12. Sato, A., B. Klaunberg, and R. Tolwani, *In vivo bioluminescence imaging*. Comp Med, 2004. 54(6): p. 631-4.
13. Choy, G., P. Choyke, and S.K. Libutti, *Current advances in molecular imaging: noninvasive in vivo bioluminescent and fluorescent optical imaging in cancer research*. Mol Imaging, 2003. 2(4): p. 303-12.
14. Doiron, A.L., et al., *Poly(lactic-co-glycolic) acid as a carrier for imaging contrast agents*. Pharm Res, 2009. 26(3): p. 674-82.
15. Sivasubramanian, M., Y. Hsia, and L.W. Lo, *Nanoparticle-facilitated functional and molecular imaging for the early detection of cancer*. Front Mol Biosci, 2014. 1: p. 15.
16. Lanza, G.M., et al., *Magnetic resonance molecular imaging with nanoparticles*. J Nucl Cardiol, 2004. 11(6): p. 733-43.
17. Chen, T.J., et al., *Targeted Herceptin-dextran iron oxide nanoparticles for noninvasive imaging of HER2/neu receptors using MRI*. J Biol Inorg Chem, 2009. 14(2): p. 253-60.

18. Margolis, D.J., et al., *Molecular imaging techniques in body imaging*. Radiology, 2007. 245(2): p. 333-56.
19. Strauss, L.G., *Fluorine-18 deoxyglucose and false-positive results: a major problem in the diagnostics of oncological patients*. Eur J Nucl Med, 1996. 23(10): p. 1409-15.
20. Hoskins, P., K. Martin, and A. Thrush, *Diagnostic Ultrasound Physics and equipment*. 2010, Cambridge university press.
21. Gessner, R. and P.A. Dayton, *Advances in molecular imaging with ultrasound*. Mol Imaging, 2010. 9(3): p. 117-27.
22. Frangioni, J.V., *New technologies for human cancer imaging*. J Clin Oncol, 2008. 26(24): p. 4012-21.
23. Goldberg, B.B., J.S. Raichlen, and F. Forsberg, *Ultrasound contrast Agents Basic principles and clinical applications* 2001: Martin Dunitz Ltd.
24. Unnikrishnan, S. and A.L. Klibanov, *Microbubbles as ultrasound contrast agents for molecular imaging: preparation and application*. AJR Am J Roentgenol, 2012. 199(2): p. 292-9.
25. Deshpande, N., A. Needles, and J.K. Willmann, *Molecular ultrasound imaging: current status and future directions*. Clin Radiol, 2010. 65(7): p. 567-81.
26. Voigt, J.U., *Ultrasound molecular imaging*. Methods, 2009. 48(2): p. 92-7.
27. Lindner, J.R., *Contrast ultrasound molecular imaging of inflammation in cardiovascular disease*. Cardiovasc Res, 2009. 84(2): p. 182-9.
28. Demos, S.M., et al., *In vivo targeting of acoustically reflective liposomes for intravascular and transvascular ultrasonic enhancement*. J Am Coll Cardiol, 1999. 33(3): p. 867-75.
29. Lanza, G.M., et al., *In vivo molecular imaging of stretch-induced tissue factor in carotid arteries with ligand-targeted nanoparticles*. J Am Soc Echocardiogr, 2000. 13(6): p. 608-14.
30. Shin, T.H., et al., *Recent advances in magnetic nanoparticle-based multi-modal imaging*. Chem Soc Rev, 2015. 44(14): p. 4501-16.
31. Jansson, T., et al., *Superparamagnetic iron oxide nanoparticles as a multimodal contrast agent for up to five imaging modalities*. Clin Transl Imaging, 2015. 3: p. 247-249.
32. Sauter, A.W., et al., *Combined PET/MRI: one step further in multimodality imaging*. Trends Mol Med, 2010. 16(11): p. 508-15.
33. Mulder, W.J., et al., *Quantum dots with a paramagnetic coating as a bimodal molecular imaging probe*. Nano Lett, 2006. 6(1): p. 1-6.
34. Shibu, E.S., et al., *Photouncaging nanoparticles for MRI and fluorescence imaging in vitro and in vivo*. ACS Nano, 2013. 7(11): p. 9851-9.
35. Lang, N., et al., *Hybrid 3D Sono/PET in a mouse*. Eur J Nucl Med Mol Imaging, 2007. 34(10): p. 1706-7.
36. Madru, R., et al., *(68)Ga-labeled superparamagnetic iron oxide nanoparticles (SPIONs) for multi-modality PET/MR/Cherenkov luminescence imaging of sentinel lymph nodes*. Am J Nucl Med Mol Imaging, 2013. 4(1): p. 60-9.

37. Mehrmohammadi, M., et al., *Pulsed magneto-motive ultrasound imaging using ultrasmall magnetic nanoprobes*. Mol Imaging, 2011. **10**(2): p. 102-10.
38. Bao, G., S. Mitragotri, and S. Tong, *Multifunctional nanoparticles for drug delivery and molecular imaging*. Annu Rev Biomed Eng, 2013. **15**: p. 253-82.
39. Nune, S.K., et al., *Nanoparticles for biomedical imaging*. Expert Opin Drug Deliv, 2009. **6**(11): p. 1175-94.
40. Albanese, A., P.S. Tang, and W.C. Chan, *The effect of nanoparticle size, shape, and surface chemistry on biological systems*. Annu Rev Biomed Eng, 2012. **14**: p. 1-16.
41. Liu, J., et al., *Nanoparticles as image enhancing agents for ultrasonography*. Phys Med Biol, 2006. **51**(9): p. 2179-89.
42. Kjellman, P., et al., *Optimizing retention of multimodal imaging nanostructures in sentinel lymph nodes by nanoscale size tailoring*. Nanomedicine, 2014. **10**(5): p. 1089-95.
43. Qiao, R., C. Yang, and M. Gao, *Superparamagnetic iron oxide nanoparticles: from preparations to in vivo MRI applications*. J. Mater. Chem 2009. **19**: p. 6274-6293.
44. Oh, J., et al., *Detection of magnetic nanoparticles in tissue using magneto-motive ultrasound*. Nanotechnology, 2006. **17**(16): p. 4183-4190.
45. Mariappan, L., et al., *Magneto acoustic tomography with short pulsed magnetic field for in-vivo imaging of magnetic iron oxide nanoparticles*. Nanomedicine, 2015.
46. Mehrmohammadi, M., et al., *Imaging of iron oxide nanoparticles using magneto-motive ultrasound*. 2007 Ieee Ultrasonics Symposium Proceedings, Vols 1-6, 2007: p. 652-655.
47. Madru, R., et al., *99mTc-labeled superparamagnetic iron oxide nanoparticles for multimodality SPECT/MRI of sentinel lymph nodes*. J Nucl Med, 2012. **53**(3): p. 459-63.
48. Mehrmohammadi, M., et al., *Pulsed Magneto-Acoustic Imaging*. 2009 Annual International Conference of the Ieee Engineering in Medicine and Biology Society, Vols 1-20, 2009: p. 4771-4774.
49. Madru, R., et al., *Development of a Hybrid Nanoprobe for Triple-Modality MR/SPECT/Optical Fluorescence Imaging*. Diagnostics (Basel), 2014. **4**(1): p. 13-26.
50. Mehrmohammadi, M., et al., *Enhanced pulsed magneto-motive ultrasound imaging using superparamagnetic nanoclusters*. Nanotechnology, 2011. **22**(4).
51. Fink, M., et al., *Sonographic Detection of Magnetic Nanoparticles for Magnetic Drug Targeting in Weak Echogenic Tissue*. Proc. IEEE Ultrasonics Symp., 2015.
52. Cobbold, R., *Foundations of biomedical ultrasound*. 2007: Oxford university press.
53. Mallidi, S., G.P. Luke, and S. Emelianov, *Photoacoustic imaging in cancer detection, diagnosis, and treatment guidance*. Trends Biotechnol, 2011. **29**(5): p. 213-21.
54. Oldenburg, A.L., et al., *Magnetomotive contrast for in vivo optical coherence tomography*. Optics Express, 2005. **13**(17): p. 6597-6614.

55. Schenck, J.F., *Safety of strong, static magnetic fields*. J Magn Reson Imaging, 2000. 12(1): p. 2-19.
56. Mehrmohammadi, M., et al., *Pulsed Magneto-motive Ultrasound Imaging Using Ultrasmall Magnetic Nanoprobes*. Molecular Imaging, 2011. 10(2): p. 102-110.
57. Griffiths, D.J., *Introduction to electrodynamics*. 1999: Prentice-Hall.
58. Mehrmohammadi, M., et al., *Pulsed magneto-motive ultrasound imaging to detect intracellular trafficking of magnetic nanoparticles*. Nanotechnology, 2011. 22(41): p. 415105.
59. Mehrmohammadi, M., et al., *In vivo pulsed magneto-motive ultrasound imaging using high-performance magnetoactive contrast nanoagents*. Nanoscale, 2013. 5(22): p. 11179-11186.
60. Pope, A.G., et al., *Contrast-enhanced imaging of SPIO-labeled platelets using magnetomotive ultrasound*. Physics in Medicine and Biology, 2013. 58(20): p. 7277-7290.
61. Ting, P.-H., et al., *Ultrafast Plane Wave Imaging Based Pulsed Magnetomotive Ultrasound*. Proc. IEEE Ultrasonics Symp., 2014.
62. Huang, Y.-C., et al., *Ultrafast pulsed magnetomotive ultrasound imaging of sentinel lymph nodes: Small animal study*.
63. Fink, M., et al., *Sonographic Detection of Nanoparticles used for Magnetic Drug Targeting*. Proc. Sensor, 2015: p. 430-435.
64. Almeida, T.W., et al., *Comparison between shear wave dispersion magneto motive ultrasound and transient elastography for measuring tissue-mimicking phantom viscoelasticity*. IEEE Trans Ultrason Ferroelectr Freq Control, 2015. 62(12): p. 2138-45.
65. Pavan, T.Z., et al., *Ultrasound-based transient elastography using a magnetic excitation*. Proc. IEEE Ultrasonics Symp. , 2012: p. 1846 - 1849.
66. Bruno, A.C., et al., *A hybrid transducer to magnetically and ultrasonically evaluate magnetic fluids*. IEEE Trans Ultrason Ferroelectr Freq Control, 2013. 60(9): p. 2004-12.
67. Bruno, A.C., et al., *A hybrid transducer to evaluate stomach emptying by ultrasound and susceptometric measurements: an in vivo feasibility study*. IEEE Trans Ultrason Ferroelectr Freq Control, 2015. 62(7): p. 1288-94.
68. Qu, M., et al., *Magneto-photo-acoustic imaging*. Biomed Opt Express, 2011. 2(2): p. 385-96.
69. Jin, Y., et al., *Multifunctional nanoparticles as coupled contrast agents*. Nat Commun, 2010. 1: p. 41.
70. *World cancer report*. World Health Organization, 2014.
71. Weissleder, R., *Molecular imaging in cancer*. Science, 2006. 312(5777): p. 1168-71.
72. *Immunology of the Lymphatic System* 2013: Springer.
73. Gray-Schopfer, V., C. Wellbrock, and R. Marais, *Melanoma biology and new targeted therapy*. Nature, 2007. 445(7130): p. 851-7.

74. Somasundaram, S.K., D.W. Chicken, and M.R. Keshtgar, *Detection of the sentinel lymph node in breast cancer*. Br Med Bull, 2007. 84: p. 117-31.
75. Morton, D.L. and A.D. Chan, *The concept of sentinel node localization: how it started*. Semin Nucl Med, 2000. 30(1): p. 4-10.
76. Widmaier, E., H. Raff, and K. Strang, *Vander's Human Physiology, the mechanisms of body function* 2014: Mc Gray Hill.
77. Hsueh, E.C. and A.E. Giuliano, *Sentinel Lymph Node Technique for Staging of Breast Cancer*. Oncologist, 1998. 3(3): p. 165-170.
78. Chakera, A.H., et al., *EANM-EORTC general recommendations for sentinel node diagnostics in melanoma*. Eur J Nucl Med Mol Imaging, 2009. 36(10): p. 1713-42.
79. Valsecchi, M.E., et al., *Lymphatic mapping and sentinel lymph node biopsy in patients with melanoma: a meta-analysis*. J Clin Oncol, 2011. 29(11): p. 1479-87.
80. Oldenburg, A.L., et al., *Phase-resolved magnetomotive OCT for imaging nanomolar concentrations of magnetic nanoparticles in tissues*. Opt Express, 2008. 16(15): p. 11525-39.

Paper I

IEEE TRANSACTIONS ON ULTRASONICS, FERROELECTRICS, AND FREQUENCY CONTROL

A PUBLICATION OF THE IEEE ULTRASONICS, FERROELECTRICS, AND FREQUENCY CONTROL SOCIETY



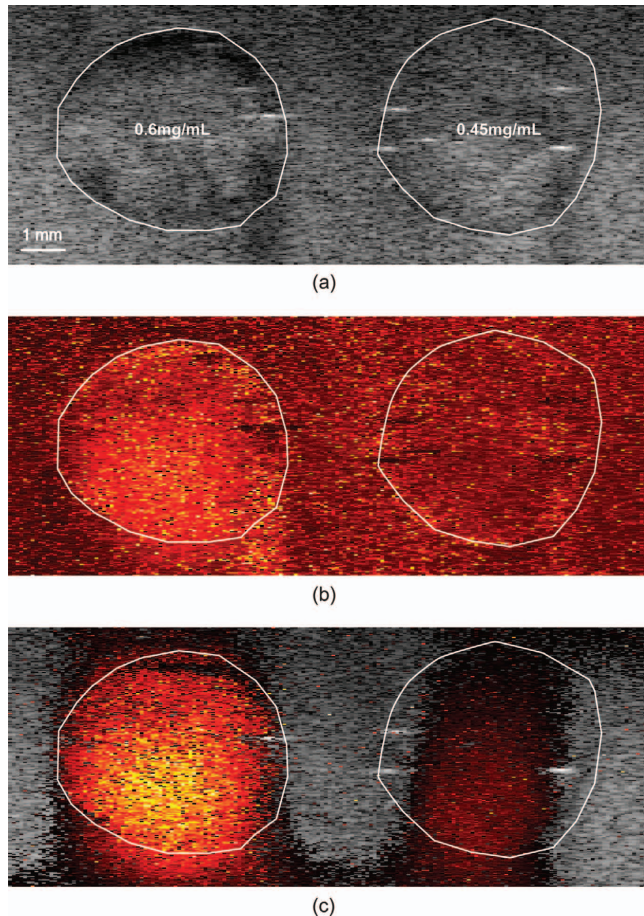
MAY 2013

VOLUME 60

NUMBER 5

ITUCER

(ISSN 0885-3010)



Access the journal with its multimedia contents online
at: <http://www.ieee-uffc.org/tr/>



DOI <http://dx.doi.org/10.1109/TUFFC.2013.2639>



Frequency- and Phase-Sensitive Magnetomotive Ultrasound Imaging of Superparamagnetic Iron Oxide Nanoparticles

These images show suppression of spurious motion signals during magnetomotive ultrasound imaging of a polyvinyl alcohol (PVA) phantom containing superparamagnetic iron oxide nanoparticle inserts (outlined, concentrations: 0.6 and 0.45 mg of $\text{Fe}_3\text{O}_4/\text{mL}$): (a) B-mode image, (b) the total rms displacement (power Doppler processing), and (c) the frequency detected and phase-gated displacement. For further reading, please see M. Evertsson, M. Cinthio, S. Fredriksson, F. Olsson, H. W. Persson, and T. Jansson, “Frequency- and phase-sensitive magnetomotive ultrasound imaging of superparamagnetic iron oxide nanoparticles,” *IEEE Trans. Ultrason. Ferroelectr. Freq. Control.*, vol. 60, no. 3, pp. 481–491, Mar. 2013.

Images courtesy of Maria Evertsson, Magnus Cinthio, Sarah Fredriksson, Fredrik Olsson, Hans W. Persson, and Tomas Jansson. M. Evertsson, M. Cinthio, H. W. Persson, and T. Jansson are with the Department of Electrical Measurements, Faculty of Engineering, Lund University, Lund, Sweden. S. Fredriksson and F. Olsson are with Genovis AB, Lund, Sweden.

Frequency- and Phase-Sensitive Magnetomotive Ultrasound Imaging of Superparamagnetic Iron Oxide Nanoparticles

Maria Evertsson, *Student Member, IEEE*, Magnus Cinthio, *Member, IEEE*, Sarah Fredriksson, Fredrik Olsson, Hans W. Persson, *Member, IEEE*, and Tomas Jansson, *Member, IEEE*

Abstract—It has recently been demonstrated that superparamagnetic iron oxide nanoparticles can be used as magnetomotive ultrasound contrast agents. A time-varying external magnetic field acts to move the particles and, thus, the nanoparticle-laden tissue. However, the difficulty of distinguishing this magnetomotive motion from undesired movement induced in regions without nanoparticles or other motion artifacts has not been well reported. Using a high-frequency linear-array system, we found that displacements outside nanoparticle-laden regions can be similar in magnitude to those in regions containing nanoparticles. We also found that the displacement outside the nanoparticle regions had a phase shift of approximately π radians relative to that in the nanoparticle regions. To suppress signals arising from undesirable movements, we developed an algorithm based on quadrature detection and phase gating at the precise frequency of nanoparticle displacement. Thus, clutter at other frequencies can be filtered out, and the processed signal can be color-coded and superimposed on the B-mode image. The median signal-to-clutter ratio improvement using the proposed algorithm was 36 dB compared with simply summing the movement energy at all frequencies. This clutter rejection is a crucial step to move magnetomotive ultrasound imaging of nanoparticles toward *in vivo* investigations.

I. INTRODUCTION

THE development of contrast agents for ultrasound imaging, as for other imaging technologies, is moving toward molecular imaging. This is the process in which contrast agents are labeled with tumor- or tissue-specific targeting agents, e.g., antibodies, peptides, and aptamers, to make it possible to detect phenomena that occur on a cellular or molecular level. This information is expected to have a major impact on the detection of cancer and cardiovascular disease, the development of drugs and individualized treatment, and our understanding of how diseases arise [1], [2].

Manuscript received June 25, 2012; accepted December 3, 2012. The authors thank the Swedish Research Council, The Knut and Alice Wallenberg Foundation, The Crafoordska Foundation, and The Royal Physiographic Society in Lund for financial support.

M. Evertsson, M. Cinthio, H. W. Persson, and T. Jansson are with the Department of Electrical Measurements, Faculty of Engineering, Lund University, Lund, Sweden (e-mail: maria.evertsson@elmat.lth.se).

S. Fredriksson and F. Olsson are with Genovis AB, Lund, Sweden.
DOI <http://dx.doi.org/10.1109/TUFFC.2013.2591>

Other techniques, e.g., positron emission tomography (PET), single-photon emission computed tomography (SPECT), magnetic resonance imaging (MRI), and optical methods, receive the most attention for molecular imaging. The same development for ultrasound has been slower, primarily because conventional ultrasound contrast agents, which are composed of relatively large micrometer-scale bubbles, are confined to the vascular system [3]. These relatively large bubbles are also difficult to attach to a target, because the shear force from the blood tends to drag the bubble away. New types of contrast agents show promise in increasing the possible molecular imaging applications for ultrasound. Perfluorocarbon emulsions have been suggested because they form bubbles with diameters in the order of 100 nm [4]; however, these bubbles produce a weaker echo than gaseous microbubbles because of their small size. Photoacoustic imaging [5] is a relatively new modality that can open up molecular imaging applications using, for instance, gold nanoparticles [6], quantum dots [7], and carbon nanotubes [8].

Superparamagnetic iron oxide (SPIO) nanoparticles were approved as contrast agents for MRI more than a decade ago. Recently, it has been shown that it is possible to detect SPIO nanoparticles with MRI, SPECT, and optical techniques in the same animal [9]. The combination of the best properties of these imaging techniques with molecular imaging would vastly increase the potential of imaging for detection of diseases and improved patient care. For instance, the combination of sensitive and quantitative SPECT data with high-resolution MRI could improve the staging of breast cancer patients [10], and the very same particles can later be imaged by more portable methods to provide guidance during surgery [9]. However, new imaging strategies are needed for ultrasound, because the particles used are too small to be imaged directly with conventional ultrasound equipment.

In 2006, Oh *et al.* [11] demonstrated a new technique, called magnetomotive ultrasound (MMUS) imaging, that enabled detection of SPIO nanoparticles with ultrasound. This imaging technique is built on the same key principle as magnetomotive optical coherence tomography (MMOCT), first demonstrated in 2005 [12]. The main idea is the application of a time-varying magnetic field (pulsed or sinusoidal) to the volume in which the nanoparticles are deposited. The magnetic field induces movement

of the particles and, thereby, the surrounding tissue. This movement can be detected with traditional Doppler techniques [11], M-mode techniques [13], or correlation techniques [14]. Indeed, standard Doppler techniques (i.e., implemented in the ultrasound scanner and not requiring offline analysis) have proved sufficient to image particles phagocytosed by Kupffer cells in a mouse liver [11].

Because MMOCT is restricted to only 1- or 2-mm penetration depth in scattering tissue [15], MMUS would vastly increase the number of applications for imaging of SPIO nanoparticles both for preclinical and clinical use because of its much larger imaging depth. A fast-growing segment is high-frequency ultrasound imaging of small animals for preclinical studies, which is also likely to be the first practical application of MMUS. Therefore, we have chosen to evaluate MMUS for high frequencies, which has the added benefit that a given magnetomotive displacement produces a larger relative phase shift, and thus a higher sensitivity to smaller displacements.

Using a high-frequency linear-array system, we have identified two complications that would restrict the use of magnetomotive imaging of SPIO nanoparticles for pre-clinical and clinical practice: first, because the induced displacement magnitude is in the order of micrometers, there is an inherent sensitivity to motion artifacts, and second, we discovered an induced displacement occurring outside the nanoparticle-laden regions. However, we have also found in our setup that these induced displacements have opposite phase relative to those within the nanoparticle laden regions, a finding that can be used to suppress undesirable motion artifacts.

To distinguish between regions containing nanoparticles and regions that do not, we developed an algorithm based on quadrature detection and phase gating precisely at the frequency with which the nanoparticles are moving. Thus, clutter occurring at other frequencies can be filtered out, and as an additional benefit, also displacements occurring out of phase relative to the displacements in the nanoparticle-laden regions, such as those described in the preceding paragraph. Our goal was to investigate the ability of our algorithm to enhance regions that contain SPIO nanoparticles relative to regions without these particles; this is a crucial property for *in vivo* measurements. Further, we investigated how different frequencies and magnitudes of the magnetic field, as well as different nanoparticle concentrations, affect the detection.

II. MATERIALS AND METHODS

A. Nanoparticles

The nanoparticles (Genovis AB, Lund, Sweden) consisted of solid iron oxide cores of Fe_3O_4 (magnetite), which were coated with polyethylene glycol (PEG; molecular weight 2000 to 4000 g/mol) to stabilize the suspension. Using transmission electron microscopy, the diameter of the particles was measured to be 18 ± 2 nm. The hydro-

dynamic particle diameter measured with dynamic light scattering was 30 nm on average, including the coating (the larger diameter using dynamic light scattering is due to water molecules coordinating around the particle). The nanoparticles had a magnetic saturation of approximately 80 emu/g of Fe_3O_4 .

B. Phantom Mold

A rectangular poly(methyl methacrylate) (PMMA) container was produced as a mold for the phantom. Three sides of the container were detachable. They were held in place by brass screws, which did not interfere with the magnetic field. Three PMMA cylinders (5 mm diameter) were attached to the bottom of the container. These cylinders created holes in the phantom, within which polyvinyl alcohol (PVA) inserts containing different concentrations of nanoparticles were placed and imaged during the experiments.

C. PVA Phantom

The phantoms were made of 5% PVA (wt%), to act as a tissue-mimicking material. The crystallized PVA (average M_w 85 000 to 124 000, 98% to 99% hydrolyzed, Sigma-Aldrich Co. LLC, St. Louis, MO) was dissolved in Milli-Q water (EMD Millipore Corp., Billerica, MA) in an autoclavable glass bottle sealed with a polypropylene plug. To do this, the glass bottle and its contents were put in a Nüve FN300 oven (Nüve, Ankara, Turkey) at 95°C for 2 h. When the PVA was completely dissolved, 30 mg of graphite (Graphite, Merck KGaA, Darmstadt, Germany) per milliliter of solution was added to act as the scattering media in the ultrasound image. The PVA solution was poured into the phantom mold described previously. It was also poured into three Eppendorf tubes containing SPIO nanoparticles in the concentrations needed to form solutions of 0.6, 0.45, and 0.3 mg of iron oxide/mL. The solutions in the Eppendorf tubes were mixed and then drawn into three syringes having an internal diameter matching the holes in the phantom. To crosslink the mixture, the phantom mold and the syringes underwent two freeze-thaw cycles. When the PVA was crosslinked, the contents of the syringes were placed into the phantom mold.

A second phantom containing only the background material was manufactured to investigate whether there was any displacement effect when no SPIO nanoparticles were present. Because PVA, together with most biological tissues, is weakly diamagnetic, it will be repelled by a magnetic field, whereas the opposite is true for a paramagnetic material [16]. Oldenburg *et al.* [17] suggested that a critical concentration of SPIO nanoparticles existed at which the force from the nanoparticles balanced the opposing force from the tissue. In other words, at larger concentrations, the net response from the tissue volume will appear paramagnetic, and for lower concentrations diamagnetic. To extract the paramagnetic signal, they introduced a

phase filter, because in an alternating magnetic field, the para- and diamagnetic movements have opposite phase. Our objective, using the phantom free from nanoparticles, was to establish whether the diamagnetic effect was so large in our phantom material as to cause the out-of-phase movement we detected.

The elastic modulus of the phantom material was measured using the technique presented by Chen *et al.* [18], in which the relative material compression (strain) was measured simultaneously with the applied force over the sample area (stress).

D. Experimental Setup

All investigations were performed with a high-frequency ultrasound scanner, VisualSonics Vevo 2100 (VisualSonics Inc., Toronto, ON, Canada). The setup is shown in Fig. 1. The phantom was positioned over a cone-shaped iron core surrounded by a solenoid (Ledex 6EC, Saia-Burgess Inc., Deerfield, IL), which induced a magnetic field when a current was applied. The electric signal to control the magnetic field strength was produced by a function generator (HP 33120, Agilent Technologies Inc., Santa Clara, CA), and amplified by a power amplifier (in-house design, 3-dB bandwidth 6 to 20000 Hz). The signal to the solenoid was monitored with an oscilloscope (Tektronix TDS 360, Tektronix Inc., Beaverton, OR) and the voltage amplitude was adjusted to be constant over the investigated frequency range. The maximum magnetic flux density in our experiments, 0.18 T, occurred at a solenoid excitation of 4 Hz, 30 V, measured just above the iron-core tip using a gaussmeter (model 9200, F. W. Bell, Milwaukee, OR; transversal probe, type HTB92-0608).

The transducer, MS250 (13 to 24 MHz bandwidth, center frequency 21 MHz; VisualSonics Inc., Toronto, ON,

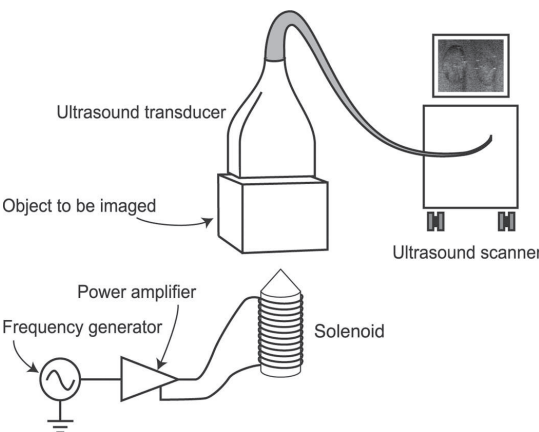


Fig. 1. Schematic diagram of the experimental setup. In reality, the solenoid is contained in a cylindrical housing and the iron core is machine-turned to fit inside the solenoid.

Canada), was positioned on the surface of the PVA phantom, using ultrasound gel to provide acoustic contact. A sinusoidal voltage, with frequencies 4, 8, 12, and 16 Hz and magnitudes 10, 20, and 30 V_{pp}, was applied to the solenoid.

The ultrasound RF in-phase and quadrature (IQ) data forming the displayed B-mode images was collected using the Vevo 2100 research interface. The data was exported to Matlab (The MathWorks Inc., Natick, MA), where the algorithm was implemented. Two cineloops of two different cross sections were acquired for every frequency at every voltage in the nanoparticle-laden phantom to appreciate the homogeneity in the phantom. The RF capture frame rate was 100 frames/s, the imaging depth was 11.0 mm, the line density was 256 lines/frame and the number of samples per line was 304.

E. Frequency-Tracking and Phase-Sensitivity Algorithm

The nanoparticle displacement was tracked at each spatial position in the two-dimensional IQ-data cineloop. The magnetic nanoparticles oscillate with a frequency (f_0), twice the frequency of the voltage applied on the solenoid [11]. The same frequency, f_0 , but with opposite phase, is expected in the phantom without nanoparticles if a diamagnetic response from the phantom material is present [17].

Let $r_I(x, y, m) + j r_Q(x, y, m)$ ($m = 1, 2, \dots, M$) denote the IQ-data from a cineloop of M frames, as exported from the Vevo 2100 research interface. Here, r_I denotes the real part and r_Q the imaginary part, and the position in the image plane is given by the coordinates x (lateral direction) and y (axial direction).

The phase $r(x, y, m)$ for each spatial position throughout all frames was extracted from the argument of the received IQ-data, $r(x, y, m) = \arg(r_I(x, y, m) + j r_Q(x, y, m))$. After unwrapping, the phase was quadrature detected with f_0 :

$$R(x, y, m) = r(x, y, m) \times e^{j2\pi f_0 m \Delta t} = I(x, y, m) + j Q(x, y, m), \quad (1)$$

where Δt corresponds to the time interval between two frames. (Note that I and Q , as denoted here, are different from what is considered IQ-data in the RF-data acquisition.) To obtain the displacement magnitude at the frequency f_0 for each pixel, a mean value of the quadrature detected sequence $R(x, y, m)$ was calculated. The mean value was used instead of a low-pass filter because we were interested in detecting the displacement magnitude at f_0 only:

$$\overline{R(x, y)} = \overline{I(x, y)} + j \overline{Q(x, y)}. \quad (2)$$

The displacement magnitude, $A(x, y)$, was then obtained as

$$A(x, y) = 2|\overline{R(x, y)}| = 2\sqrt{\overline{I(x, y)}^2 + \overline{Q(x, y)}^2}. \quad (3)$$

To compare $A(x, y)$ (i.e., at f_0 only) with the total motion (i.e., displacement at all frequencies) in the phantom, the rms deviation of the phase $r(x, y, m)$ was calculated, hereafter denoted r_{RMS} . To make the numbers comparable, the displacement magnitude A was divided by a factor of $\sqrt{2}$ (denoted A_{RMS}).

Finally, the phase P in each pixel at frequency f_0 was calculated as

$$P(x, y) = \arg\left(\frac{Q(x, y)}{I(x, y)}\right). \quad (4)$$

F. Evaluation

The detected displacement magnitude, phase distribution, and signal-to-clutter ratio (SCR) were calculated to evaluate the algorithm.

Both r_{RMS} and A_{RMS} were determined at four different regions; within the three nanoparticle-laden inserts and between the 0.6-mg $\text{Fe}_3\text{O}_4/\text{mL}$ and 0.45-mg $\text{Fe}_3\text{O}_4/\text{mL}$ inserts. All regions had areas of 9×9 pixels, which corresponded to 0.33 mm axially and 0.81 mm laterally. The mean values and standard deviations within these regions were calculated. The resulting measure (in radians) was then translated into micrometers, color-coded, and superimposed on the B-mode image. Two images were created; one in which all pixels representing displacement with frequency f_0 were color coded, and a second in which only a phase interval of 2.3 rad, including all nanoparticle displacement, was color coded. Other pixel values were set to zero and plotted with B-mode grayscale information. Two additional images were created as a comparison; the total motion in the phantom, r_{RMS} , was color coded and superimposed on the B-mode image as well as the phase information P for each spatial position.

The phase interval was chosen based on the time necessary to acquire one frame. Because this was 10 ms (frame rate 100 Hz), it resulted in a time delay that caused the detected phase of the particle displacement to differ between the acquisitions of the first and last lines of the image frame. In other words, the phase interval that needed to be covered corresponded to f_0 divided by the frame rate, multiplied by 2π to obtain the result in radians. This meant that the maximum phase interval to be covered was 2.1 rad (in the 16-Hz case), and the gate was chosen to slightly exceed this.

The SCR was calculated by dividing the average r_{RMS} (or A_{RMS}) value within the 9×9 pixel region from the 0.6-mg $\text{Fe}_3\text{O}_4/\text{mL}$ insert, by the value from the 9×9 pixel region between the nanoparticle-laden regions. The ratios were then converted to decibels. The differences between the phase and frequency sensitive images and the image of the total movement were taken as measures of improvement resulting from the algorithm.

To investigate the displacements caused by diamagnetic forces, a measurement was made on the phantom without nanoparticles. $I(x, y)$ and $Q(x, y)$ were recorded in a 9×9 pixel region using magnetic solenoid excitation voltage

of 30 V at 4 Hz, and the 81 value pairs were plotted in a IQ-coordinate grid. As a comparison IQ-data pairs from 9×9 pixel regions from the 0.6-mg $\text{Fe}_3\text{O}_4/\text{mL}$ insert and from between the nanoparticle-laden regions, respectively, were plotted in the same fashion (from the 4 Hz, 30 V measurement #1).

III. RESULTS

Fig. 2 shows a B-mode image of our phantom, in which the nanoparticle-laden regions are outlined and labeled. During our experiments, motion over the entire detected frequency range 0 to 50 Hz (half the frame rate) was present in all parts of the phantom. This is shown in Fig. 3(a), where r_{RMS} is color coded for the 4 Hz 30 V_{pp} measurement. By employing quadrature detection at the nanoparticle displacement frequency, motion at other frequencies is suppressed. At this frequency, motion is more apparent both in, and between, the nanoparticle-laden regions [Fig. 3(b)]. However, by examining the phase at the nanoparticle displacement frequency it is shown that nanoparticle-laden regions are moving virtually with the same phase, whereas the regions between the nanoparticle-laden regions move with opposite phase. This is shown in Fig. 3(c) with a color-encoded representation of the relative phase of the displacement. The slight variation in detected phase between the left and the right part of the phantom is due to the scanning velocity as described in Section II. The effect of applying our frequency-tracked and phase-discriminative algorithm is shown in Fig. 3(d). The SCR improvements for this measurement are 1.1 dB for the low-concentration insert and 8.0 dB for the high-concentration insert between Figs. 3(a) and 3(b), and additional improvements of 22.0 and 22.0 dB between Figs. 3(b) and 3(d). The large SCR improvements mainly result from all pixels outside the permitted phase range being set to zero. The areas immediately above and below the nanoparticle-laden regions moved in-phase with the particles [Fig. 3(c)], thus making the nanoparticle-laden regions appear to be artificially elongated in the vertical direction [Fig. 3(d)].

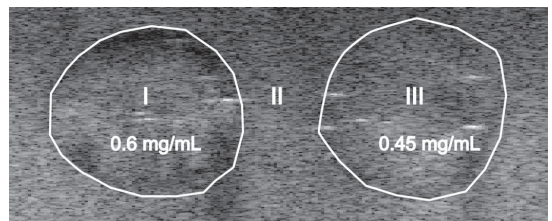


Fig. 2. A B-mode image of the phantom in which two nanoparticle-laden inserts are outlined and their concentrations noted. The lowest concentration insert (0.3-mg $\text{Fe}_3\text{O}_4/\text{mL}$) is not shown because there was no detectable displacement in the same phase range as the high-concentration nanoparticle-laden inserts. The two nanoparticle-laden regions are labeled, I (0.60-mg $\text{Fe}_3\text{O}_4/\text{mL}$) and III (0.45-mg $\text{Fe}_3\text{O}_4/\text{mL}$), and the region between them without nanoparticles is labeled II.

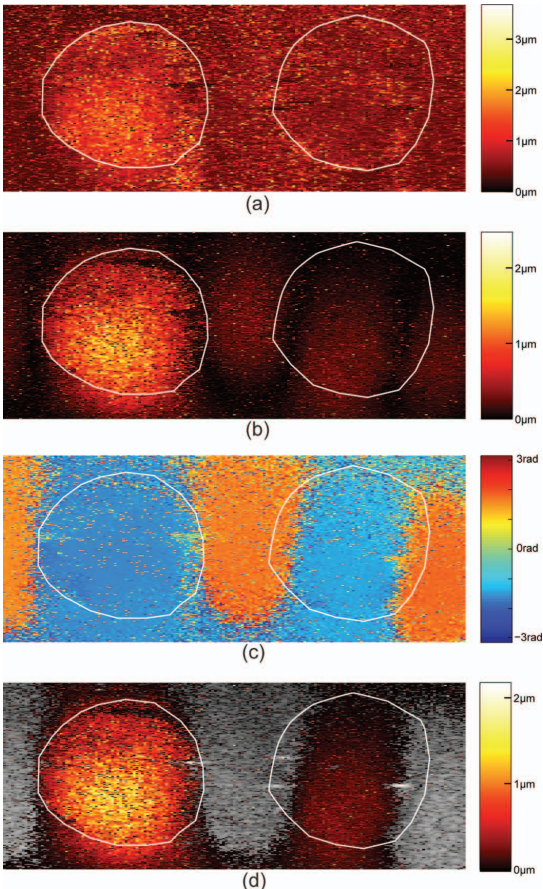


Fig. 3. Color-coded images showing displacement magnitude and its phase across the image in Fig. 2, obtained at 4 Hz, 30 V_{pp} magnetic solenoid excitation voltage. The color of each pixel represents the displacement magnitude [Figs. 3(a), 3(b), and 3(d)] or phase [Fig. 3(c)] in that position and is coded according to the color bar beside each individual image. Note the different scales. (a) Total movement, r_{RMS} , i.e., displacements at all frequencies are color-coded; (b) frequency-tracked but phase-insensitive imaging, i.e., movement at f_0 (in this case 8 Hz) is color coded; and (c) phase of the displacement across the B-mode image. Notice the approximate π rad phase difference between the displacements of the nanoparticle-laden inserts and the area between. A phase increase from left to right in the figure is appreciable. This is due to the scanning velocity, as described in the Section II. (d) Frequency-tracked and phase-discriminative imaging, i.e., displacement was only color coded when occurring with frequency f_0 and the phase difference was less than ± 1.15 rad relative to the center phase in the nanoparticle-laden regions.

Table I summarizes all the measurements in the nanoparticle-laden phantom. Higher nanoparticle concentration results in larger induced displacement magnitude (Fig. 4, showing the average of measurements from two cross sections). There were only a few pixels with detectable displacement in the same phase range as the high concentration nanoparticle-laden inserts for the 0.3-mg

Fe₃O₄/mL insert, even at the measurement creating the largest displacement, which is the case shown in the Fig. 4. The 0.3-mg Fe₃O₄/mL insert was therefore not included in the table.

The elastic modulus of the phantom material was measured to be 0.83 ± 0.13 kPa (mean \pm standard error), which is within the same range as reported elastic modulus values from the liver [18].

Throughout measurement series #1, an unwanted disturbance was present in the setup at approximately 24 Hz caused by mechanical vibrations from an unknown source. This disturbance was effectively suppressed in all measurements except in the 12 Hz case, where it coincided with the frequency of the nanoparticle displacement. The phase of the disturbance and that of the nanoparticle displacement were almost identical, which made it difficult to distinguish between noise and the signal of interest, especially for the measurement at the lowest excitation amplitude. In the second measurement series, the unwanted disturbance occurred at 27 Hz, but because this frequency did not coincide with any of the detection frequencies, this disturbance was successfully suppressed.

Overall, the displacement magnitude increased with higher nanoparticle concentrations and voltages. This is demonstrated in Fig. 5, which shows the resulting displacement magnitude in the three regions labeled I, II, and III (as denoted in Fig. 2), for different excitation frequencies and voltages. It can also be seen that the displacement magnitude in the region between the nanoparticle-laden inserts (region II), is in the same range as for the 0.45-mg Fe₃O₄/mL insert (region III). The displacement magnitude for the 0.6-mg Fe₃O₄/mL nanoparticle-laden insert (region I) is approximately five times larger than the 0.45-mg Fe₃O₄/mL insert. There seems to be a difference in displacement magnitudes between the different cross sections in some of the cases.

Fig. 5 also illustrates a tendency for decreasing displacement magnitude with increasing frequency.

Using our quadrature and phase gating algorithm, we are able to detect a nanoparticle displacement magnitude which is substantially smaller than the overall phantom motion. This is demonstrated in Fig. 6, where r_{RMS} (displacements at all frequencies) and A_{RMS} (displacements at f_0 only) are displayed for three different excitation voltages for the 0.45-mg Fe₃O₄/mL insert.

There appears to be no detectable diamagnetically induced displacement because measured values from the phantom without nanoparticles have a random phase and negligible magnitude, whereas values from regions within (region I) and between (region II) nanoparticle-laden inserts have a considerably higher magnitude with a preferred phase. This is shown in Fig. 7, where each measurement value ($I(x, y)$, $Q(x, y)$) from 9 by 9 pixel subareas are visualized in IQ-coordinate grids for three cases: Fig. 7(a) is within the 0.60-mg Fe₃O₄/mL insert (region I), Fig. 7(b) is between the high-concentration nanoparticle-laden inserts (region II), and Fig. 7(c) is in the center of the phantom without nanoparticles. All cineloops were

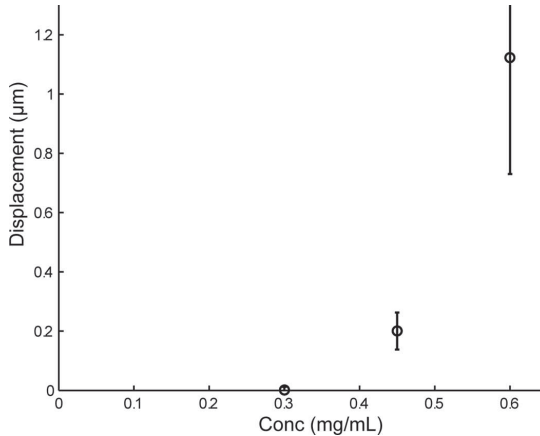


Fig. 4. The mean of measurements from the two cross sections (each point represents the average displacement magnitude in a 9×9 pixel subarea) for frequency-detected and phase-gated displacement at the three concentrations of nanoparticles (0.30, 0.45, and 0.6 mg $\text{Fe}_3\text{O}_4/\text{mL}$). The data are obtained at 4 Hz, 30 V_{pp} magnetic solenoid excitation voltage and the mean standard deviation of the two measurements is marked with error bars.

obtained at 4 Hz, 30 V_{pp}. Note the π rad phase shift between Figs. 7(a) and 7(b), including the small deviation resulting from the scanning velocity as described in Section II-F.

IV. DISCUSSION

We have proposed an algorithm that is able to calculate the displacement at the precise frequency of interest during magnetomotive ultrasound detection of SPIO nanoparticles, and suppress motion artifacts occurring at other frequencies. By applying this algorithm to data acquired with a high-frequency linear-array scanner, we have also shown that displacement is not only induced in the nanoparticle-laden regions but also indirectly outside those areas [see Fig. 3(b)]. By phase gating the detected frequency, the algorithm can also distinguish between these types of movement [Fig. 3(d)].

Previous studies using magnetomotive ultrasound on nanoparticle-laden phantoms [11], [13], [14] have neither included reports on indirectly induced displacement, nor on the influence of other motion artifacts. In our setup, we

TABLE I. SUMMARY OF THE SIGNAL-TO-CLUTTER RATIO (SCR) AND DISPLACEMENT MAGNITUDES FOR ALL MEASUREMENTS IN THE NANOPARTICLE-LADEN PHANTOM USING THE MS250 TRANSDUCER.

Measurement	SCR-0.6 mg $\text{Fe}_3\text{O}_4/\text{mL}$ insert Total displacement magnitude to frequency detected displacement magnitude (dB)	SCR-0.6 mg $\text{Fe}_3\text{O}_4/\text{mL}$ insert Frequency detected to phase discriminative displacement magnitude (dB)	Displacement magnitude (A_{RMS}) 0.45-mg $\text{Fe}_3\text{O}_4/\text{mL}$ insert (μm) \pm Std	Displacement magnitude (A_{RMS}) between inserts (μm) \pm Std	Displacement magnitude (A_{RMS}) 0.6-mg $\text{Fe}_3\text{O}_4/\text{mL}$ insert (μm) \pm Std
4 Hz 10 V 1	13	31	0.05 ± 0.09	0.04 ± 0.03	0.17 ± 0.07
4 Hz 10 V 2	6	∞	0.05 ± 0.02	0.09 ± 0.04	0.30 ± 0.11
4 Hz 20 V 1	9	37	0.11 ± 0.04	0.17 ± 0.15	0.67 ± 0.34
4 Hz 20 V 2	3	∞	0.13 ± 0.04	0.23 ± 0.07	0.82 ± 0.30
4 Hz 30 V 1	8	22	0.22 ± 0.06	0.28 ± 0.12	1.27 ± 0.39
4 Hz 30 V 2	2	∞	0.19 ± 0.06	0.29 ± 0.10	0.98 ± 0.40
8 Hz 10 V 1	10	14	0.03 ± 0.01	0.05 ± 0.05	0.17 ± 0.07
8 Hz 10 V 2	7	30	0.04 ± 0.03	0.08 ± 0.05	0.25 ± 0.09
8 Hz 20 V 1	8	20	0.09 ± 0.03	0.14 ± 0.10	0.58 ± 0.37
8 Hz 20 V 2	5	∞	0.12 ± 0.05	0.22 ± 0.08	0.76 ± 0.34
8 Hz 30 V 1	6	39	0.17 ± 0.11	0.20 ± 0.07	0.79 ± 0.42
8 Hz 30 V 2	2	∞	0.19 ± 0.07	0.31 ± 0.10	1.14 ± 0.64
12 Hz 10 V 1*	—	—	—	0.17 ± 0.07	0.15 ± 0.08
12 Hz 10 V 2	5	31	0.04 ± 0.04	0.05 ± 0.03	0.21 ± 0.11
12 Hz 20 V 1	19	10	0.18 ± 0.05	0.04 ± 0.06	0.61 ± 0.28
12 Hz 20 V 2	2	40	0.08 ± 0.04	0.13 ± 0.04	0.55 ± 0.28
12 Hz 30 V 1	3	38	0.14 ± 0.05	0.28 ± 0.10	0.69 ± 0.53
12 Hz 30 V 2	3	∞	0.16 ± 0.09	0.26 ± 0.11	0.94 ± 0.35
16 Hz 10 V 1	7	20	0.03 ± 0.02	0.03 ± 0.02	0.10 ± 0.04
16 Hz 10 V 2	1	29	0.04 ± 0.08	0.04 ± 0.02	0.13 ± 0.09
16 Hz 20 V 1	6	28	0.05 ± 0.05	0.06 ± 0.03	0.19 ± 0.08
16 Hz 20 V 2	3	40	0.05 ± 0.03	0.11 ± 0.04	0.40 ± 0.18
16 Hz 30 V 1	6	40	0.06 ± 0.02	0.09 ± 0.05	0.34 ± 0.13
16 Hz 30 V 2	-3	∞	0.09 ± 0.04	0.15 ± 0.05	0.63 ± 0.41

Two sets of measurements were obtained for each frequency and voltage. Note that the infinite SCR values are due to all pixels in the region between the nanoparticle-laden regions representing movement with opposite phase, and are therefore set to zero.

*In the 12 Hz 10 V 1 measurement, it was difficult to distinguish between noise and signal because of a 24-Hz disturbance coinciding with the nanoparticle displacement.

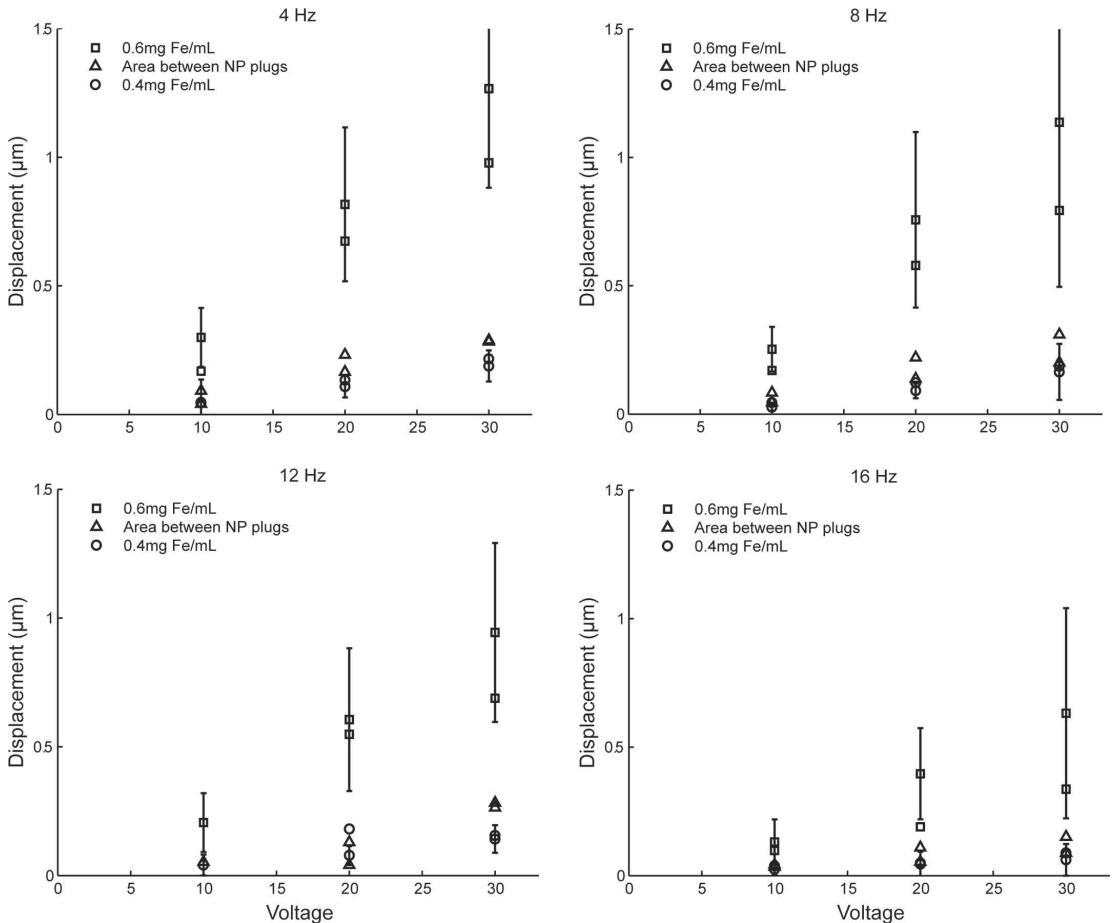


Fig. 5. The frequency detected displacement magnitude (A_{RMS}) in the nanoparticle-laden regions (region I and III in Fig. 2) and in the area between the nanoparticle regions (region II in Fig. 2), using the MS250 (10 to 25 MHz) transducer as a function of applied voltage to the solenoid. Each point represents the average displacement magnitude in a subarea (9 × 9 pixels). The standard deviation is marked with error bars on the highest and lowest measured value for each voltage. There are two measured values at each concentration of nanoparticles, representing measurements at two different cross sections in the phantom.

found that the displacement magnitude in media between two nanoparticle-laden inserts was in the same range as the displacement magnitude for the 0.45-mg $\text{Fe}_3\text{O}_4/\text{mL}$ insert. However, there was a π rad phase shift between the nanoparticle-laden regions and the area between these regions when a sinusoidal voltage was applied on the solenoid [see Fig. 3(c)]. Oldenburg *et al.* [17] have explained the presence of opposite phase displacements in MMOCT studies as a consequence of the diamagnetic response from diamagnetic media relative to paramagnetic nanoparticle-laden regions. However, we did not find any detectable diamagnetic induced displacement in our phantom with no SPIO nanoparticles present. All measured displacement magnitudes were evenly distributed in the IQ-coordinate grid [i.e., with no preferred phase, Fig. 7(c)] indicating

that diamagnetic displacement was hidden in the noise-floor and cannot be detected. Instead, we hypothesize that the containment of our phantom in a mold might explain the large magnitude of the opposite phase displacement, because the walls act as rigid boundaries. Because of conservation of mass, an induced upward displacement of nanoparticle-laden phantom material must be counteracted by a downward displacement of phantom material unaffected by the magnetic field. An indication that the hypothesis is correct can be seen in Fig. 3(d), which shows that magnetomotive displacement is transmitted into the background material, i.e., there is a vertical displacement above and below the inserts. The magnetomotive signal is affected by the presence of a boundary, as we showed in a recent publication [19]. Another explanation to the out-of-

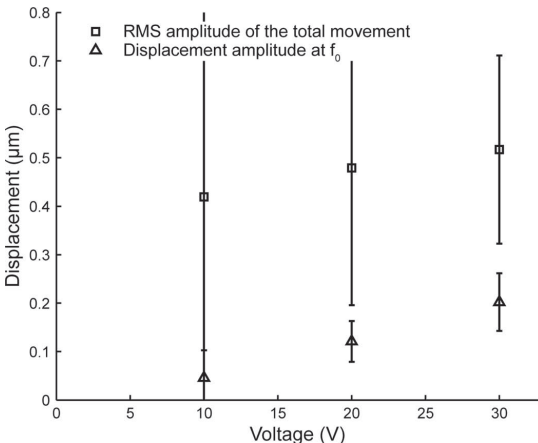


Fig. 6. The mean of measurements from the two cross sections (9×9 measured displacement magnitude values each) for the total movement, r_{RMS} (open squares), and frequency detected displacement magnitude A_{RMS} (open triangles), respectively, in the 0.45-mg Fe₃O₄/mL concentration insert at the three different voltages. The magnetic field excitation frequency was 4 Hz.

phase movement might be shear wave generation. For an unbounded medium, nanoparticle displacement will presumably induce a shear movement in the same manner as was reported for acoustic radiation force imaging (ARFI) [20]. Interestingly, the displacement magnitudes reported from ARFI measurements are very similar to those reported in our study. The process of shear wave generation is, however, unclear in our case, foremost because of the lack of connection (glue or chemical bonding) between the background material and the inserts, but it is also unclear if the generated wavelength is short enough to need to be considered in our setup. Whether the out-of-phase displacement is noticeable *in vivo* is still an open question, but it is likely that the phase carries important information here also, because the elastic properties of tissue are similar to our phantom and because tissue interfaces can act as semi-rigid boundaries (bone, fat, etc.).

The demonstrated reduction of undesired displacements is a crucial step enabling the application of magnetomotive imaging of nanoparticles in preclinical and clinical investigations. The median SCR improvement using phase-gated and frequency-detected displacement magnitude compared with total movement (r_{RMS}) of all measurements was found to be approximately 36 dB. Note that some SCR values are set to infinity when all pixels from region II in the phase gated image have been set to zero, because all of these pixels move out of phase compared with the nanoparticle-laden regions. This can also explain the large variability in the SCR values.

The nanoparticle displacement decreased when the frequency of the magnetic field increased. One explanation might be that the energy of the wave motion is proportional to both the displacement magnitude and frequency

squared. Because the applied energy was kept constant, the displacement magnitude must decrease with frequency. Other explanations include frequency-dependent losses in the amplifier, the solenoid, and the iron core. However, all frequencies were detectable, thereby providing sufficient opportunity to change the excitation frequency in case of an interfering disturbance. For example, in the first measurement series, interference at approximately 24 Hz was observed (which most likely corresponds to the eigenfrequency of the measurement setup, i.e., all components involved in holding the phantom, transducer, etc.). This made the detection difficult when the excitation frequency was 12 Hz, but did not impede detection at other frequencies. A difference in displacement magnitude can be seen by comparing two different cross-sections in the nanoparticle-laden phantom. This difference is probably due to a non-uniform distribution of SPIO-nanoparticles.

As shown previously by Mehrmohammadi *et al.* [14], a higher voltage or nanoparticle concentration results in a larger induced displacement magnitude. This result was confirmed in our study. Mehrmohammadi *et al.* [13], [14] and Oh *et al.* [11] used a conventional scanner or a single-element transducer, and we have now demonstrated similar results with a high-frequency linear-array transducer for preclinical imaging.

It is noteworthy that displacement magnitudes well below the noise floor can be detected. The background noise level was found to be around $0.5 \mu\text{m}$, and this is the detection limit if the total movement r_{RMS} is taken as a measure of displacement (Fig. 6). When the magnetically-induced nanoparticle displacement magnitude is under the limit, the phase-tracking algorithm can still detect displacements having the right frequency and phase. It even shows that the detected displacement magnitude increases linearly with applied excitation voltage (Fig. 5).

Mehrmohammadi *et al.* demonstrated a considerably larger displacement in their nanoparticle-laden phantoms [14] than we were able to show. One explanation might be that their phantom was free floating in a water tank, whereas our phantom was contained in a mold with rigid walls. Other explanations could be differences between the nanoparticles employed in the respective studies, or differences in elastic or viscous properties of the phantom material. The measured magnetic field strength was substantially lower in our case as compared with the values reported in Oh *et al.* [11] and Mehrmohammadi *et al.* [13], [14]. However, the magnetic gaussmeter probe averaged the measurement over a comparably large area (1.75 by 1.75 mm), and the reported value is likely far from the maximum field strength, because the tip of the iron core produces a strong gradient. Details of the field measurement in the studies of Oh and Mehrmohammadi are missing, but given the measurement situation with a strongly in-homogeneous field, it is not unlikely that a smaller active magnetic probe area will produce a higher value. Because our field generator is equivalent to theirs, we find it likely that the field strength differences between our setups are less than our measurement indicates.

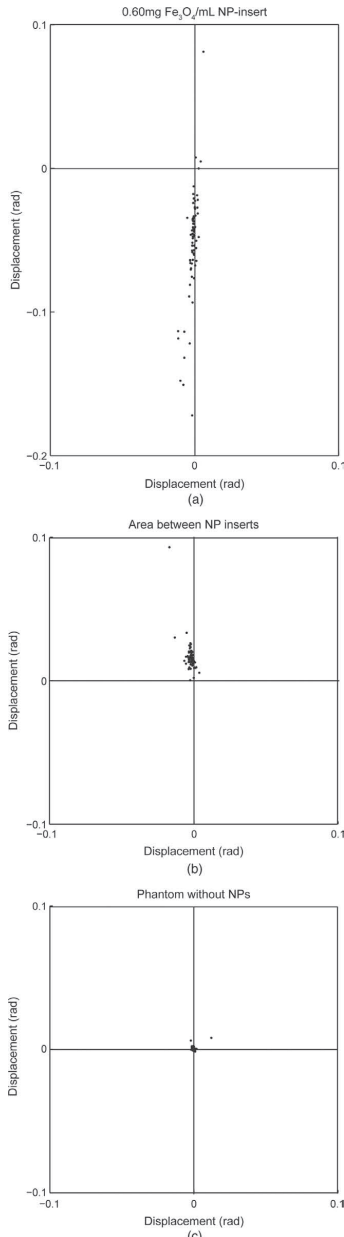


Fig. 7. The figure displays measurement values ($I(x, y)$ $Q(x, y)$) from 9 \times 9 pixel subareas from three cases: (a) region I in Fig. 2 (0.60-mg Fe_3O_4 /mL insert); (b) region II in Fig. 2 (the area between the high-concentration nanoparticle-laden inserts); and (c) the center of the phantom without nanoparticles. Each panel displays the 81 $I(x, y)$ $Q(x, y)$ pairs in an IQ-coordinate grid, where the displacement magnitude can be interpreted as the distance from each data point to the origin, and its phase, P , as the angle to the abscissa. Note that the scale on the axes is given in radians, where 2π radians correspond to one wavelength at the center frequency of the imaging transducer. All measurements were obtained at 4 Hz, 30 V_{pp} magnetic solenoid excitation voltage.

The displacement with opposite phase as noticed by us is likely to be smaller in a free-floating phantom or in a large object, even though it is presumably a noticeable effect as particles are attracted to the point where the field emanates (i.e., not along parallel lines). On the other hand, induced shear waves resulting from nanoparticle displacement may also be present. In any case, the algorithm will suppress displacement artifacts at other frequencies, and will also suppress displacement tendencies that are at the desired frequency but have a phase that is outside a given interval. However, the parts of the potential shear wave (or other wave type) that have a phase not within the phase interval we choose to suppress will be displayed as a magnetomotive signal.

A difficulty with our setup was that we could not attach the phantom to the ultrasound transducer; instead, the phantom was partially supported by the cone-shaped iron core. This meant that the whole phantom and the mold might move with the same frequency and phase as the iron core, which would have presented as a problem had we not taken advantage of the phase detection algorithm. Because the displacement created from the magnetic field is apparently larger than that of the core, the algorithm can distinguish the nanoparticle displacement.

The present study confirms the threshold effect observed by Mehrmohammadi *et al.* [14]. The high-concentration nanoparticle-laden insert (0.6-mg Fe_3O_4 /mL) moved around five times more than the 0.45-mg Fe_3O_4 /mL concentration insert and no displacement at all was detected in the 0.3-mg Fe_3O_4 /mL insert (see Fig. 4). Oldenburg *et al.* [17] argued that diamagnetism could cause a threshold effect. However, as shown in Fig. 7(c), no diamagnetic effect could be measured in our setup. Another explanation might be that an internal resistance resulting from the viscoelastic properties of the phantom material must be overcome before the particles in the phantom can start to move. It appears from Figs. 5 and 6 that the displacement magnitude increases with voltage but that the increase does not start at 0 V. Extrapolation shows that a voltage between 2 and 5 V is needed to initiate displacement, further pointing in the direction of an effect similar to an internal resistance being the cause. This may, in turn, be dependent on material parameters as well as phantom design.

Another factor that may influence the nonproportional relationship between concentration and displacement is the inhomogeneous magnetic field distribution in the image plane. As a consequence, the magnetomotive force will vary over the imaged cross section. Thus, the absence of displacement in the lowest concentration insert may also be due to it being farthest from the magnet or the threshold effect noted previously. Evaluation of this is not within the scope of this study. Finally, a difference in mechanical coupling between the inserts and the background material cannot be ruled out, even though the B-mode image in Fig. 2 shows a minimal mismatch in mechanical properties at the boundary because of the absence of an echo and shadow.

A limitation of this method is the possible generation of heat by the particles as they are exposed to a magnetic field [21]. Heat generation may damage the surrounding tissue in *in vivo* measurements; thus, further investigation into heat generation for varying exposure times is necessary before *in vivo* use. On the other hand, localized heating of tumor tissue using targeted nanoparticles may present a possible advantage, by combining diagnosis and therapy [22]. Another problem that may occur when using this technique is insufficient displacement of particles within tissue resulting from inadequate concentration and/or magnetic field strength as demonstrated in the 0.3-mg Fe₃O₄/mL insert. Improvements of the magnetic field strengths (e.g., changing solenoid) and of the nanoparticles (e.g., increasing the nanoparticles' susceptibility) must be considered.

V. CONCLUSION

To our knowledge, we have for the first time used a high-frequency ultrasound scanner to evaluate the displacement in a SPIO-nanoparticle-laden phantom, enabling higher measurement sensitivity. During magneto-motive detection, we have shown displacement artifacts that have not been previously reported. We have addressed this issue by developing an algorithm based on quadrature detection and phase gating at the frequency of interest. The demonstrated algorithm effectively enhances regions containing SPIO nanoparticles, a crucial property for *in vivo* measurements.

ACKNOWLEDGMENTS

The authors thank D. Ley and T. Poepping for their helpful comments on the manuscript.

REFERENCES

- [1] R. Weissleder, "Molecular imaging in cancer," *Science*, vol. 312, no. 5777, pp. 1168–1171, 2006.
- [2] S. A. Schmitz, M. Taupitz, S. Wagner, K.-J. Wolf, D. Beyersdorff, and B. Hamm, "Magnetic resonance imaging of atherosclerotic plaques using superparamagnetic iron oxide particles," *J. Magn. Reson. Imaging*, vol. 14, no. 4, pp. 355–361, 2001.
- [3] S. Menakuru, N. Brown, C. Staton, and M. Reed, "Angiogenesis in pre-malignant conditions," *Br. J. Cancer*, vol. 99, no. 12, pp. 1961–1966, 2008.
- [4] G. M. Lanza, D. R. Abendschein, and C. S. Hall, "In vivo molecular imaging of stretch-induced tissue factor in carotid arteries with ligand-targeted nanoparticles," *J. Am. Soc. Echocardiogr.*, vol. 13, no. 6, pp. 608–614, 2000.
- [5] L. V. Wang, *Photoacoustic Imaging and Spectroscopy*. Boca Raton, FL: CRC Press, 2009.
- [6] M. A. Eghatdari, J. A. Copland, V. L. Popov, N. A. Kotov, M. Motamedi, and A. A. Oraevsky, "Biocomjugated gold nanoparticles as a contrast agent for optoacoustic detection of small tumors," *Proc. SPIE*, vol. 4960, pp. 76–85, 2003.
- [7] E. V. Shashkov, M. Everts, E. I. Calanzha, and V. P. Zharov, "Quantum dots as multimodal photoacoustic and photothermal contrast agents," *Nano Lett.*, vol. 8, no. 11, pp. 3953–3958, 2008.
- [8] A. de la Zerda, C. Zavaleta, S. Keren, S. Vaithilingam, S. Bodapati, Z. Liu, J. Levi, T.-J. Ma, O. Oralkan, Z. Cheng, X. Chen, H. Dai, B. T. Khuri-Yakub, and S. S. Gambhir, "Photoacoustic molecular imaging in living mice utilizing targeted carbon nanotubes," *Nat. Nanotechnol.*, vol. 3, no. 9, pp. 557–562, 2008.
- [9] R. Madru, F. Olsson, K. Wingårdh, S. Fredriksson, C. Ingvar, E. Carleman, J. Olsrud, J. Lått, F. Ståhlberg, and S. E. Strand, "Preparation and characterization of 99mTc-labeled superparamagnetic iron oxide (IO) nanoparticles for multimodality imaging (MRI/SPECT) of SLN," in *Proc. Int. Society for Magnetic Resonance in Medicine and Biology Conf.*, 2009, p. 3695.
- [10] R. Madru, P. Kjellman, F. Olsson, K. Wingårdh, C. Ingvar, F. Ståhlberg, J. Olsrud, J. Lått, S. Fredriksson, L. Knutsson, and S. E. Strand, "99mTc-labeled superparamagnetic iron oxide nanoparticles for multimodality SPECT/MRI of sentinel lymph nodes," *J. Nucl. Med.*, vol. 53, no. 3, pp. 459–463, 2012.
- [11] J. Oh, M. D. Feldman, J. Kim, C. Condit, S. Y. Emelianov, and T. E. Milner, "Detection of magnetic nanoparticles in tissue using magneto-motive ultrasound," *Nanotechnology*, vol. 17, no. 16, pp. 4183–4190, 2006.
- [12] A. L. Oldenburg, J. R. Gunther, and S. A. Boppart, "Imaging magnetically labeled cells with magnetomotive optical coherence tomography," *Opt. Lett.*, vol. 30, no. 7, pp. 747–749, 2005.
- [13] M. Mehrmohammadi, J. Oh, L. Ma, E. Yantsen, T. Larson, S. Malildi, S. Park, K. P. Johnston, K. Sokolov, T. Milner, and S. Y. Emelianov, "Imaging of iron oxide nanoparticles using magneto-motive ultrasound," in *Proc. IEEE Ultrasonics Symp.*, 2007, pp. 652–655.
- [14] M. Mehrmohammadi, J. Oh, S. Aglyamov, A. Karpouki, and S. Y. Emelianov, "Pulsed magneto-acoustic imaging," in *Proc. 31st Annu. Int. IEEE Engineering in Medicine and Biology Society Conf.*, 2009, pp. 4771–4774.
- [15] J. M. Schmitt, "Optical coherence tomography (OCT): A review," *IEEE J. Sel. Topics Quantum Electron.*, vol. 5, no. 4, pp. 1205–1215, 1999.
- [16] J. F. Schenck, "Safety of strong, static magnetic fields," *J. Magn. Reson. Imaging*, vol. 12, no. 1, pp. 2–19, 2000.
- [17] A. L. Oldenburg, V. Crecea, S. A. Rinne, and S. A. Boppart, "Phase-resolved magnetomotive OCT for imaging nanomolar concentrations of magnetic nanoparticles in tissues," *Opt. Express*, vol. 16, no. 15, pp. 11525–11539, 2008.
- [18] E. J. Chen, J. Novakofski, W. K. Jenkins, and J. W. D. O'Brien, "Young's modulus measurements of soft tissues with application to elasticity imaging," *IEEE Trans. Ultrason. Ferroelectr. Freq. Control*, vol. 43, no. 1, pp. 191–194, 1996.
- [19] M. Evertsson, M. Cinthio, S. Fredriksson, F. Olsson, H. W. Persson, and T. Jansson, "Normalization of magnetic field effects: Towards quantitative magnetomotive ultrasound imaging," in *Proc. IEEE Ultrasonics Symp.*, 2011, pp. 775–778.
- [20] K. R. Nightingale, M. S. Soo, R. W. Nightingale, and G. E. Trahey, "Acoustic radiation force impulse imaging: In vivo demonstration of clinical feasibility," *Ultrasound Med. Biol.*, vol. 28, no. 2, pp. 227–235, 2002.
- [21] S. Wada, K. Tazawa, N. Suzuki, I. Furuta, and I. Nagano, "Pulp ablation therapy by inductive heating: Heat generation characteristics in the pulp cavity," *Oral Dis.*, vol. 13, pp. 193–197, 2007.
- [22] J. R. Oleson, S. K. Calderwood, C. T. Coughlin, M. W. Dewhurst, L. E. Gerweck, F. A. Gibbs, and D. S. Kapp, "Biological and clinical aspects of hyperthermia in cancer therapy," *Am. J. Clin. Oncol.*, vol. 11, pp. 368–380, 1988.



Maria Evertsson (formerly Holst) (M'10) was born in Malmö, Sweden, in 1984. She finished her M.Sc. degree in 2009. Since 2010, she has been a Ph.D. student in the Department of Electrical Measurement, Faculty of Engineering, Lund University, Sweden. Her research area is contrast agents, magnetomotive imaging, and signal processing.



Magnus Cinthio (formerly Persson) (M'01) was born in Klippan, Sweden, in 1969. He received the M.Sc. degree in biomedical engineering and the Ph.D. degree in electrical measurements in 1999 and 2004, respectively, from Lund University, Lund, Sweden. In 2010, he became an associate professor in the Faculty of Engineering, Lund University. He has been a visiting researcher at Tohoku University, Sendai, Japan, in 2007 and at Florence University, Florence, Italy, in 2012. Since 2005, he has held different positions in the Department of Electrical Measurements, Faculty of Engineering, Lund University. His research interests include ultrasonic tissue motion measurements, signal processing, and magneto-motive imaging, as well as arterial, cerebral, and musculature characterization.



Sarah Fredriksson was born in Svanshall, Sweden, in 1968. She finished her M.Sc. degree in biotechnology engineering at Lund University and received her Ph.D. degree, submitting a thesis with the title "Gene Fusion in Protein Engineering—Design of novel peptides and bifunctional enzymes," in 1999. Her research interests are novel nanostructures, medical imaging, and protein engineering. She is the founder and CEO of Genovis AB, a Swedish company focusing on novel nanostructures for research and commercial use within the life science industry. She is also in partnership with Lund University in a project developing nanostructures for sentinel node detection. Dr. Fredriksson is an active member of the Lund University Board of Directors, of the board of SwedeNano, and the board of Sparbankstiftelsen Skånes Venture Capital Foundation.



Fredrik Olsson was born in Löddeköpinge, Sweden, in 1971. He finished his M.Sc. degree in biotechnology engineering at Lund University and currently holds an industrial Ph.D. student position in the Department of Pure and Applied Biochemistry at Lund University. His research interests are nanoparticle design and manufacturing as well as bioconjugation to nanostructures. Fredrik also has a significant interest in design and expression of novel enzymes.

He is currently COO of Genovis AB in Lund, Sweden.



Hans W. Persson (M'89) received the M.Sc. and Ph.D. degrees in 1975 and 1980, respectively, from the Lund Institute of Technology, Lund University, Sweden. He worked as a visiting research engineer in 1977–1978 at the University of Rochester, Rochester, NY. Since then, he has been with the Lund Institute of Technology, Department of Electrical Measurements and in 1999, he was promoted to professor in electrical measurements. His research interests include ultrasound transducer design, ultrasonic field measurements, acoustic streaming, air-coupled ultrasound, blood perfusion measurements, vessel characterization, and bioacoustics.



Tomas Jansson (M'05) was born in Hagfors, Sweden, in 1967. He received the M.Sc. and the Ph.D. degrees in 1993 and 1999 from Lund University, Lund, Sweden. After holding positions at the University of Rochester, Rochester, NY, Linköping University, and Lund University, he is now an Associate Professor in Biomedical Engineering in the Department of Electrical Measurements at Lund University. His Ph.D. thesis concerned Doppler measurements of blood perfusion, and even though his later research interests have gravitated towards applications of contrast agents for diagnostic ultrasound, other projects still are focused on Doppler ultrasound, such as staging of sinusitis, and auditory perception of Doppler signals.

Paper II

Normalization of Magnetic Field Effects: Towards Quantitative Magnetomotive Ultrasound Imaging

Maria Evertsson¹, Magnus Cinthio¹, Sarah Fredriksson², Fredrik Olsson², Hans W Persson¹, Tomas Jansson¹

¹Electrical Measurements, Faculty of Engineering, LTH, Lund University, Lund, Sweden

²Genovis AB, Lund, Sweden

Abstract—In magnetomotive ultrasound (MMUS) imaging superparamagnetic iron oxide nanoparticles (NP) are used as contrast agents and a time-varying external magnetic field acts to move the particles and thereby the nanoparticle-laden tissue. Recently we proposed a frequency and phase sensitive algorithm to reduce motion artifacts. However, the method is not quantitative as the particle movement induced is dependent not only on the field strength, but also on the field gradient, plus material parameters. Here we assess the measured nanoparticle movement across the image plane in comparison with simulations of the magnetic force, to evaluate the potential for image normalization of magnetic field effects. We found that the movement decreased with distance to the iron core tip, from which the magnetic field was extending, and approaches zero at the transducer face. This finding did not coincide with the simulation and may make it difficult to enable quantification. The coefficient of variation between measurements on the homogeneous phantom was typically in the order of 15% for all frequencies, indicating the expected accuracy for quantitative measurements.

Keywords- *multimodal imaging; molecular imaging; contrast agents; magnetic field normalizations; quantitative measurements*

I. INTRODUCTION

Molecular imaging is the labeling of contrast agents for different imaging techniques with appropriate tumor/tissue specific markers, e.g. antibodies, enabling changes occurring on a cellular or molecular level to be detected. This is expected to have a major impact on e.g. detection of cancer and cardiovascular disease, individualized treatment, drug development, as well as our understanding of how disease arises [1,2].

The development of molecular imaging for ultrasound contrast agents has not reached as far as for other imaging techniques such as MRI, PET and optical imaging techniques. The foremost reason is that conventional ultrasound contrast agents are confined to the vascular system, as they are comprised of micrometer-sized bubbles [3]. The fact that ultrasound contrast agents are relatively large bubbles, also mean a difficulty to attach to a target, as the shear force from the blood tends to drag the bubble away. New types of contrast agents would likely increase the possible molecular imaging applications for ultrasound [4].

In 2006 Oh et al proposed a new technique called magnetomotive ultrasound (MMUS) imaging which made it possible to detect superparamagnetic ironoxide nanoparticles

This study was supported by grants from the Swedish Research Council, The Knut and Alice Wallenberg foundation, The Crafoordska Foundation and The Royal Physiographic Society in Lund.

(NP) with ultrasound [5]. This type of particles have been used as MRI contrast agents for more than one decade and are small enough to be used as molecular imaging probes [6]. The MMUS imaging technique is built on the same key principle as Magnetomotive OCT (MMOCT) first demonstrated in 2005 [7]. A time-varying magnetic field applied to the volume where the nanoparticles are deposited induces a displacement of the magnetic particles, and thereby their surrounding. For MMUS imaging this movement can be detected with traditional Doppler techniques [5], M-mode techniques [8] quadrature detection with the frequency of the oscillating nanoparticles [9], or correlation techniques with a pulsed (or sinusoidal) magnetic field [10].

However, none of these methods are quantitative as the particle movement induced by the external magnetic field is dependent not only on the field strength, but also on the field gradient, plus material parameters. Here we assess the measured nanoparticle movement across the image plane in comparison with simulations of the magnetic force, to evaluate the potential for image normalization of magnetic field effects.

II. MATERIAL AND METHODS

A. The nanoparticles

The nanoparticles (Genovis AB, Lund, Sweden) were made of solid iron oxide cores of Fe_3O_4 , which were coated with polyethylene glycol (PEG, molecular weight 2000-4000g/mol) to stabilize the suspension. The diameter of the particles was measured to be 18 ± 2 nm, including coating, using transmission electron microscopy (TEM). The magnetic saturation of the nanoparticles was approximately 80 emu/g Fe_3O_4 .

B. The phantom

The phantom was made of 5% by weight polyvinyl alcohol (PVA), to act as a tissue-mimicking material. The crystallized PVA (average Mw 85,000-124,000, 98-99% hydrolyzed, Sigma-Aldrich, USA) was dissolved in MilliQ water in an autoclavable glass bottle sealed with a polypropylene plug and put in a Nüve FN300 oven at 95 °C for 2 hours. When the PVA was completely dissolved, 30 mg graphite (Graphite, Merck KGaA, Darmstadt, Germany) per milliliter solution was added to act as the scattering media in the ultrasound image. The PVA solution was poured into a tube containing SPIO nanoparticles in the concentration needed to form a solution of 0.45mg iron oxide/ml. The solution in the tube was mixed and poured into a

rectangular phantom mold which underwent two freeze-thaw cycles to crosslink the mixture. The rectangular phantom ($2 \times 1.5 \times 1$ cm) was then taken out of the mold and put in a latex wrap together with ultrasound gel. The latex wrap was used make it possible to attach the phantom to the ultrasound transducer.

C. Experimental setup

The measurements were made with a high-frequency ultrasound scanner, VisualSonics Vevo 2100 (VisualSonics Inc., Toronto, ON, Canada). The setup is shown in Fig. 1. The phantom in the wrap was taped to the transducer (MS250, 10–25 MHz bandwidth, transmit center frequency 21MHz) together with ultrasound gel to provide acoustic contact. The phantom was then positioned over a cone-shaped iron core surrounded by a solenoid (Ledex 6EC, Saia-Burgess Inc., USA), which induced a magnetic field when a current was applied. Ultrasound gel was applied to the tip of the iron core to make it visible in the ultrasound image. The electric signal to control the magnetic field strength was produced by a function generator (HP 33120, Agilent technologies, Santa Clara, CA, USA), amplified by a power amplifier (in-house designed, 3dB bandwidth 6-20000 Hz). The signal to the coil was monitored with an oscilloscope (Tektronix TDS 360, Tektronix Inc, Beaverton, OR, USA) and the voltage amplitude was adjusted to be constant over the investigated frequency range. The maximum magnetic field strength was measured just above the iron-core tip using a gaussmeter (FW Bell 9200, Litho, USA, transversal probe, type HTB92-0608) to be 0.18 T.

A sinusoidal voltage, with frequencies 5, 10 and 15 Hz and magnitudes 10, 20, and 30 Vpp, was applied to the solenoid. Three different cross sections were obtained for every frequency at every voltage. The radio frequency in-phase quadrature (RF IQ) image cine loop data was collected and exported to Matlab™ R2009a (MathWorks Inc., Natick, MA, USA), where our frequency-tracking algorithm was implemented. The RF capture frame rate was 100 frames/s, the imaging depth 20.0 mm, the line density 256 lines/frame, and the number of samples per line was 456.

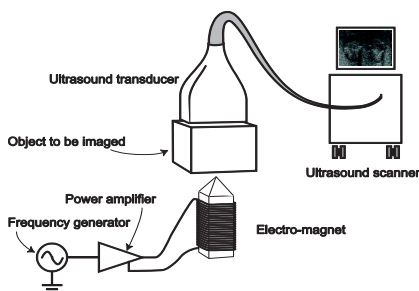


Figure 1: Experimental setup

D. Frequency-tracking and phase-gating algorithm

The algorithm calculated the amplitude of the movement in each pixel at frequency f_0 , the frequency with which the

nanoparticles oscillates (twice the frequency of the voltage applied on the solenoid). The algorithm is earlier partly described [9], but repeated here in short..

Let $r_{IQ}(x, y, m)$ ($m = 1, 2, \dots, M$) denote the IQ-data from cineloop of M frames, where (x, y) (x :lateral, y :axial) corresponds to the coordinates of a position in the image plane. The phase $r(x, y, m)$, for each spatial position throughout all frames was calculated by taking the argument of the IQ-data, $r(x, y, m) = \arg(r_{IQ}(x, y, m))$ and was then quadrature detected with f_0 :

$$R(x, y, m) = r(x, y, m) \times e^{j2\pi f_0 m \Delta t} = \\ I(x, y) + jQ(x, y) \quad (1)$$

where Δt corresponds to the time interval between two frames. To obtain the amplitude at the frequency f_0 for each pixel, a mean value of the quadrature detected sequence $R(x, y, m)$ was calculated.

$$\overline{R(x, y)} = \overline{I(x, y)} + j\overline{Q(x, y)} \quad (2)$$

The amplitude in radians, was then given as

$$A(x, y) = 2\sqrt{I(x, y)^2 + Q(x, y)^2}. \quad (3)$$

To obtain the movement in micrometers, the following relation was used

$$A_{\mu m}(x, y) = \frac{A(x, y)}{2\pi} \times \frac{c}{f_c} \quad (4)$$

where f_c is the center frequency of the transducer and c is the speed of sound in the phantom ($1540 \times 10^6 \mu\text{m/s}$).

E. Evaluation

To evaluate the magnetic field distribution a color-coding of the phantom with regard to displacement was made when the excitation voltage applied on the solenoid was 30Vpp and 5Hz. A mean value for three different cross sections was calculated for each pixel after correlating the iron core's tip in the different images.

To illustrate how the displacement decrease with distance from the tip, a graph was made showing the mean movement in micrometer along the vertical ultrasound line extending from the tip of the iron core to the transducer. Each line in the graph illustrates the mean value of three ultrasound lines, each from a different cross section of the phantom. Before an averaged line was calculated the ultrasound line extending from the tip in two of the cross sections was resampled and interpolated to make the lines equal in length. The reduction in length compared to the uninterpolated length was 3.9 respectively 9.8%. As a comparison a simulation of the magnetic force (field strength times its gradient) for a corresponding situation was also performed in COMSOL Multiphysics and the centerline over the tip was included in the graph.

A normalization of the mean movement along the line extending from the iron core tip (sample 50:250), for the 5Hz measurement was done, using the mean 5Hz 30Vpp measurement.

The influence of solenoid excitation frequency on the

displacement was also investigated. For each of the five most centered ultrasound lines over the iron core tip in each cross section, the mean values of the displacement were calculated. This was done for the three cross sections with same solenoid excitation voltage and frequency, and a mean value and a standard deviation was computed. To indicate the accuracy for quantitative measurements the coefficient of variation was calculated as this mean value divided by the corresponding standard deviation.

III. RESULTS

Fig. 2(A) shows an image color-coded with regard to the amplitude of the measured displacement, $A_{\mu\text{m}}$, in the phantom. The amplitude in each pixel is a mean value of three measurements. Due to the uniform distribution of nanoparticles and graphite in the phantom the figure also represents the impact of the magnetic field distribution in the phantom. The magnet is located at the bottom center, and the transducer along the top. The maximum movement was 2.9 μm and is color-coded as white. The figure indicates that the displacement in the phantom decreases with increasing distance to the tip of the iron core.

The solid lines in Fig. 2(B) displays the movement along the vertical ultrasound line extending from the tip of the magnet for three excitation voltages, 10, 20, and 30 Vpp, all at 5Hz. Each line is mean of three measurements. The dotted line illustrates the simulated magnetic force (magnetic field times its gradient), and is scaled to fit in the figure. Overall, the movement decreases with expanding distance from the iron core tip and approaches zero at the transducer face. The graph also shows an increasing movement with higher voltages.

Fig. 2(C) illustrates the normalized movement along the line extending from the iron core tip (sample 50:250), for different voltages, at 5Hz. Each square is a mean of three measurements. The averaged 5Hz 30Vpp measurement serves as normalization value and the standard deviation is marked with errorbars. The graph shows that the displacement scales linear with applied voltage above a threshold voltage of approximately 4V.

Fig. 2(D) shows a graph where the mean movement along the five most centered lines over the iron core tip is plotted against the excitation frequency applied on the solenoid. The plot shows the average of three cross sections (with five mean value each) and the standard deviation of these measurements.

The coefficient of variation between measurements on the homogeneous phantom was typically in the order of 15%.

IV. DISCUSSION

To take magnetomotive ultrasound imaging one step closer to be a quantitative imaging technique we have investigated the induced displacement in a PVA phantom with a homogeneous distribution of magnetic nanoparticles and graphite during excitation of a time-varying magnetic field. Independent of applied field strength the movement was largest just above the iron core tip, from which the magnetic field was produced, and

decreased to be zero at the edges of the phantom. The latter fact suggests that the transducer and latex wrap act as rigid boundaries for particle movement. Away from the boundaries the magnetic force appears to be dominant. The zero movement at the boundaries may pose a problem for quantification in vivo and further investigations are needed to determine the origin of the phenomenon.

The simulation of the magnetic force coincided well with the measurements a small distance from the tip of the iron core but closest to the tip the simulation and measurement differ. The simulated magnetic force seems never to reach zero, while the measurements reach zero at the phantom boundary. The absence of the transducer interface as well as the lack of a recoiling force in the simulation probably causes this difference.

The movement of the nanoparticles decreased when the frequency of the magnetic field increased. One explanation might be that the energy of the wave motion is proportional to both the displacement and frequency squared. As the applied energy was kept constant, the displacement will need to decrease with frequency. Other explanations include frequency dependent losses in the amplifier, the coil, and the iron core. However, all frequencies were detectable, thereby providing sufficient opportunity to change the excitation frequency in case of an interfering disturbance.

We had anticipated a decrease between the 10 and 15Hz measurements, but this may be explained as a statistical variation since the standard deviation is quite high.

As expected the displacement of the particles increased with an increased excitation voltage on the solenoid, higher amplitude on the magnetic field creates higher amplitude on the displacements. The displacement scaled linearly with applied solenoid voltage, above a threshold voltage (approximately 4V). This threshold voltage has been described previously [10].

The coefficient of variation between measurements on the homogeneous phantom was in the order of 15%, indicating the accuracy for quantitative measurements.

V. CONCLUSION

In this study we have taken a first step to make MMUS imaging quantitative. The movement in a PVA phantom with a uniform distribution of SPIO-NPs has been examined for different excitations voltages and frequencies applied on the solenoid creating the magnetic field. The results show that the movement decreases with an increasing distance from the tip of the iron core from which the magnetic field is extending, and the movement decreases to zero at the edges of the phantom. This zero movement did not coincide with the simulation of the magnetic force and is probably due to the transducer and the latex wrap in which the phantom is placed and that act as rigid boundaries. Similar boundary conditions are likely to appear in vivo and may pose a problem for future quantization of MMUS images.

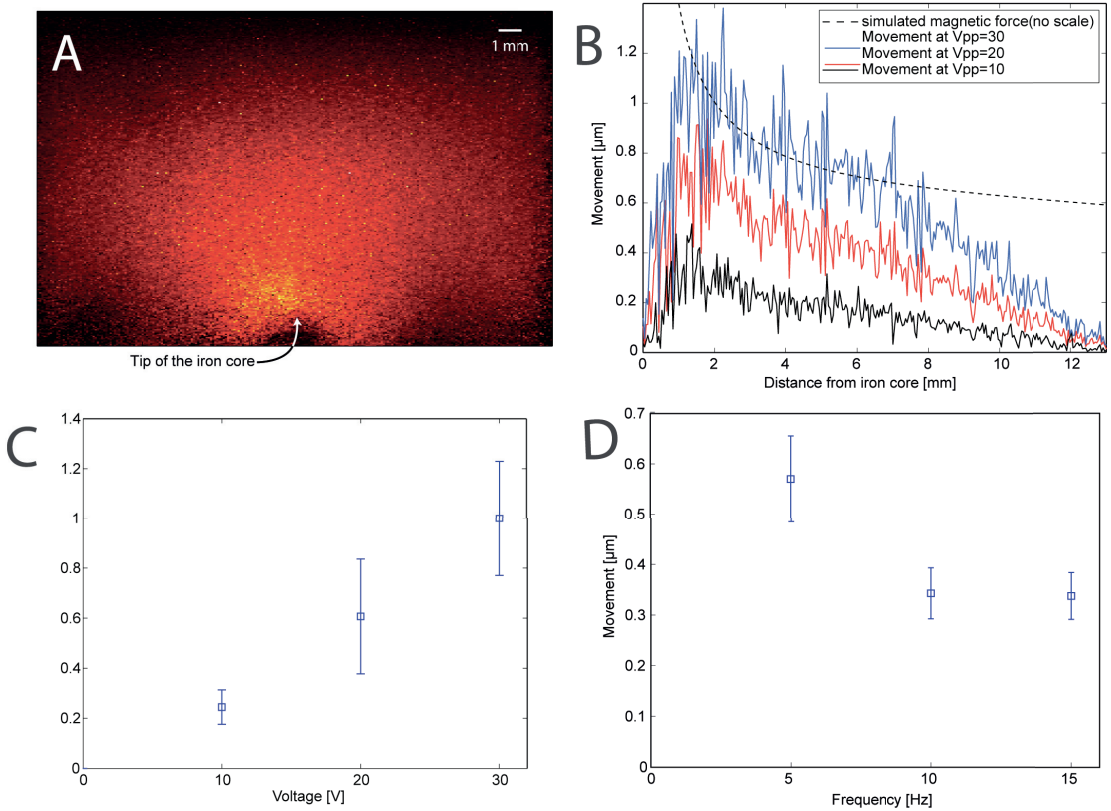


Figure 2. (A) A MMUS image of the phantom with displacement in color-code. The tip of the iron core, from which the magnetic field is extending, is located at the bottom center, and the transducer is positioned along the top. The maximum movement was measured to be $2.9 \mu\text{m}$ and is color-coded as white. Note the 1mm bar in the top right corner. (B) The movement along the vertical ultrasound line extending from the tip of the iron core for three voltages, all at 5Hz . Each solid line is a mean of three measurements. The dotted line represents the simulated magnetic force (field times its gradient) and is scaled to fit in the figure. (C) Normalized mean movement (each square: three measurements) along the line extending from the iron core tip, for different voltages at 5Hz . Standard deviation is marked with errorbars. (D) Mean displacement along the five most centered ultrasound lines extending from the tip. Each square represents a mean of three cross sections (with five mean values each, one value from each ultrasound line). The solenoid excitation voltage was 30Vpp . The standard deviation of the mean from the five most central image lines from the three cross sections is marked with errorbars.

REFERENCES

- [1] R. Weissleder, "Molecular imaging in cancer," *Science*, vol. 312, pp. 1168-1171, 2006.
- [2] S. A. Schmitz, M. Taupitz, S. Wagner, K.-J. Wolf, D. Beyersdorff, and B. Hamm, "Magnetic Resonance Imaging of Atherosclerotic Plaques Using Superparamagnetic Iron Oxide Particles," *J Magn Reson Im*, vol. 14, pp. 355-361, 2001.
- [3] S. Menakura, N. Brown, C. Staton, and M. Reed, "Angiogenesis in pre-malignant conditions," *Brit j cancer* vol. 99, pp. 1961-1966, 2008
- [4] G. M. Lanza, D. R. Abendschein, and C. S. Hall, "In vivo molecular imaging of stretch-induced tissue factor in carotid arteries with ligand-targeted nanoparticles," *J Am Soc Echocardiog*, vol. 13, pp. 608-614, 2000.
- [5] J. Oh, M. D. Feldman, J. Kim, C. Condit, S. Y. Emelianov, and T. E. Milner, "Detection of magnetic nanoparticles in tissue using magneto-motive ultrasound," *Nanotechnology*, vol. 17, pp. 4183-4190, 2006.
- [6] J-H. Lee1, Y-M. Huh, Y. Jun, J. Seo, J. Jang, H-T. Song, S Kim, E-J. Cho, H-G. Yoon, J-S. Suh and J. Cheon, "Artificially engineered magnetic nanoparticles for ultra-sensitive molecular imaging", *Nat Med*, vol 13, pp 95-99, 2007.
- [7] A. L. Oldenburg, J. R. Gunther, and S. A. Boppart, "Imaging magnetically labeled cells with magnetomotive optical coherence tomography," *Opt Lett*, vol 30, pp 747-749, 2005.
- [8] M. Mehrmohammadi, J. Oh, L. Ma, E. Yantsen, T. Larson, S. Mallidi, S. Park, K. P. Johnston, K. Sokolov, T. Milner, and S. Emelianov, "Imaging of Iron Oxide Nanoparticles Using Magneto-Motive Ultrasound," in Proc IEEE Ultrason Symp, pp 652-655 2007
- [9] M. Holst, M. Cinthio, S. Fredriksson, F. Olsson, H.W. Persson, T. Jansson, "Phase-locked magnetomotive ultrasound imaging of superparamagnetic iron-oxide nanoparticles," in Proc IEEE Ultrason Symp, pp 1007-1010, 2010
- [10] M. Mehrmohammadi, J. Oh, S. Aglyamov, A. Karpiouk, and S. Y. Emelianov, "Pulsed magneto-acoustic imaging," in Proc 31st Ann Int IEEE EMBS Conf , pp. 4771-4774, 2009.

Paper III

Multimodal Detection of Iron Oxide Nanoparticles in Rat Lymph Nodes Using Magnetomotive Ultrasound Imaging and Magnetic Resonance Imaging

Maria Evertsson, *Student Member, IEEE*, Pontus Kjellman, Magnus Cinthio, *Member, IEEE*, Sarah Fredriksson, Rene in 't Zandt, Hans W. Persson, *Member, IEEE*, and Tomas Jansson, *Member, IEEE*

Abstract—Detection and removal of sentinel lymph nodes (SLN) is important in the diagnosis and treatment of cancer. The SLN is the first regional lymph node draining the primary tumor, and if the cancer has spread, it is most likely to find metastases in the SLN. In this study, we have for the first time been able to image the very same contrast agent, superparamagnetic iron oxide nanoparticles (SPIO-NPs), in rat SLNs by using both our frequency- and phase-gated magnetomotive ultrasound (MMUS) algorithm and conventional magnetic resonance imaging (MRI); MMUS *post mortem*, MRI *in vivo*. For both higher NP-concentration and smaller NPs, we found that the MMUS data showed a larger magnetomotive displacement (1.56 ± 0.43 and 1.94 ± 0.54 times larger, respectively) and that the MR-images were affected to a higher degree. The MMUS displacement also increased with lower excitation frequency (1.95 ± 0.64 times larger for 5 Hz compared with 15 Hz) and higher excitation voltage (2.95 ± 1.44 times larger for 30 V compared with 10 V). The results show that MMUS has potential to be used as bedside guidance during SLN surgery, imaging the same particles that were used in prior staging with other imaging techniques.

I. INTRODUCTION

BREAST cancer and malignant melanoma spread mainly through the lymphatic system. If the cancer has spread, it is most likely to find metastases in the sentinel lymph node (SLN), the first lymph node draining the primary tumor [1]. The current gold standard method to find the SLN is lymphoscintigraphy, where a gamma camera (before surgery) and a gamma probe (during surgery) are used to image ^{99m}Tc -labeled nanometer-sized colloids that have been injected sub-dermally or peri-tumorally. A

blue dye may then be injected before surgery to visualize the SLN intra-operatively [2]. When the SLN is found, it is removed by invasive surgery and cancer infiltration is examined using histology during ongoing surgery. The lack of precise anatomic information in the scintigraphic images and the nonspecificity of the tracer, however, often limit the preoperative planning and the identification of the SLN to the experience of the surgeon in the current technique [1]. To achieve a more precise SLN localization, increasing interest and research efforts have been directed to find alternative contrast agents in the past years [3].

Metal-based nanoparticles are currently being extensively used as imaging contrast agents [4]. Because of their small size, it is possible to follow biological events on a molecular level, a key to earlier detection of diseases and understanding how diseases arise [5]. Superparamagnetic iron oxide nanoparticles (SPIO-NP) can be observed by MRI as signal voids in the MR image and have been approved as MRI contrast agents for more than a decade [4]; SPIO-based contrast agents have also shown promising results in different applications for identifying metastases in the reticuloendothelial system, including the liver, spleen, and lymph nodes [6]–[9].

Recently, it has been shown that it is possible to detect SPIO-NP-laden SLNs with MRI, SPECT, and optical techniques in the same animal [10]. By combining the best property of each imaging modality, an improved identification and localization of the SLN will be achieved, and thereby there is potential for improved diagnosis for spread of e.g., breast cancer and malignant melanoma. For instance, combining high anatomical MRI resolution with high sensitivity and quantitative SPECT will increase the possibility of ensuring a more accurate localization of the SLN before surgery. During surgery, more portable techniques can be used as a guide, visualizing the very same contrast particles [10].

Ultrasound, being cost-effective and portable, is an excellent candidate as an intra-operative guide, but the SPIO particles are too small to be imaged directly with conventional ultrasound equipment and new imaging strategies are needed. One solution is to utilize the magnetic properties of SPIO particles to obtain image contrast. Oldenburg *et al.* were the first to demonstrate a magnetomotive imaging technique, using optical coherence tomography [11]. By virtue of a time-varying magnetic field, induced

Manuscript received December 9, 2013; accepted May 21, 2014.

We thank VINNOVA: The Swedish Governmental Agency for Innovation Systems, the Swedish Research Council, The Knut and Alice Wallenberg foundation, The Crafoordskra Foundation, and The Royal Physiographic Society in Lund for financial support.

M. Evertsson, M. Cinthio, and H. W. Persson are with the Biomedical Engineering Department, Faculty of Engineering LTH, Lund University, Lund, Sweden (e-mail: maria.evertsson@bme.lth.se).

P. Kjellman, S. Fredriksson, and R. in 't Zandt are with Geccodots AB, Lund, Sweden.

P. Kjellman is also with Clinical Sciences Lund, Medical Radiation Physics, Lund University, Lund, Sweden.

R. in 't Zandt is also with Lund University Bioimaging Center, Lund University, Lund, Sweden.

T. Jansson is with Clinical Sciences Lund, Biomedical Engineering, Lund University, and Medical Services, Skåne University Hospital, Lund, Sweden.

DOI <http://dx.doi.org/10.1109/TUFFC.2014.3034>

particle movement is used to differentiate particle-laden tissue, as particles also move their immediate surroundings. In 2006, Oh *et al.* showed that it was possible to detect the magnetomotive displacements from SPIO-NP-laden tissue using ultrasound [magnetomotive ultrasound (MMUS)]. The displacement was then detected by proper processing of ultrasound data [12]. Lately, the group has detected SPIO-NPs directly injected in a tumor using the maximum displacement after application of a magnetic impulse [13], [14].

Recently, we developed an MMUS algorithm which tracks displacements through the phase variation of the ultrasound radio-frequency in-phase and quadrature (RF-IQ) data. It is based on quadrature detection and phase gating at the precise frequency of nanoparticle displacement, and the processed signal is then color-coded and superimposed on the B-mode image. The advantage of this algorithm is the effective suppression of unwanted movements at other frequencies. The algorithm has shown promising results in phantom studies but has not yet been verified in animals [15]. If successful imaging can be achieved, this opens a vast array of pre-clinical applications and shows the potential for MMUS to be used *in vivo* as a bedside surgical guide.

The objective of this study was to explore the possibilities of multimodal SPIO-NPs in rat SLNs using both MMUS and MRI (MMUS *post mortem*, MRI *in vivo*) in a clinically relevant animal model. Specifically, it was investigated under what conditions presence of adequate MMUS signal can be established in an animal model; we have examined how different particle sizes and injected concentrations of NPs affect the MMUS and MRI images, as well as how various magnetic field excitation frequencies and voltages in the MMUS setup affect MMUS displacement. Finally, the effect of iron core tip location in the MMUS setup (where the magnetic field extends from) relative to the SLN was investigated.

II. MATERIALS AND METHODS

A. Nanoparticles

The superparamagnetic iron oxide nanoparticles used in this study (Geccodots AB, Lund, Sweden) had two different sizes; 31 and 67 nm, measured by dynamic light scattering. Both types consisted of 11-nm solid iron oxide cores of Fe_3O_4 (magnetite) which were coated with polyethylene glycol of varying molecular weight. The production protocol is described by Kjellman *et al.* [16]. The magnetic saturation of nanoparticles was approximately 80 emu/g Fe_3O_4 .

B. Animal Studies

The model studied was a clinically relevant model, showing drainage through the lymphatic system, as well as accumulation of particles in the sentinel lymph node, the first lymph node that drains the injection site. We

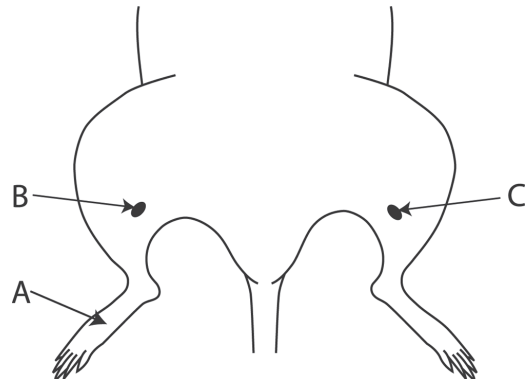


Fig. 1. Schematic sketch of the animal with relevant sites. A 0.1-mL NP solution was injected subcutaneously on the dorsal side of the right hind paw (A). After 24 h, nanoparticles had accumulated in the popliteal node, located at the posterior surface of the right knee (B). The contralateral leg acted as a control in animal 6 (sentinel lymph node C).

chose to inject contrast agent subcutaneously on the dorsal side of the right hind paw (A in Fig. 1), whereby the agent after sufficient time and activity of the animal, is accumulated primarily in the popliteal node, located at the posterior surface of the right knee (B in Fig. 1) [16], [17]. For these experiments, 24 h were allowed between injection and imaging. During this period, the animals were free to move about in their cages. The contralateral leg acted as a control in animal 6 (sentinel lymph node C in Fig. 1).

Eight female Wistar rats (six weeks old, normally grown) were, under anesthesia, injected with 0.1 mL of NP solution, four with 31-nm NPs and four with 67-nm NPs. Two concentrations of the NPs were used; 0.3 and 3 mg of iron/mL; each concentration and particle size was given to two animals, as shown in Table I. The 0.1-mL dose of 0.3 mg Fe/mL corresponded approximately to 0.15 mg of iron/kg of body weight of the animal. Although not directly comparable because of different iron oxide core sizes, it is in the same range as was previously used subcutaneously in the literature [18], whereas intravenous doses are higher, also for humans [19].

Twenty-four hours post injection, the animals were anaesthetized with isoflurane and T2*-weighted MR-images were acquired (3D gradient echo, TE 6 ms, TR 27 ms, field of view: $60 \times 50 \times 50$ mm, pixel resolution: $234 \times 234 \times 468$ μm ; 2.4T Bruker Avance II system, Bruker Corp., Billerica, MA). Animals were kept warm using hot air and respiration and rectal temperature was monitored (SA Instruments Inc., Stony Brook, NY).

After MR imaging, the animals were sacrificed and their hind legs were shaved to allow optimal contact with the ultrasound probe, after which MMUS imaging with a high-frequency ultrasound system (VisualSonics Inc., Toronto, ON, Canada) was performed. A schematic diagram of the MMUS setup can be seen in Fig. 2. Each rat was positioned between the transducer, MS550D (25 to 35 MHz bandwidth, center frequency 32 MHz; Visu-

TABLE I. SUMMARY OF THE DIFFERENT NP CONCENTRATION AND NP SIZE WHICH WERE GIVEN TO EACH RAT IN THE 100- μ L INJECTIONS.

Rat	Concentration (mg of iron/mL)	Size of the NP (nm)
1	0.3	31
2	0.3	31
3	0.3	67
4*	0.3	67
5	3	31
6	3	31
7	3	67
8	3	67

*In this measurement there was a loss of information in the RF-IQ ultrasound data which made it impossible to process the data; the measurement is therefore excluded from the study.

alSonics Inc.), and a solenoid (Ledex 6EC, Saia-Burgess Inc., Deerfield, IL) with a cone-shaped iron core, imaging the popliteal lymph node (SLN), proximal to the injection site. The solenoid was excited with various voltages (10, 20, 30 V_{pp}) and frequencies (5 to 15 Hz, in steps of 2.5 Hz). A function generator (HP 33120, Agilent Technologies Inc., Santa Clara, CA) produced the electric signal which controlled the magnetic field strength and the signal was subsequently amplified by a power amplifier (in-house design, 3-dB bandwidth, 6 to 20000 Hz). The signal to the solenoid was monitored with an oscilloscope (Tektronix TDS 360, Tektronix Inc., Beaverton, OR) and the voltage amplitude was adjusted to be constant over the investigated frequency range. The maximum magnetic flux density in the experimental setup was measured at dc-current to be 0.18 T just above the iron-core tip using a gaussmeter (model 9200, F. W. Bell, Milwaukee, OR; transversal probe, type HTB92-0608) [15]. This value decreases with frequency for constant driving voltage (-20% at 5 Hz, compensated for bandwidth limitation, to -35% at 15 Hz), and also distance from the tip.

By using the Vevo 2100 research interface, the RF-IQ data could be collected and exported to Matlab (The MathWorks Inc., Natick, MA), where our frequency- and phase-gating algorithm was implemented. In short, this consists of retrieving the phase of the received IQ-data for each spatial position throughout all frames. After unwrapping, the phase is quadrature detected with the frequency of particle motion and low-pass filtered (averaged). The displacement rms-magnitude is finally found as twice the length of the phasor spanned by the quadrature components.

For each animal, one cross section for each voltage and frequency was collected when the iron-core tip was positioned directly under the SLN. To investigate how the inhomogeneous magnetic field affected the MMUS displacement, different positions of the iron core tip in relation to the SLN were also studied. Two additional cross sections for each rat were obtained at 5 Hz, 30 V; one when the iron-core tip was positioned on average 3.5 mm horizontally to the left of the SLN and a second on average 3.5 mm horizontally to the right (ranges 3 to 4 mm).

The frame rate used in all measurements was 100 Hz, and each cineloop contained 300 frames.

All studies were conducted in accordance with the Swedish guidelines for the use and care of laboratory animals.

C. Evaluation

To evaluate our algorithm's capability to sort out MMUS displacement in the NP-laden SLN, signal-to-clutter ratios (SCR) were calculated. The lymph nodes were outlined manually from the B-mode images only to avoid operator bias due to the presence of MMUS-signal. After calculation of an average MMUS displacement for both the outlined lymph node and the rest of the pixels in the ultrasound image, an SCR was obtained as the ratio of the average displacement in the lymph node with that in the surrounding pixels in the ultrasound image. Five different images for each rat were created: from the 3D-MRI data set, one axial projection of the popliteal lymph nodes (SLN) in both the right and the left leg was selected to investigate the presence of NP accumulation in the SLN in the injected leg; one grayscale B-mode ultrasound image of the SLN in the injected leg, and finally, three color-coded images which were superimposed on the B-mode image: one showing the total motion at all frequencies, another one showing the phase distribution, and one showing the frequency- and phase-gated MMUS displacement (rms value, as shown in [15]).

The relationship between the average MMUS displacement in the SLN and the applied solenoid excitation frequency and voltage amplitude, respectively, were also evaluated for each rat and displayed in graphs. The same relationships were also investigated and displayed for the control lymph node in rat 6.

III. RESULTS

There was a loss of information in the RF-IQ ultrasound data during the measurement of rat 4, which made it impossible to process the data. The measurement was consequently excluded from the study.

Figs. 3(a)-3(e) displays the SLN in rat 1 (injected with 100 μ L of 0.3 mg/mL solution of 31-nm NPs, excitation voltage on the solenoid in the MMUS setup; 30 V_{pp}, 5 Hz), Fig. 3(f) shows the control side of animal 6 (also for 30 V_{pp}, 5 Hz). The accumulation of SPIO-NPs in the SLN can clearly be seen in Fig. 3(a) because of the void of signal in the T2*-weighted MR image, whereas no such signal void can be seen on the control side. In Fig. 3(c), the total displacement over the entire frequency range (0 to 50 Hz, half the frame rate) is shown as color code superimposed on the B-mode image. In line with previous phantom studies [15], a phase difference of π radians was found between the lymph node and the surrounding fat capsule when the phase distribution at the detected frequency was examined [Fig. 3(d)]. By applying our algorithm, displacements with different frequencies and phases other than the

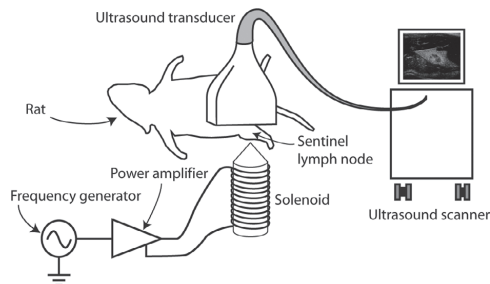


Fig. 2. Schematic diagram of the magnetomotive ultrasound setup. The solenoid produces a time-varying magnetic field that acts to move the superparamagnetic nanoparticles that are lodged in the sentinel lymph node. The resulting movement is detected with ultrasound using a custom-implemented algorithm.

MMUS displacement can be filtered out, resulting in Fig. 3(e). Compare with Fig. 3(f), where the same procedure is applied to the control side of animal 6 where no SPIO-NPs are present. The displacement magnitudes [Figs. 3(c) and 3(e)] and phase distribution [Fig. 3(d)] can be read from the color bars and the displacements are in the same order as in previous phantom studies. Note the different scales.

The signal-to-clutter ratio in the case depicted in Fig. 3(e) was 18.1 dB compared with an average of 10.4 dB, standard deviation ± 1.9 dB, for all measurements.

When the iron core tip was positioned directly under the SLN, a tendency of increasing displacement with decreasing solenoid excitation frequency was found in the MMUS-images, as well as an increased displacement with increasing excitation voltage. This could be seen in all seven rats (Fig. 4). The average displacement for all 5-Hz measurements was 1.95 ± 0.64 times larger than compared with the average for 15 Hz. In the same way, the average displacement was 2.95 ± 1.44 times larger when comparing measurements for which the voltage was increased from 10 V to 30 V. For clarity, error bars are not included in Fig. 4, but the sample standard deviation of the data points are on the order of magnitude as seen in Figs. 5 and 6. Each data point is an average of thousands of pixels (range 4000 to 17000), which makes the standard error considerably smaller.

The MR-signal is, in most cases, completely diminished by the iron oxide, in the dose range used in this study. A higher concentration of iron gives a larger void, sometimes well exceeding the area occupied by the lymph node. It is therefore difficult to speak of MR signal changes in more than in a qualitative way. What can be said is that for both a higher NP-concentration and smaller NPs, the MR-images were affected to a higher degree (Fig. 7), and the MMUS images showed a larger displacement. In Fig. 5, this is illustrated for the 5 Hz, 30 V_{pp} case, where mean displacement and sample standard deviation for all ani-

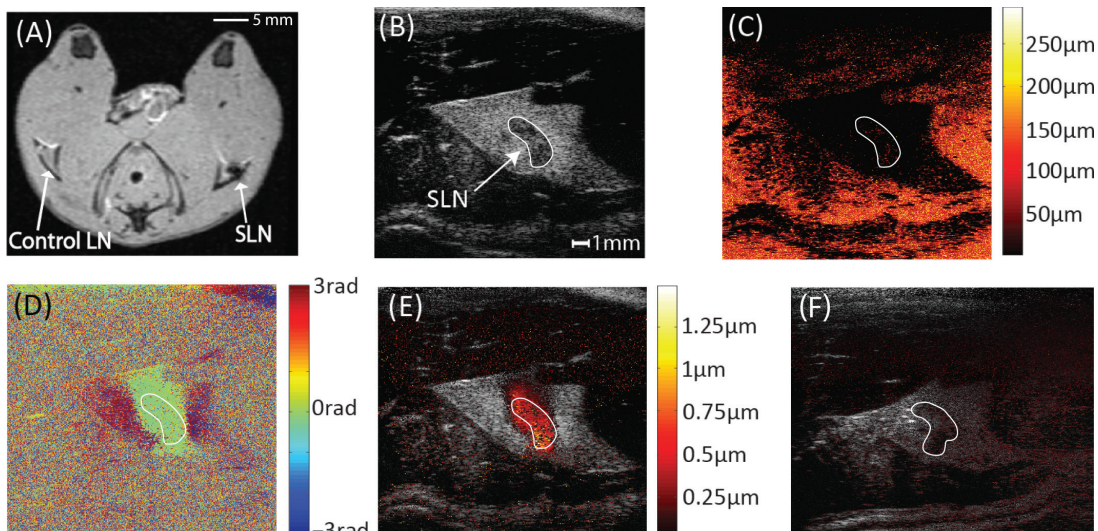


Fig. 3. (A) A T2*-weighted MR image of the popliteal nodes of a rat injected with 100 μ L of 0.3-mg/mL solution of 31-nm NPs. SPIO-NP accumulation can be seen in the SLN in the right knee (arrow) because of the lack of MR signal. On the control side, no NPs are detected. The bar in upper-right corner indicates 5 mm. (B) A B-mode ultrasound image of the NP-laden SLN; note the higher spatial resolution compared with the MRI image. The SLN is outlined with a white border [also in panels (C)–(F)]. (C) The total magnetomotive displacement, i.e., the displacement at all frequencies; (D) the phase distribution at the detected frequency; and (E) the frequency- and phase-discriminative magnetomotive displacement. (F) The frequency- and phase-discriminative magnetomotive displacement seen in the control animal. The color-coding represents magnetomotive displacement (C), (E), and (F), and phase (D), respectively, according to the color bars. Note the different scales. The ultrasound images were obtained at 5 Hz, 30 V_{pp} solenoid excitation. From the phase map (D), it can be seen that the magnetomotive displacement of NP-laden tissue induces a counteracting motion with opposite phase in tissue surrounding the lymph node, effectively suppressed by the algorithm (E). The signal-to-clutter ratio in the case depicted in (E) was 18.1 dB.

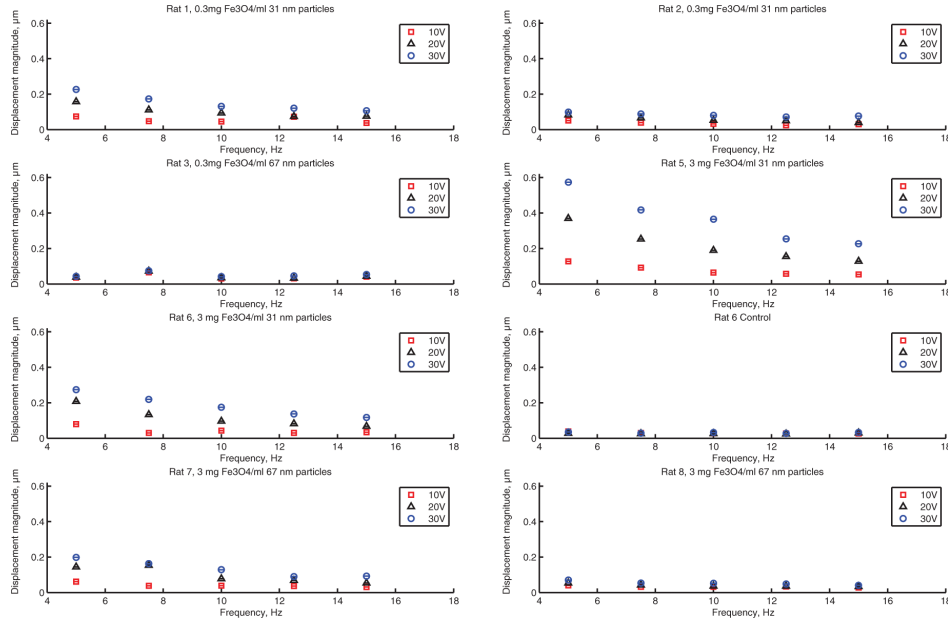


Fig. 4. The magnetomotive displacement in each animal, for various solenoid excitation voltages and frequencies. A tendency of decreasing displacement with increasing solenoid excitation frequency can be seen, as well as an increased displacement with increasing excitation voltage. The graphs also show a larger displacement for both higher NP-concentration and smaller NPs. The sample standard deviations are left out for clarity, but have typically magnitudes as seen in Figs. 6 and 7.

mals at 30 V_{pp}, 5 Hz are plotted. The displacement increase for all animals and excitation parameters was on average 1.56 ± 0.43 times for the higher concentration and 1.94 ± 0.54 times larger for smaller particles. In Fig. 7, the accumulation in (a) rat 2 injected with 0.3 mg/mL of 31-nm NPs, (b) rat 5 injected with 3 mg/mL of 31-nm NPs, and (c) rat 7 injected with 3 mg/mL of 67-nm NPs can be seen. Rat 5, injected with a high concentration of 31-nm NPs, shows a higher signal void compared with rat

2, which was injected with a lower concentration of 31-nm NPs. Rat 5 also shows a higher signal void compared with rat 7, which was injected with larger particles but the same concentration as rat 5.

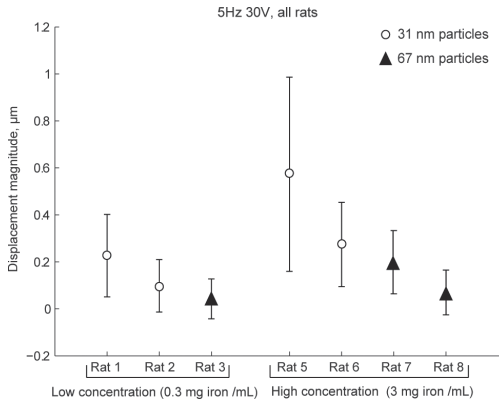


Fig. 5. The magnetomotive displacement amplitude for each rat at 5 Hz, 30 V. A larger displacement for both higher NP-concentration and smaller NPs can be seen. The error bars indicate sample standard deviation.

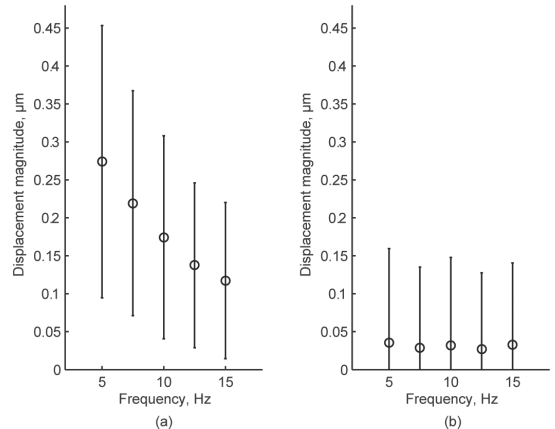


Fig. 6. The graph shows the magnetomotive displacement amplitude in rat number 6 (injected with 100 μ L of 3 mg/mL solution of 31-nm NPs). (a) Results from the popliteal lymph node in the leg which was injected with SPIO-NPs and (b) from the contralateral control leg which had no SPIO-NPs injected. (a) shows a typical magnetomotive displacement behavior, i.e., an increased displacement with lower excitation frequency at the solenoid, whereas (b) shows no frequency behavior. The error bars indicate sample standard deviation.

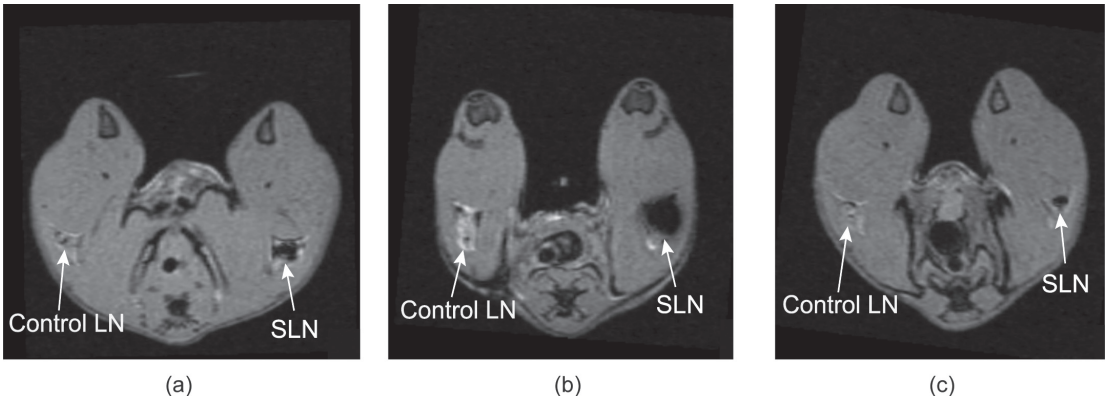


Fig. 7. The image shows the accumulation of SPIO-NP in the SLN in (a) rat 2, (b) rat 5, and (c) rat 7. From the image, it can be seen that a stronger signal void is present when a higher concentration of NPs is injected [compare (b) and (a)] and when smaller NPs are injected [compare panel (b) and panel (c)].

No indication of any MMUS displacement could be found for the lymph node in the control animal (rat 6), only a background noise displacement was found at the detected frequency and phase. Further, there was no dependency between MMUS displacement magnitude and excitation frequency and/or voltage, which were present in all the other measurements where NPs were present. This can be seen in Fig. 6 where the MMUS displacement in the control lymph node is compared with the MMUS displacement in the NP-laden SLN in the same animal. The error bars indicate standard deviation.

The position of the iron core tip in relation to the SLN had an impact on the MMUS displacement according to Fig. 8. The displacement was on average 1.99 ± 1.16 times larger when the tip was positioned directly under the SLN compared with when the tip was positioned 3 to 4 mm horizontally to the left and 1.53 ± 0.36 times larger when it was positioned 3 to 4 mm horizontally right.

IV. DISCUSSION

In this study, we have shown that it is possible to detect the same SPIO-NPs in rat lymph nodes with both MRI (*in vivo*) and MMUS (*post mortem*), as illustrated in Fig. 3. The MMUS imaging was enabled using our previously developed algorithm [15]. The algorithm filters out motion artifacts, leaving only the desirable MMUS signal, which is converted to color code and superimposed on the B-mode image, efficiently enhancing the NP-laden lymph node [Fig. 3(e)]. Compared with MRI, which has a disadvantage of not being quantitative (the signal disappears for a large enough concentration of iron oxide), MMUS holds the promise to be a quantitative tool for detection of SPIO-NPs.

In Fig. 3(d), it can be seen that the MMUS displacement of the NP-laden SLN induces a counteracting motion with a π -rad phase shift in tissue surrounding the lymph node. This out-of-phase displacement was distinct

in our previous phantom studies [15], but it was uncertain whether it would exist in an animal or was a result of the phantom design. Oldenburg *et al.* [20] have earlier explained this π -rad phase shift as a consequence of diamagnetic response from the media not containing superparamagnetic particles, but we could detect only minute movement with no preferred phase when SPIO-NPs were absent, both in our phantom study [15] and in this animal study. We argue instead that the phase shifted displacement is due to the mechanical coupling; an upward movement in the lymph node is counteracted by a downward movement in surrounding tissue. To what extent magnetomotive motion affects surrounding media is subject to further investigation.

The MMUS displacement dependency on frequency and solenoid excitation voltage as well as NP concentra-

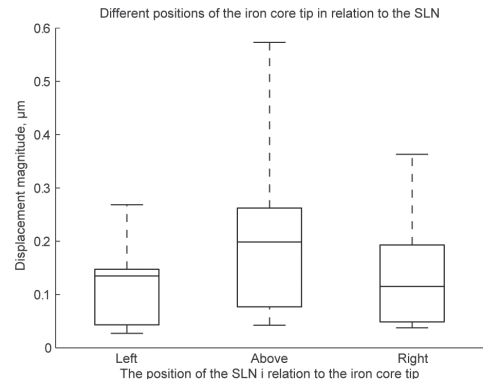


Fig. 8. The figure shows a boxplot of the average magnetomotive displacement amplitude in the SLNs for all seven rats for three different iron core tip positions in relation to the SLNs; when the tip is positioned directly under the lymph node and when it is positioned 3 to 4 mm to the left (respectively the right). The solenoid excitation was 5 Hz, 30 V. It can be seen from the graph that the displacement is affected by the tip position, because the displacement is higher when the tip is placed directly below the SLN.

tion has previously been shown in phantoms [15], [21]. Just as in those studies, an increased MMUS displacement was found when the excitation voltage on the solenoid increased and when the frequency decreased. The decrease with frequency is most likely caused by the solenoid's increasing impedance with frequency. We do not exclude the possibility of this also being a contribution from the viscoelastic response of tissue, but at this point we have no evidence for this being the case. As expected, we also recorded an increasing displacement magnitude for the higher concentration.

A threshold effect restricting the particles to move at lower voltages has been indicated earlier [15], [21]. To overcome this threshold effect, the NP concentration and/or voltage applied on the solenoid can be increased and/or the frequency decreased. In this study, it was possible to detect MMUS displacements at all settings, showing that the parameters used were large enough to overcome the assumed threshold for this application.

When a smaller NP size was used, a larger MRI and MMUS response could be seen. The reason for this is probably that the smaller particles accumulate faster in the SLN compared with the larger particles [16]. Note that the core size, and thereby iron content, is the same for small and large particles—it is only the polyethylene glycol coating that affects the total particle size. This justifies the assumption that MRI and MMUS response scales with the number of particles.

As seen in Fig. 6, the lymph node that acted as control (in rat 6) did not show any frequency- or voltage-dependent displacement. Furthermore, the phase map for the control lymph node measurements showed a random phase distribution over the lymph node. This was expected because no SPIO-NPs were present and no MMUS displacement was likely to exist. The magnetomotive response in the contralateral lymph node was considerably higher, though significance levels are not provided because the pixel values were not normally distributed. Because of the large number of pixel values, still, a test for difference comparing a NP-laden lymph-node with the control for each frequency shows high statistical significance (*p*-values are practically zero) in all cases.

As the iron core tip was displaced sideways relative to the SLN, the MMUS displacement decreased. This was expected because of the inhomogeneous magnetic field which extends from the cone-shaped iron core. The result is in line with previous phantom studies [22] and shows that it is desirable to place the tip as close to the SLN as possible, and apply compensation for the magnetic field for quantitative measurements. The design with a magnetic field generator on the opposite side of the ultrasound transducer will naturally pose a challenge for a clinical translation. Current efforts focus on a solution in which the magnetic field can be applied from the same side as the ultrasound probe, similar to the design that recently was suggested by Pope *et al.* [23]. It is also crucial to show the validity of the technique in live animals, which includes the choice of

a suitable magnetic field frequency that does not interfere with any physiological activity, such as heart rhythm.

Because of the *post mortem* nature of these experiments, there were no artifactual movements (breathing, heart beats, etc.) to interfere with magnetomotive motion. Therefore, the results are not directly translatable to an *in vivo* situation, but certainly the results of this study point in the direction that MMUS has potential as a stand-alone modality for other imaging applications aside from a pre-operative guide for the surgeon during SLN detection and removal, such as stem cell tracking and cardiovascular research.

V. CONCLUSION

In this study, we have for the first time shown truly multimodal imaging by detecting SPIO-NPs in rat sentinel lymph nodes using both MRI and MMUS imaging. Further, we have established magnetic excitation parameters for successful MMUS imaging in a preclinical SLN model by using our recently developed frequency- and phase-gated algorithm.

REFERENCES

- [1] R. Madru, P. Kjellman, F. Olsson, K. Wingardh, C. Ingvar, F. Stahlberg, J. Olsrud, J. Latt, S. Fredriksson, L. Knutsson, and S. E. Strand, “ 99m Tc-labeled superparamagnetic iron oxide nanoparticles for multimodality SPECT/MRI of sentinel lymph nodes,” *J. Nucl. Med.*, vol. 53, no. 3, pp. 459–463, 2012.
- [2] J. Buscombe, G. Paganelli, Z. E. Burak, W. Waddington, J. Maublant, E. Prats, H. Palmedo, O. Schillaci, L. Maffioli, M. Lassmann, C. Chiesa, E. Bombardieri, and A. Chiti, “Sentinel node in breast cancer procedural guidelines,” *Eur. J. Nucl. Med. Mol. Imaging*, vol. 34, no. 12, pp. 2154–2159, 2007.
- [3] R. Jain, P. Dandekar, and V. Patravale, “Diagnostic nanocarriers for sentinel lymph node Imaging,” *J. Control. Release*, vol. 138, no. 2, pp. 90–102, 2009.
- [4] R. Qiao, C. Yang, and M. Gao, “Superparamagnetic iron oxide nanoparticles: From preparations to *in vivo* MRI applications,” *J. Mater. Chem.*, vol. 19, no. 35, pp. 6274–6293, 2009.
- [5] R. Weissleder, “Molecular imaging in cancer,” *Science*, vol. 312, no. 5777, pp. 1168–1171, 2006.
- [6] J. T. Ferrucci and D. D. Stark, “Iron oxide-enhanced MR imaging of the liver and spleen: Review of the first 5 years,” *Am. J. Roentgenol.*, vol. 155, no. 5, pp. 943–950, 1990.
- [7] M. F. Bellin, C. Beigelman, and S. Precetti-Morel, “Iron oxide-enhanced MR lymphography: Initial experience,” *Eur. J. Radiol.*, vol. 34, no. 3, pp. 257–264, 2000.
- [8] M. Russell and Y. Anzai, “Ultrasmall superparamagnetic iron oxide enhanced MR imaging for lymph node metastases,” *Radiography*, vol. 13, suppl. 1, pp. 73–84, 2007.
- [9] M. G. Harisinghani, M. A. Saksena, P. F. Hahn, B. King, J. Kim, M. T. Torabi, and R. Weissleder, “Ferumoxtran-10-enhanced MR lymphangiography: Does contrast-enhanced imaging alone suffice for accurate lymph node characterization,” *Am. J. Roentgenol.*, vol. 186, no. 1, pp. 144–148, 2006.
- [10] R. Madru, F. Olsson, K. Wingardh, S. Fredriksson, C. Ingvar, E. Carleman, J. Olsrud, J. Latt, F. Stahlberg, and S. E. Strand, “Preparation and characterization of 99m Tc-labeled superparamagnetic iron oxide (IO) nanoparticles for multimodality imaging (MRI/SPECT) of SLN,” in *Proc. Int. Society for Magnetic Resonance in Medicine and Biology Conf.*, 2009, p. 3695.
- [11] A. L. Oldenburg, J. R. Gunther, and S. A. Boppart, “Imaging magnetically labeled cells with magnetomotive optical coherence tomography,” *Opt. Lett.*, vol. 30, no. 7, pp. 747–749, 2005.

- [12] J. Oh, M. D. Feldman, J. Kim, C. Condit, S. Y. Emelianov, and T. E. Milner, "Detection of magnetic nanoparticles in tissue using magneto-motive ultrasound," *Nanotechnology*, vol. 17, no. 16, pp. 4183–4190, 2006.
- [13] M. Mehrmohammadi, J. Oh, S. Mallidi, and S. Y. Emelianov, "Pulsed magneto-motive ultrasound imaging using ultrasmall magnetic nanopropes," *Mol. Imaging*, vol. 10, no. 2, pp. 102–110, 2011.
- [14] M. Mehrmohammadi, T.-H. Shin, M. Qu, P. Kruizinga, R. L. Truby, J.-H. Lee, J. Cheon, and S. Y. Emelianov, "In vivo pulsed magneto-motive ultrasound imaging using high-performance magnetoactive contrast nanoagents," *Nanoscale*, vol. 5, no. 22, pp. 11179–11186, 2013.
- [15] M. Evertsson, M. Cinthio, S. Fredriksson, F. Olsson, H. W. Persson, and T. Jansson, "Frequency- and phase-sensitive magnetomotive ultrasound imaging of superparamagnetic iron oxide nanoparticles," *IEEE Trans. Ultrason. Ferroelectr. Freq. Control*, vol. 60, no. 3, pp. 481–491, 2013.
- [16] P. Kjellman, R. in 't Zandt, S. Fredriksson, and S.-E. Strand, "Optimizing retention of multimodal imaging nanostructures in sentinel lymph nodes by nanoscale size tailoring," *Nanomed.: Nanotechnol. Biol. Med.*, vol. 10, no. 5, pp. 1089–1095, 2014.
- [17] N. L. Tilney, "Patterns of lymphatic drainage in the adult laboratory rat," *J. Anat.*, vol. 109, pt. 3, pp. 369–383, 1971.
- [18] M. A. Oghabian, N. Gherehaghaji, S. Amirmohseni, S. Khoei, and M. Guitté, "Detection sensitivity of lymph nodes of various sizes using USPIO nanoparticles in magnetic resonance imaging," *Nanomedicine*, vol. 6, no. 3, pp. 496–499, 2010.
- [19] P. A. Hudgins, Y. Anzai, M. R. Morris, and M. A. Lucas, "Ferumoxtran-10, a superparamagnetic iron oxide as a magnetic resonance enhancement agent for imaging lymph nodes: A phase 2 dose study," *AJNR Am. J. Neuroradiol.*, vol. 23, no. 4, pp. 649–656, 2002.
- [20] A. L. Oldenburg, V. Crecea, S. A. Rinne, and S. A. Boppart, "Phase-resolved magnetomotive OCT for imaging nanomolar concentrations of magnetic nanoparticles in tissues," *Opt. Express*, vol. 16, no. 15, pp. 11525–11539, 2008.
- [21] M. Mehrmohammadi, J. Oh, L. Ma, E. Yantsen, T. Larson, S. Mallidi, S. Park, K. P. Johnston, K. Sokolov, T. Milner, and S. Emelianov, "Imaging of iron oxide nanoparticles using magneto-motive ultrasound," in *Proc. IEEE Ultrasonics Symp.*, 2007, pp. 652–655.
- [22] M. Evertsson, M. Cinthio, S. Fredriksson, F. Olsson, H. W. Persson, and T. Jansson, "Normalization of magnetic field effects: Towards quantitative magnetomotive ultrasound imaging," *Proc. IEEE Ultrasonics Symp.*, 2011, pp. 775–778.
- [23] A. G. Pope, G. Wu, F. Y. McWhorter, E. P. Merricks, T. C. Nichols, T. J. Czernuszewicz, C. M. Gallippi, and A. L. Oldenburg, "Contrast-enhanced imaging of SPIO-labeled platelets using magnetomotive ultrasound," *Phys. Med. Biol.*, vol. 58, no. 20, pp. 7277–7290, 2013.



Maria Evertsson (formerly Holst) (M'10) was born in Malmö, Sweden, 1984. She finished her M.Sc. degree in 2009. Since 2010, she has been a Ph.D. student in Biomedical Engineering, Faculty of Engineering, Lund University, Sweden. Her research area is contrast agents, magnetomotive imaging, and signal processing.



Pontus Kjellman was born in Helsingborg, Sweden, in 1981. He received his B.Sc. degree in biotechnology from Lund University, Sweden in 2004. In 2007, he took employment at Genovis AB, and since 2009 he has been an industrial Ph.D. student, dividing his time between the company and the department of Medical Radiation Physics at Lund University. Pontus's research areas include contrast agent development and sentinel lymph node detection.



Magnus Cinthio (formerly Persson) (M'01) was born in Klippan, Sweden, in 1969. He received the M.Sc. degree in biomedical engineering and the Ph.D. degree in electrical measurements in 1999 and 2004, respectively, from Lund University, Lund, Sweden. In 2010, he became Associate Professor in the Faculty of Engineering, Lund University, Lund. He has been visiting researcher at Tohoku University, Sendai, Japan, in 2007, and at Florence University, Florence, Italy, in 2012. Since 2005, he has held different positions in Electrical Measurements, Faculty of Engineering, Lund University. He obtained a University Lecturer position in 2013. His research interests include ultrasonic tissue motion measurements, signal processing, magnetomotive imaging, as well as arterial, cerebral, and musculature characterization.



Sarah Fredriksson was born in Vänersborg, Sweden, in 1968. Sarah Fredriksson finished her M.Sc. degree in biotechnology engineering from Lund University and received her Ph.D. degree by submitting a thesis with the title "Gene fusion in protein engineering—Design of novel peptides and bifunctional enzymes" in 1999. Sarah Fredriksson's research interests are novel nanostructures, medical imaging, and protein engineering. She is the founder and CEO of Genovis AB, a Swedish company focusing on novel nanostructures for re-

search and commercial use within the life science industry. She is also in partnership with Lund University in a project developing nanostructures for sentinel node detection. Sarah Fredriksson is an active member of Lund University Board of Directors, of the board of SwedeNano, and the board of Sparbankstiftelsen Skånes Venture Capital Foundation.



René in 't Zandt was born in Eindhoven, The Netherlands, in 1970. He finished his M.Sc. degree in physics at the Radboud University Nijmegen, Nijmegen, The Netherlands, in 1995. In 2000 he received his Ph.D. degree after successfully defending his thesis "Plasticity of energy metabolism in creatine kinase deficient mice: An *in vivo* MR spectroscopy study." After a 2-year postdoctoral stint in Leuven, Belgium, he moved to Sweden in 2002. Currently, he is sharing his time between a position as MR physicist at the Lund University

Bioimaging Center, Lund University, Lund, and as preclinical imaging director at Geccodots AB, a fully owned subsidiary of Genovis AB, Lund.



Hans W. Persson (M'97) received the degrees of M.Sc. and Ph.D. degrees in 1975 and 1980, respectively, from the Lund Institute of Technology, Lund University, Sweden. He worked as a visiting research engineer from 1977 to 1978 at the University of Rochester, Rochester, NY. Since then, he has been with Lund Institute of Technology's Department of Electrical Measurements, and in 1999, he was promoted to professor in electrical measurements. His research interests include ultrasound transducer design, ultrasonic field measurements, acoustic streaming, air-coupled ultrasound, blood perfusion measurements, vessel characterization, and bioacoustics.



Tomas Jansson (M'05) was born in Hagfors, Sweden, in 1967. He received the M.Sc. and Ph.D. degrees in 1993 and 1999 from Lund University, Lund, Sweden. After positions at the University of Rochester, Rochester, NY; Linköping University; and Lund University, he is now an Associate Professor in Biomedical Engineering at the Medical Faculty at Lund University. His Ph.D. thesis concerned Doppler measurements of blood perfusion, and even though his later research interests have gravitated towards applications of contrast agents for diagnostic ultrasound, other projects still are focused on Doppler ultrasound, such as staging of sinusitis, and auditory perception of Doppler signals.

Paper IV

Induced tissue displacement in magnetomotive ultrasound imaging - simulations and comparison with phantom and *post mortem* experiments

Tomas Jansson^{1,2}, Maria Evertsson³, Esayas Aatile³, Roger Andersson³, Sarah Fredriksson⁴, Hans W Persson³, Ingrid Svensson³, Magnus Cinthio³

¹Clinical Sciences Lund, Biomedical Engineering, Lund University, Lund Sweden

²Medical Services, Skåne University Hospital, Lund, Sweden

³Biomedical Engineering, Faculty of Engineering LTH at Lund University, Lund, Sweden

⁴Genovis AB, Lund, Sweden

E-mail: tomas.jansson@med.lu.se

Abstract. Magnetomotive ultrasound imaging is an emerging technique that enables superparamagnetic iron oxide nanoparticles to be detected with ultrasound. The contrast is achieved by a time-varying external magnetic field that acts to move magnetic particles lodged in tissue, and ultrasound is used to detect the resulting tissue movement. In previous phantom and animal studies, we have observed opposite phase motion next to regions containing nanoparticles. We hypothesize that mechanical coupling from regions where nanoparticles are located, causes this motion. The present study compares experimental phantom and *post mortem* rat lymph node measurements to a numerical simulation with similar geometry as the experimental set-up. The magnetic force acting on particles was in the simulation, modeled as emanating from a coil with a cone shaped iron core, and applied as a body load in nanoparticle-laden regions. The simulation showed opposed motion in-between/next to nanoparticle-laden regions, in a manner similar to the experimental situations. For the phantom, there was a slight mismatch in the extent and alignment of the movement, which is interpreted as a result of the modeled slip condition tangentially to the surface, which in reality presumably is a combination of slip and stick due to friction. In the *post mortem* case, there was no similar mismatch in extent of the movement, but the simulation showed the induced movement essentially to be confined to the fat capsule surrounding the lymph node, as experienced also in the experimental case.

1. Introduction

Contrast agents for ultrasound in use today are comprised of micrometer-sized bubbles, and thereby confined to the vascular system. Extra-vascular targets are thus currently out of reach for ultrasound contrast agents, which limits the applications for molecular imaging. Nanoscale contrast agents may open up a new diagnostic and therapeutic window for ultrasound, and ongoing research investigate for instance nanodroplets (Lin and Pitt 2013) and various types of nanoparticle sized contrast agents for photoacoustic imaging (Egitedari et al 2003, Zerda et al 2008).

Magnetomotive ultrasound (MMUS) imaging is a new method that enables the use of superparamagnetic iron oxide nanoparticles (SPIO NP) as a contrast agent for ultrasound. These are attractive since they for over a decade have been approved as contrast agents for MRI (Bao et al 2013). A complication for ultrasound is that nanoscale particles have an extremely small scattering cross section

as this scales with their radius to the sixth power (Morse and Ingard 1968). In MMUS, the contrast is instead achieved by virtue of a time-varying external magnetic field whereby NPs are set in motion. Ultrasound can be used to detect the motion, as NPs move also their immediate surrounding. Various excitation and detection strategies have been proposed, such as detection using conventional power or pulsed Doppler (Oh et al 2006) and custom detection schemes for pulsed (Mehrmohammadi et al 2011), or continuous magnetic fields (Evertsson et al 2013).

The fact that SPIO NPs are approved as a contrast agent for MRI, make them an attractive candidate for multimodal imaging. It is the magnetic property that is utilized for generation of image contrast for both MRI and MMUS, but by attaching a radioactive probe, the very same particle can be used for PET or SPECT, depending on the choice of radionuclide. With the attachment of a fluorophore it can also be used for optical imaging, thus providing a contrast agent that can be used for up to five modalities (Jansson et al 2015). This property motivates our choice of first application for MMUS: identification of sentinel lymph nodes during breast cancer surgery. We propose a workflow where disease staging can be performed initially with SPECT/PET/MR, and then intraoperative guidance can be performed with MMUS, utilizing the very same particles for image contrast. For refined diagnostic development, and future alternative applications, the particles lend themselves excellently to applications for molecular imaging, as the conjugation of active molecular moieties to the particle surface is straightforward.

In previous studies we have noted what appears to be an induced displacement occurring laterally outside nanoparticle-laden regions. We however also found that the displacement had opposite phase, and thus, could be filtered out (Evertsson et al 2013). It has been suggested by Oldenburg et al. (2008) that the opposed motion is a result of a diamagnetic response of tissue or material free from iron oxide NPs. They argued that, as tissue mainly is diamagnetic, tissue would normally be displaced in opposite phase with the magnetic field. Therefore, there is a “critical” particle volume density at which the force from the particles that attract towards the magnet, exactly balances the opposing force from tissue. At higher particle concentrations, the net response will appear paramagnetic. This may explain the threshold effect observed by others, and us, where a certain particle concentration, or magnetic force, is needed to obtain a magnetomotive response.

However, in our previous phantom experiments we were unable to measure any diamagnetic effect in phantoms free of SPIO-NP (Evertsson et al 2013). Instead, we hypothesize that the observed large scale opposite motion in presence of SPIO NP, is caused by mechanical coupling from movement of SPIO NP laden regions.

This study aims to investigate this by a numerical simulation of generated displacements in response to a magnetic field. The situations to be modeled are the phantom used in our experiments (Evertsson et al 2013) and an approximate model of a sentinel lymph node with its surroundings (Evertsson et al 2014). The simulation results are compared to experimental data.

2. Materials and methods

2.1. Imaging setup and processing

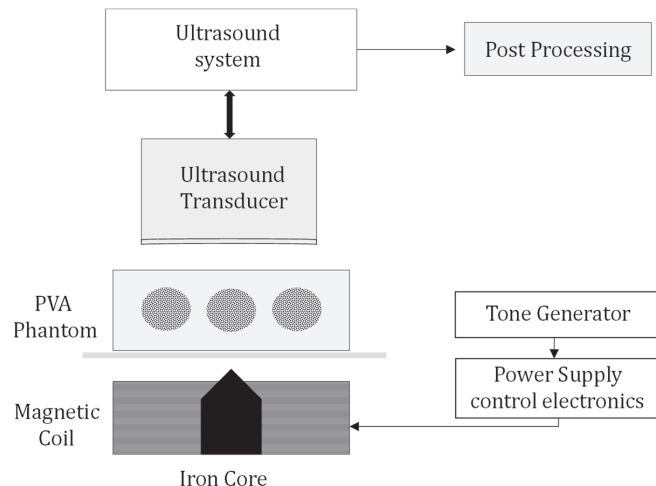


Figure 1. The magnetomotive ultrasound setup as used in the experiments.

The MMUS imaging system is identical to that used by Evertsson et al (2013), but is for convenience summarized here and shown in Fig 1. The key to image SPIO NPs is to apply an external magnetic field. This is provided with a solenoid (Ledex 6EC Saia-Burgess Inc., USA) connected to a function generator (HP 33120, Agilent technologies, Santa Clara, CA, USA) via a power amplifier (in-house designed, 3dB bandwidth 6-20000Hz). The sinusoidal voltage applied to the solenoid was 30 V peak-to-peak, with a frequency of 4 Hz.

The NP motion induced by the magnetic field is detected with a small-animal ultrasound scanner (Visualsonics Vevo 2100, Visualsonics Inc., Toronto, ON, Canada), equipped with a 21 MHz ultrasound probe. The radio-frequency in phase quadrature (RF-IQ) ultrasound data was collected for 3 seconds at a recording rate of 50 frames per second. The data was transferred to a computer and postprocessed in MATLAB. The detection algorithm is essentially that of a lock-in amplifier, where the phase variation of the RF-IQ-data is detected at precisely the frequency of the nanoparticle movement.

2.2. Phantom model

The phantom was made from 5% by weight polyvinyl alcohol (PVA, average Mw 85,000-124,000, 98-99% hydrolyzed, Sigma-Aldrich, USA) according to the procedure outlined in Evertsson et al (2013). Graphite (Vendor) was added to act as ultrasound scattering material. The PVA solution was poured into the phantom mold, with Plexiglas™ forming the walls of the mold. Three Plexiglas™ cylinders created hollows when removed after the PVA had cross-linked, compare Fig. 2. PVA inserts of identical composition and matching diameter was produced, but with added concentration of SPIO-NPs with 0.4, 0.3, and 0.5 mg Fe/ml, respectively, from left to right in the phantom. After the first batch had cross-linked, the inserts were placed in the hollows. All PVA-components underwent two freeze-thaw cycles.

The nanoparticles (Geccodots AB, Lund, Sweden) consisted of 11 nm cores of Fe_3O_4 (magnetite), coated with polyethylene glycol.

2.3. Animal model

The simulation results herein, was compared to image data from a previous study (Evertsson et al 2014). This was a model of clinical relevance, showing drainage through the lymphatic system, as well as accumulation of particles in the sentinel lymph node, the first lymph node that drains the injection site, which in a clinical case is a tumor. SPIO-NPs were injected under anesthesia in the hind paw of the rat, after which the animal was allowed to move around its cage until imaging was performed 24 hours later. For the protocol MR-imaging was performed initially, and after termination of the animal, MMUS imaging commenced. During the period following the injection, the particles migrated in the lymphatic system and accumulated in the popliteal lymph node, the sentinel lymph node in this model.

In the experiments eight female Wistar rats (six weeks old, normally grown) were injected with 0.1 mL NP solution, either with two different coatings, giving the particles two different overall sizes (31 nm and 67 nm, respectively). Two concentrations of the NPs were used; 0.3 and 3 mg iron /mL, each concentration and particle size was given to two animals. We used data from one of the animals with the highest concentration and largest injected particle size.

2.4. *In silico*

2.4.1. Model. A numerical model with the same geometry as the experimental situation was set up in COMSOL (COMSOL, Stockholm, Sweden), see Fig. 2. A solenoid with a cone-shaped iron core surrounded by a current conducting copper coil was modeled to generate the magnetic field. The geometric dimensions of the COMSOL model agreed with the commercial solenoid used in the experiments. For the phantom situation, a polyvinyl alcohol (PVA) cuboid with 5mm diameter inserts was modelled (Fig. 2A). The Plexiglas™ mold was given the same magnetic characteristics as air, and was mechanically modeled as rigid walls.

The ultrasound transducer may be thought of as being oriented in parallel with the long edge of the phantom, so that cross-sections of the nanoparticle-laden inserts are imaged.

For the animal experiment, the simulation situation was somewhat simplified, with the lymph node modelled as a sphere, centered in a triangular region with properties resembling fat (Fig. 2B). Tissues outside the fatty regions, as well as the lymph node, were modelled as the PVA material.

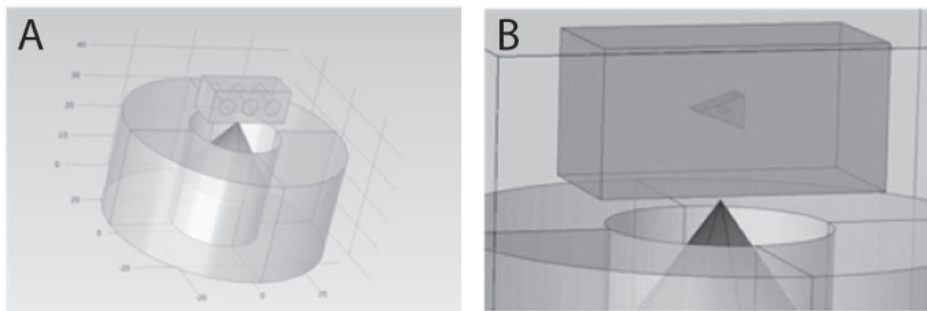


Figure 2. A graphical representation of the simulation situations for the phantom measurements (panel A) and post mortem animal lymph node situation (panel B). A coneshaped iron core is centered within a circuar coil. On top of the iron core the phantom (panel A) consisting of polyvinylalcohol can be seen, as well as its three inserts containing different concentrations of SPIO NPs. To the right the post mortem case. Here, the coneshaped iron core can be seen in the lower part of the figure. The lymph node can be seen as a sphere within the triangular region (green) mimicking the fat capsule surrounding the lymph node.

The material parameters of the iron, copper, and air domains were collected from the COMSOL material library. For PVA, the Young's modulus was measured to 900 Pa (Evertsson et al. 2013), while shear and bulk moduli were set to 10^5 and 0.28×10^9 , respectively. These numbers were consistent with values published in the literature for liver tissue (Glozman and Azhari 2008).

The parameters for the fatty tissue in the lymph node model were set as: Young's modulus: 140 kPa, shear and bulk moduli 46.7 kPa and 2.25 GPa, respectively (Glozman and Azhari 2008).

After the situation was meshed using a triangular grid in the setting "fine", the simulation was ready to run.

2.4.2. Simulations of Magnetic field and Structural mechanics

The simulation was divided in to two parts; simulation of the magnetic field extending from the iron core tip, and simulation of the structural mechanics, modeling the movement of the nanoparticle laden regions. The structural mechanics part uses the magnetic force from the magnetic field simulation as an input.

Given some assumptions and simplifications, the magnetic force, \mathbf{F} , in a given direction (z), is proportional to the magnitude of the magnetic field (\mathbf{B}) times its gradient:

$$\mathbf{F} = \frac{\chi V_m}{\mu_0} \mathbf{B}_z \frac{d\mathbf{B}_z}{dz} \quad (1)$$

Here χ is the magnetic susceptibility of the nanoparticles, μ_0 is the permeability of free space, and V_m is the volume of the magnetic portion of the nanoparticle. Starting from this relation, the magnetic field within the phantom was first calculated, and thereafter the spatial gradient of this field. The resulting magnetic force (the product of the field and its gradient) was then used as input to the structural mechanic's part where the force was applied to the NP-laden regions as a body load (the calculated magnetic force per unit volume) by a relative magnitude corresponding to the NP concentration (Fig. 3). Since precise nanoparticle and material parameters were unknown, the actual values were adjusted so that the resulting displacement was in the same range as that observed experimentally.

Sinusoidal time dependence was chosen, with a frequency of 4 Hz. The tissue mimicking phantom and the inserts both had viscoelastic characteristics. Boundaries were modeled as fixed, but with a slip condition tangentially to the surface.

From the experimental data we noted that nanoparticle-laden regions indeed were affected by a magnetic field, as opposed to a phantom free from particles, and thus the diamagnetic response was not modeled, i.e. the force is set to zero outside the nanoparticle-laden regions.

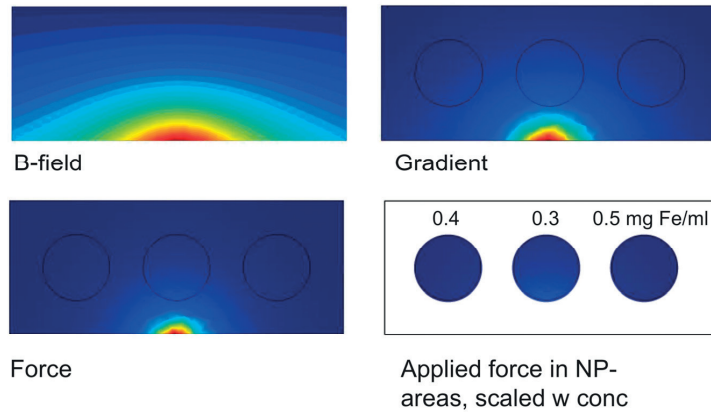


Figure 3. Illustrations of the calculated B-field (A), its gradient (B) and the resulting force (C). In (D) the force field in (C) has been masked to allow force acting on the material only in the regions corresponding to the nanoparticle laden inserts.

3. Results

Fig 4 shows the particle displacement at two locations within the phantom, the upper row at the midpoint of the center insert, and the lower row, in-between the two rightmost inserts. The left panels show the location of the sample point, and the panels to the right, show the displacement the first periods after the magnetic field has been turned on. In both cases the displacement starts at zero but in the center of the phantom there is a negative displacement, indicating motion towards the magnet, located below the phantom. In-between the inserts, the motion is opposed to that in the NP-laden region. Note that there is a net displacement around which the oscillation takes place, at half the oscillation magnitude as predicted by theory. Note also the initial transient response before the oscillation reaches a steady state.

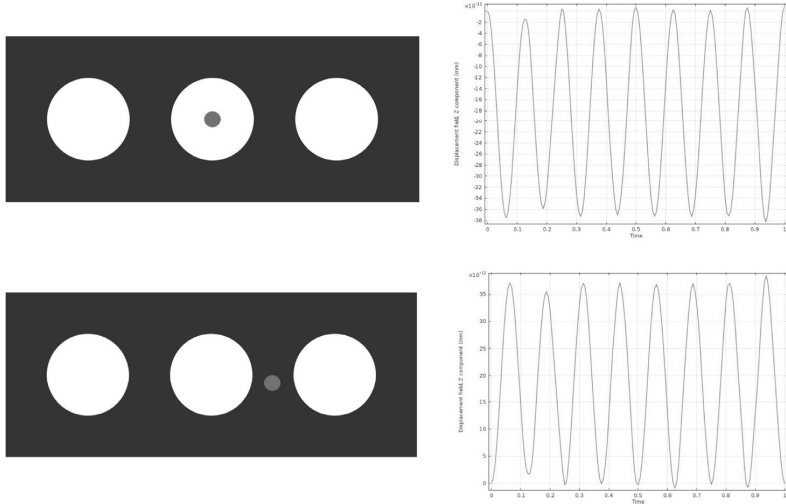


Figure 4. Material response at two points, in the center of the phantom (top row), and in-between the two rightmost inserts (bottom row). The left panels show the precise locations of the sample points (red dots), while the rightmost show the displacements at the corresponding points.

In Fig. 5, panel A shows the experimental MMUS image of approximately the central plane of the phantom, while panel B is the simulation (cut to show same field of view as panel A). The nanoparticle concentration expressed in mg Fe/ml, is indicated in panel A of Fig. 5, with insert concentrations of 0.4, 0.3, and 0.5 mg Fe/ml from left to right. These are also the concentrations chosen for the simulation (panels B and C, respectively, not indicated for clarity).

Color is scaled according to the absolute value of the vertical displacement (along the ultrasound beam). Movement in-between inserts can be seen, which after closer inspection was found to have opposite direction to that in nanoparticle regions. Note how the magnetomotive displacement in the central insert is the largest in both the experiment and the simulation, even though it holds the lowest nanoparticle concentration. This is a consequence of the shorter distance to the magnet, and therefore a higher spatial gradient, and thereby a larger acting force.

Panel C shows both displacement magnitude and direction as arrows, in a time instant of nearly maximum displacement. The black open triangle below the center insert indicates the position of the tip of the cone-shaped iron core. The position is the same also for panel A and B.

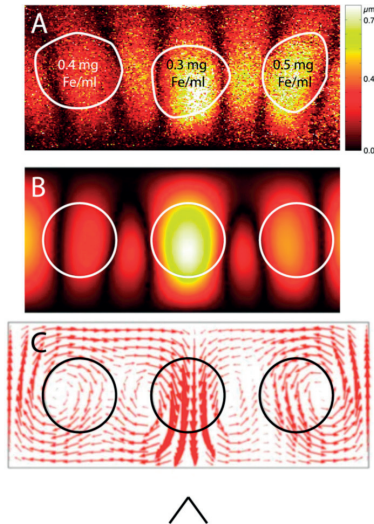


Figure 5. Detected magnetomotive motion in the experiment (A) and simulation (B and C). Color indicates displacement in the vertical direction, with a scale according to the color bar. In C the arrows show the direction of the displacement, where the size of the arrow indicate the magnitude of the displacement at the given location. The black open triangle below the center insert indicates the position of the iron core tip from which the magnetic field is extending.

The results from the *post mortem* case is shown in Fig. 6. Panel A shows displacement as arrows, at a time instant of nearly maximum displacement, at a cross-section through the centre of the simulated lymph node. In panel B, is the vertical displacement component shown as colour code. The lower panels are data from the experimental *post mortem* situation, the lymph node and its surrounding fat capsule is outlined. Panel C shows the phase of the detected signal as colour code. Note the area with coherent phase at the location of the lymph node. Adjacent to this region, within the fat capsule, the phase is also coherent but with opposite phase. Outside the lymph node area, the phase is apparently random, indicating no detectable magnetic force. Panel D shows a MMUS image. Pixels, only showing movement with the same frequency and phase (± 0.35 radians) as the magnetic field excitation signal, are accepted as nanoparticle movement. The color-code corresponds to MMUS displacement magnitude and when superimposed on the B-mode image indicates the presence of NPs.

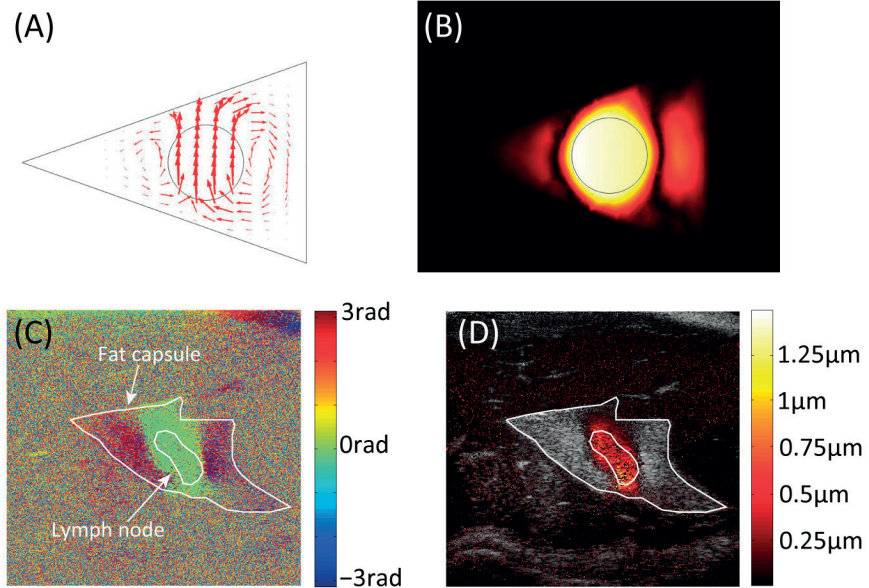


Figure 6. Detected magnetomotive motion in the simulation (A and B) and the experiment (C and D). The arrows in panel A show the direction of the displacement, where the size of the arrow indicate the magnitude of the displacement at the given location In panel B, color indicates displacement in the vertical direction, with white as maximum displacement. Displacement can be seen both in the lymph node and in the fat capsule. Panel C shows the phase distribution at the nanoparticle frequency overlaid as a color code on the ultraosund image. A MMUS image is shown in panel D. Only displacement with the same frequency and phase (± 0.35 radians) as the nanoparticle frequency is color coded according to the colorbar to the right. Both in panel A and C, a phase shift of approximately π radians can be seen between the SPION-laden lymph node and its closest surrounding can be seen.

4. Discussion

Due to the incompressible nature of the studied phantom media, it is natural that the application of a body load within a confined region in the material, would necessitate a displacement of this region. The displacement will be limited by the connective forces to the surrounding as well as viscous drag, while the connective forces mean that media surrounding the insert also would need to move. It is not intuitively clear how exactly the motion propagates in the phantom, even though a downward movement presumably should be compensated by an upward movement.

The simulation can answer this question by the trajectories in Fig. 5, panel C, that show how the movement propagates in the fixed-wall phantom. Consequently, the simulation appears to explain the observed opposed motion in-between the inserts as a result of mechanical coupling. This is assuming that the nanoparticles are fixed in the phantom material, and unable to migrate, at least during the time period of a cycle of the exciting magnetic field.

The tilt of the NP areas in Fig 5, panel A reflects attraction to the tip, while in panel B the tilt is away from the magnet. We interpret this to be due to the simulated slip condition at the boundary, which in reality presumably is a combination of slip and stick due to friction, causing the lateral forces to dominate. Another explanation may also be that the nanoparticle concentrations in the phantom do not match the ones modeled. It may also be due to geometrical inconsistencies, since the phantom material

is very soft, and difficult to precisely match the simulated geometry. Indeed, the inserts can be seen to not sit on an entirely straight line in Fig. 5, panel A, and not to describe perfectly circular regions. The shear and bulk moduli are furthermore only assumed, which is another uncertainty factor.

In the simulation the major upward motion appears to take place along the outer edges of the phantom, while in the experiment, more material is in opposite motion in-between the inserts. We believe this also can be explained as a result of a mismatch in geometry or nanoparticle concentrations, or as suggested above, the deviation in reality from the assumed slip boundary condition used in the simulations.

The simulation also shows a similar effect in the lymph node situation, with a counteracting movement adjacent to the nanoparticle-laden region, Fig. 6, panel A and B. This is consistent with what was found *post mortem*. Panel D shows the resulting MMUS image after rejecting out-of-phase motion. It is however visible in the phase image, panel C. The green area corresponds to a movement with zero radian phase shift relative the magnetic signal, while the adjacent red/blue area is phase shifted π radians. It is interesting to note that the movement in both simulation and *post mortem*, appears to be limited to the fat capsule surrounding the lymph node, reflecting the different mechanical properties of the fat and surrounding tissue.

The phase image in panel C also reveals that where there are no SPIO particles present, the phase is random and in panel D can be seen not to contribute to any measureable magnitude of magnetomotive motion. This would indicate that the diamagnetic effect is too small to be detected by our setup, and that the paramagnetic response from particles overrides this to a degree that allows detection.

In conclusion, the results points in the direction that the opposite-phase motion we have observed, in its magnitude can be explained as a coupled motion initiated from nanoparticle magnetomotion. The diamagnetic response was too small to be measured *post mortem*, but we still believe it to be of importance for the onset of magnetomotion, counteracting motion of small concentrations of nanoparticles.

5. References

- Bao G, Mitragotri S, and Tong S, 2013 Multifunctional nanoparticles for drug delivery and molecular imaging. *Annu Rev Biomed Eng*, **15**: p. 253-82.]
- Eghedari M A, Copland J A, Popov V L, Kotov N A, Motamedi M, and Oraevsky A A, 2003, Bioconjugated gold nanoparticles as a contrast agent for optoacoustic detection of small tumors, *Proc SPIE*, pp. 76-85.
- Evertsson M, Cinthio M, Fredriksson S, Olsson F, Persson H W, and Jansson T, 2013 Frequency- and Phase-Sensitive Magnetomotive Ultrasound Imaging of Superparamagnetic Iron Oxide Nanoparticles, *IEEE Trans. UFFC*, vol. 60, pp. 481-491.
- Evertsson M, Cinthio M, Fredriksson S, Kjellman P, in't Zandt R, Persson HW, Jansson T. 2014 Multimodal detection of iron oxide nanoparticles in rat lymph nodes using Magnetomotive ultrasound imaging and Magnetic Resonance Imaging, *IEEE Trans, Ultrason, Ferroelec, and Freq Contr*, vol 61, pp 1276-1283.
- Glozman T, and Azhari H. A Method for Characterization of Tissue Elastic Properties Combining Ultrasonic Computed Tomography With Elastography, *J Ultrasound Med*, vol 29:, pp 387-398, 2010.
- Jansson T, Andersson-Engels S, Fredriksson S, Ståhlberg F, Strand S-E. 2015 Superparamagnetic iron oxide nanoparticles as a multimodal contrast agent for up to five imaging modalities, *Clin Transl Imaging*, vol 3, pp 247-249.
- Lin C Y, and Pitt W G 2013 Acoustic droplet vaporization in biology and medicine, *Biomed Res Int*. 2013:404361, doi: 10.1155/2013/404361.
- Mehrnommadi M, Oh J, Mallidi S, and Emelianov S Y, 2011, Pulsed Magneto-motive Ultrasound Imaging Using Ultrasmall Magnetic Nanoprobes. *Mol Imaging*. Vol 10, pp. 102-110.

- Morse PM, Ingard KU. 1968, *Theoretical acoustics*. McGraw-Hill, New York.
- Oh J, Feldman M D, Kim J, Condit C, Emelianov S Y, and Milner T E, 2006 Detection of magnetic nanoparticles in tissue using magneto-motive ultrasound, *Nanotechnology* vol. 17: pp. 4183–4190,
- Oldenburg A L, Crecea V, Rinne S A, and Boppart S A, 2008 Phase-resolved magnetomotive OCT for imaging nanomolar concentrations of magnetic nanoparticles in tissues, *Opt. Express*, vol. 16, pp. 11525–11539.
- Zerda A, Zavaleta C, Keren S, Vaithilingam S, Bodapati S, Liu Z, Levi J, Ma T-J, Oralkan O, Cheng Z. et al, 2008, Photoacoustic molecular imaging in living mice utilizing targeted carbon nanotubes, *Nat Nanotech*, vol. 3, pp. 557–562.

Acknowledgments

The late Lennart Nilsson is acknowledged for skillfully manufacturing phantom molds, pinpoint iron cores, and other crucial sundries of relevance for this project. Financial support is acknowledged from the Kamprad Family Foundation and the Swedish Research Council.

Paper V

In vivo magnetomotive ultrasound imaging of rat lymph nodes – a pilot study

Maria Evertsson¹, Magnus Cinthio¹, Pontus Kjellman^{2,3}, Sarah Fredriksson², Roger Andersson¹,
Hanna Tofteval², Hans W. Persson¹, Tomas Jansson^{4,5}

¹Biomedical Engineering, Faculty of Engineering, Lund University, Lund, Sweden

²GeccoDots AB, Lund, Sweden

³Medical Radiation Physics, Clinical Sciences Lund, Lund University, Lund, Sweden

⁴Biomedical Engineering, Clinical Sciences Lund, Lund University, Lund, Sweden

⁵Medical Services, Skåne University Hospital, Lund, Sweden

Email: Maria.Evertsson@bme.lth.se

Abstract—The drive to gain a better understanding of how diseases arise and how to provide ever-earlier detection are some of the key factors for the development of molecular imaging. Compared to other imaging modalities ultrasound has not received the same attention for molecular imaging mainly due to its limited contrast resolution, together with contrast agents confined to the intravascular space. To overcome these issues, new nano-sized contrast agents and new ultrasound imaging techniques e.g. photo acoustic imaging, have been developed. Another such imaging technique under development is magnetomotive ultrasound imaging (MMUS). We have previously developed a frequency and phase tracking algorithm which is able to detect superparamagnetic iron oxide nanoparticles (SPIO NPs) using MMUS, where our suggested first clinical application is to detect sentinel lymph nodes (SLNs) in breast cancer surgery. Recently we have shown detection of SPIO laden rat SLNs *in situ*. Here we present the feasibility of *in vivo* detection of SLNs in rats. The algorithm clearly pinpoints the NP laden SLN, even in presence of significant artefactual tissue movement. The magnetomotive displacement increased when a higher voltage was applied on the coil creating the magnetic field (e.g. 56.6% increasing the voltage from 20V to 50V). An uneven concentration distribution of NPs in the SLN was found. The maximum magnetomotive displacement difference between two different cross sections in one SLN was 9.76 times. The study also showed that for a higher concentration of NPs a lower magnetic coil excitation voltage could be used in order to create a magnetomotive displacement of a certain magnitude. The result from this *in vivo* study shows that the method has potential for future clinical use.

Keywords-Magnetomotive ultrasound imaging; molecular imaging sentinel lymph nodes; *in vivo* imaging; contrast agents; multimodal imaging

I. INTRODUCTION

Molecular imaging has through the last decades gained an increasing focus in the medical imaging community. The possibility to detect changes and abnormalities on a cellular or molecular level is expected to open up the feasibility of earlier detection of diseases, better understanding how diseases arise, an individualized treatment, and a more precise follow up [1].

This study was supported by grants from the Kamprad Family Foundation, VINNOVA, The Swedish Research Council, The Knut and Alice Wallenberg foundation, The Royal Physiographic Society in Lund and The IEEE UFFC society

Ultrasound, being a cost effective, non-radiating imaging technique with a wide accessibility should be a well-considered choice in many imaging applications. But due to its limited contrast resolution conventional ultrasound cannot be used to image molecular events directly, and commercial contrast agents also limit applicability to intravascular events. In an effort to overcome these limitations, different contrast agents and alternative imaging approaches have been developed [2].

In 2006 magnetomotive ultrasound (MMUS) imaging was introduced by Oh et al. The main idea is to apply a time varying magnetic field to a volume where superparamagnetic iron oxide nanoparticles (SPIO-NPs) are deposited. The magnetic nanoparticles will thereby start to move in response to the field, and an induced movement of their surrounding will follow. This movement is possible to detect with conventional ultrasound [3]. Due to their small size, the particles are small enough to be used for molecular imaging of extravascular events.

We have previously developed a motion artefact robust algorithm which is able to detect this movement [4] and most recently we have proven it to successfully image SPIO-laden sentinel lymph nodes (SLN) in rats *in situ* [5]. The SLN is the first lymph node which drains a primary tumor region, and it is of special therapeutic interest, particularly in cases of breast cancer and malignant melanoma. Since one of the main routes for cancer spread is via the lymphatic system, tumor infiltration in the SLN means a higher probability for further metastatic spread, and therefore the need to locate and examine the SLN. In the same study we also showed a multimodal capability of the particles, as the same NP-laden SLNs were detected with both MRI and MMUS. Still, it is uncertain whether it is possible to use MMUS *in vivo* which is fundamental for future clinical use.

In this paper we have studied NP-laden SLNs in rats *in vivo*. Our aim was to find whether it was possible to filter out the nanoparticle displacement and suppress unwanted motion artefacts as e.g. heart beats and respiration. Further, to evaluate our results, we have also investigated how the magnetic field excitation voltage affect the nanoparticle

movement, calculated signal-to-clutter ratios and observed how the particles are distributed within the SLN.

II. MATERIAL AND METHODS

A. Nanoparticles

The superparamagnetic iron oxide nanoparticles (SPIO NPs) (GeccoDots AB, Lund, Sweden) used in this study consisted of a Fe_3O_4 iron core coated with polyethylene glycol (PEG) to make the particles biocompatible and to prevent aggregation. The SPIOs iron core size were $10 \pm 2\text{ nm}$ and measured by dynamic light scattering the particles hydrodynamic diameter were $40 \pm 5\text{ nm}$. The magnetic saturation was 80 electromagnetic units/g Fe_3O_4 .

B. In vivo study

Three 6-weeks-old female Wistar rats were injected subcutaneously on the dorsal side of their right hind paw with 0.1 mL SPIO NP solution. The injections were given in three different concentrations; 0.1, 0.2, 0.3 mg iron oxide/ml, one for each animal. 24 hours post injection the animals were anaesthetized with isoflurane and the popliteal lymph node (SLN), proximal to the injection site was scanned with the MMUS setup. All studies were performed in compliance with the Swedish regulations for the conduct of laboratory animals.

C. Experimental setup

For each animal the location of the SLN was positioned between a transducer, MS550D (25–35 MHz bandwidth, center frequency 32 MHz; VisualSonics Inc., Toronto, ON, Canada), and a solenoid with an iron-core (in-house design) producing a time varying magnetic field. A 5 Hz AC-voltage was applied on the solenoid and varied between 5–60 V, in steps of 5 V. A function generator produced the electric signal which was subsequently fed to a power amplifier (in-house design) to generate sufficient magnetic field strength. The magnetic flux density measured at 60 V, 7 mm above the iron core of the solenoid using a hallsensor was 0.28 mT. Using the Visualsonics Vevo 2100 research interface the radio frequency in-phase quadrature (RF-IQ) data could be collected. The data was then exported to Matlab (The MathWorks Inc., Natick,

MA), where our algorithm was implemented, and processed offline.

D. Evaluation

The magnetomotive displacement in the lymph node, i.e. the displacement at the precise frequency and phase (± 0.35 radians) of the NPs, was calculated using our previously developed algorithm [4]. For each animal this was done for all voltages (5–60 V, in steps of 5 V) and for six different cross sections. The cross sections were obtained at 60 V, 5 Hz and three of the planes were taken along the longitudinal axis (the longest dimension) of the SLN, and three planes orthogonal to those. The lymph node in which the magnetomotive displacement was calculated, was outlined in the B-mode image. The total movement, i.e. displacement at all frequencies was also calculated. Finally Signal-to-Clutter-Ratios (SCR), defined as magnetomotive displacement magnitude in all the pixels in the SLN divided by that in the rest of the pixels in the ultrasound image, were calculated.

III. RESULTS

The SPIO-NP laden sentinel lymph nodes in all three rats were successfully imaged using our MMUS frequency and phase-gated algorithm.

The SLN and its surrounding fat capsule in the right knee of animal 3 is imaged in Fig. 1. The solenoid excitation was 35 V, 5Hz. Panel 1A shows a B-mode image where the SLN is outlined. Panel 1B shows the total movement in the ultrasound image at the entire frequency range (0–25 Hz, framerate 50 Hz) and at all phases ($-\pi - \pi$). The color coding represents displacement. Panel 1C is obtained by employing our algorithm, the MMUS image shows only the pixels moving with the same frequency and phase (± 0.35 radians) as the NPs. The magnetomotive displacement is superimposed as color code on the B-mode image. Note that the difference of the maximum displacement is more than 150 times larger for panel 1B than 1C and observe the bright area to the left of the SLN in panel 1B, stemming from pulsatile motion of the popliteal artery. As the heart rate of the animal is approximately 7 Hz, this signal is effectively suppressed. The SCR in panel 1C was 23.3 dB.

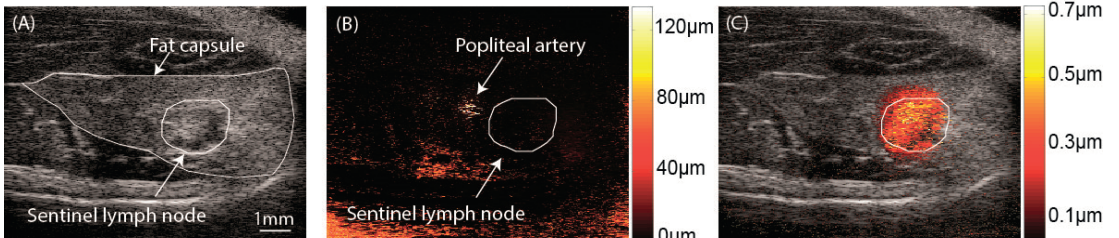


Fig. 1. The SLN in rat 3 injected with 0.3 mg Fe/ml when the magnetic field excitation voltage was 5 Hz 35 V. (A) A B-mode image where the SLN is outlined. (B) The total movement, i.e. movement at all frequencies and phases is superimposed as a color code on the B-mode image. The white area to the left of the SLN is the popliteal artery. (C) A MMUS image of the SLN. Pixels moving with the same frequency and phase as the NPs are color coded according to displacement. Note the scales, the maximum displacement is more than 150 times larger in panel B than panel C. The SCR in panel C was 23.3 dB.

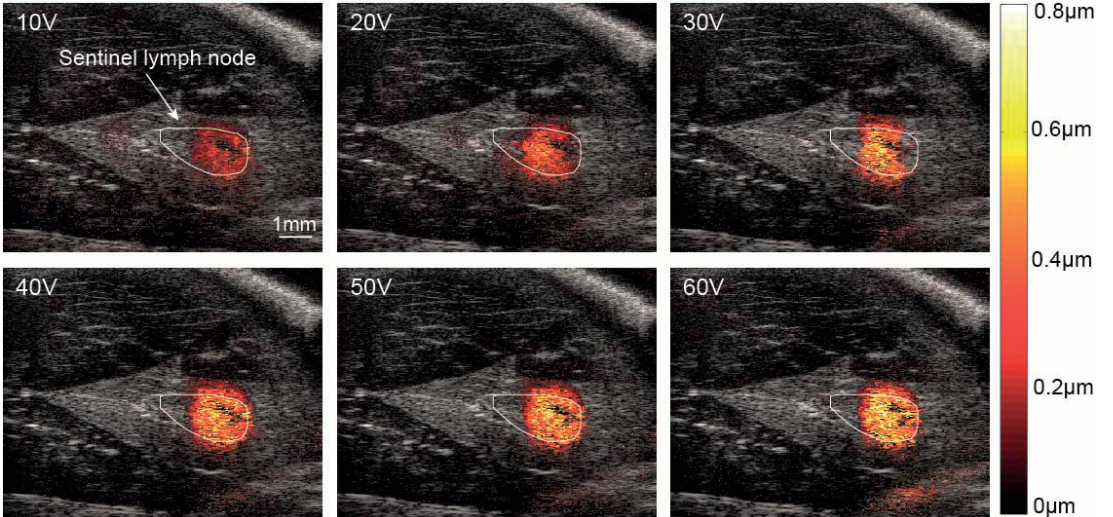


Fig. 2. MMUS images of the SLN in rat 2, injected with 0.2 mg Fe/ml, obtained at six different excitation voltages: 10, 20, 30, 40, 50 and 60V. To give the ability to compare the magnetomotive displacement at different voltages, the color scale is identical for all images with the brightest color corresponding to a displacement magnitude of 0.8 μm . All pixels showing larger displacements were set to 0.8 μm . It can be seen from the images that the MMUS signal increases with a higher magnetic field voltage.

Fig. 2 shows a series of MMUS-images for animal 2. The images show the resulting magnetomotion with magnetic field excitation voltages ranging between 10-60 V in 10 V increments. The color scale is equal for all images to aid comparison between images. The color bar was adjusted to accommodate displacements up to 0.8 μm , while pixels showing a larger displacement were set to 0.8 μm (white). As expected and seen previously, higher voltages resulted in larger magnetomotive displacement [4, 5].

In Fig. 3 the excitation voltage is plotted versus the mean magnetomotive displacement in the SLNs for the three

animals. Also this graph follows the same pattern as Fig. 2; a higher voltage induces a larger displacement. The mean (\pm standard deviation) magnetomotive displacements for the three animals (conc. 0.1, 0.2 and 0.3 mg Fe/ml) were $0.10 \pm 0.16 \mu\text{m}$, $0.18 \pm 0.19 \mu\text{m}$ and $0.17 \pm 0.16 \mu\text{m}$ respectively.

The mean SLN magnetomotive displacement in the six different cross sections obtained in each animal is plotted in Fig. 4. The solenoid excitation was 5 Hz 60 V. It can be seen that it varies not only between the different subjects but also among the different cross sections in each lymph node. The mean (\pm standard deviation) magnetomotive displacements for the animals were $0.07 \pm 0.14 \mu\text{m}$ for animal 1 (0.1 mg Fe/ml), $0.25 \pm 0.23 \mu\text{m}$ for animal 2 (0.2 mg Fe/ml) and $0.18 \pm 0.20 \mu\text{m}$ for animal 3 (0.3 mg Fe/ml). Note that some of the cross sections show more or less no magnetomotive displacement. The ratios between the cross sections with the maximum and minimum magnetomotive displacement were calculated to 6.87, 2.12 and 9.76 for animal 1, 2 and 3, respectively.

Fig. 5 shows a graph of SCR versus excitation voltage for all three animals. The SCR increases with voltage up to 20-30 V where it stabilizes. The mean SCRs for the three rats were $15.54 \pm 5.21 \text{ dB}$ for animal 1, $17.35 \pm 6.89 \text{ dB}$ for animal 2 and $16.78 \pm 6.24 \text{ dB}$ for animal 3.

IV. DISCUSSION

In this *in vivo* study we have shown that it is feasible to detect SPIO NP-laden sentinel lymph nodes in Wistar rats using our frequency and phase sensitive MMUS-algorithm. The algorithm's ability to pick up the magnetomotive displacement enables detection of NP displacement on a sub micrometer level and motion artefacts from e.g. blood flow, which is order of magnitudes larger, can effectively be filtered

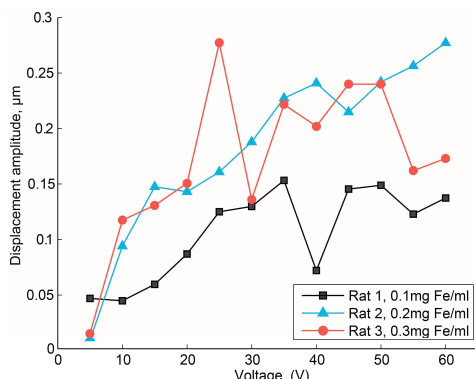


Fig. 3. The mean nanoparticle displacement magnitude in the outlined SLN area for the three rats as a function of applied magnetic field excitation voltage. A higher voltage results in a larger displacement magnitude. The graph indicates that if the concentration of NPs is increased, a lower excitation voltage is needed to get the same displacement magnitude.

out (see Fig 1). When the magnetomotive displacement is superimposed as a color code on the B-mode image the algorithm clearly pinpoints location of NPs.

As in previous reports [4, 5] a positive relationship between an increased magnetic field excitation voltage and a larger magnetomotive displacement can be seen. The result of this is illustrated in both in Fig. 2 and Fig. 3 Some measurement values e.g. animal 1 at 40 V and animal 3 at 25 V differs substantially from measurements at adjacent voltages. With the limited amount of data in this pilot study we cannot find any obvious explanation for this. Perhaps it may be a consequence of some resonance or interference phenomenon of the various tissue motions within the rat/lymph node [6].

An increase in MMUS signal was also expected for higher NP concentrations. Here animal 2, injected with the medium concentration of NPs, had a slightly larger mean displacement than the high concentration animal 3. This indicates an inter-subject variation in SPIO-NP uptake in the SLN and/or an uneven distribution of the NPs throughout the SLN, which has also previously been reported by Kjellman et al [7]. The varied mean magnetomotive displacement within the different cross sections in the same SLN similarly points to an uneven NP distribution within the SLN.

When comparing the ratios between the cross sections with the maximum and minimum magnetomotive displacement within each SLN, animal 3 had the highest ratio. It was 1.4 times larger than animal 1 and 4.6 larger than animal 2. This shows that animal 3 probably had the most heterogeneous distribution of NPs throughout the SLN.

The SCR increases with voltage but beyond 20-30 V the SCR stabilizes (Fig. 5). One explanation for this could be that 20-30 V may be the threshold value where all NPs are set in detectable motion. An even higher excitation voltage would only increase the magnetomotive displacement magnitude, both in and outside the SLN as the NP displacement propagates from the SLN into the surrounding tissue (see Fig. 2). The stabilization of the SCR would be a result of an equal contribution of increased displacement in and outside the SLN.

The large SCRs values show that the algorithm is able to differentiate the NP-laden SLNs from their surrounding which

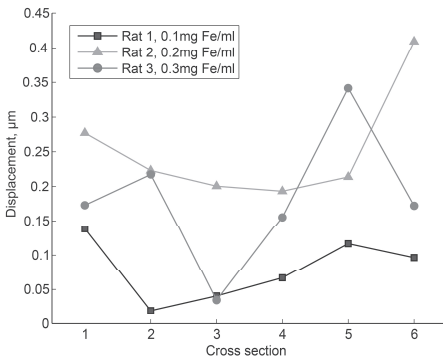


Fig. 4. The mean magnetomotive displacement magnitude in the SLN in six different cross sections in each of the rats. The cross sections were obtained at 5 Hz 60 V. The displacement tends to vary within the SLN, indicating an uneven distribution of NPs in the SLN.

is crucial for the technique to make clinical translation. There are still many practical issues to obtain a better understanding how different parameters affect the displacement and detection SPIO NPs in the SLN. Additional measurements of for instance the NPs distribution within the SLNs have to be performed.

V. CONCLUSION

In this study we have shown that it is possible to detect magnetomotive nanoparticle induced displacement *in vivo* in rat sentinel lymph nodes. Though the magnetomotive displacement is small and the motion artefacts from the heart and blood flow are substantial larger, our algorithm is able to extract the magnetomotive displacement and provide a clear representation were the SPIO NP laden sentinel lymph nodes are. This opens up the ability for future use of this technique to detect sentinel lymph nodes in the clinic.

REFERENCES

- [1] R. Weissleder, "Molecular imaging in cancer," *Science*, vol. 312, no. 5777, pp. 1168–1171, 2006.
- [2] M. Mehrmohammadi, J. Oh, L. Ma, E. Yantsen, T. Larson, S. Mallidi, S. Park, K. P. Johnston, K. Sokolov, T. Milner, and S. Emelianov, "Imaging of iron oxide nanoparticles using magneto-motive ultrasound," in Proc. IEEE Ultrasonics Symp., pp. 652–655, 2007.
- [3] J. Oh, M. D. Feldman, J. Kim, C. Condit, S. Y. Emelianov, and T. E. Milner, "Detection of magnetic nanoparticles in tissue using magnetomotive ultrasound," *Nanotechnology*, vol. 17, pp. 4183–4190, 2006
- [4] M. Evertsson, M. Cinthio, S. Fredriksson, F. Olsson, H. W. Persson, and T. Jansson, "Frequency- and Phase-Sensitive Magnetomotive Ultrasound Imaging of Superparamagnetic Iron Oxide Nanoparticles," *IEEE Trans. UFFC*, vol 60, pp 481-491, 2013.
- [5] M. Evertsson, P. Kjellman, M. Cinthio, S. Fredriksson, R. in 't Zandt, H. W. Persson, and T. Jansson, "Multimodal Detection of Iron Oxide Nanoparticles in Rat Lymph Nodes Using Magnetomotive Ultrasound Imaging and Magnetic Resonance Imaging" *IEEE Trans UFFC*, vol 61, 1276-1283, 2014
- [6] T. Jansson, M. Evertsson, E. Atilé, R. Andersson, S. Fredriksson, H. W. Persson, I. Svensson, M. Cinthio, "Induced tissue displacement in magnetomotive ultrasound imaging - simulations and experiments", in Proc. IEEE Ultrasonics Symp., pp 639-642, 2014.
- [7] P. Kjellman, R. in 't Zandt, S. Fredriksson, SE. Strand, "Optimizing retention of multimodal imaging nanostructures in sentinel lymph nodes by nanoscale size tailoring." *Nanomedicine*, 2014 Jul; vol 10, 1089-1095

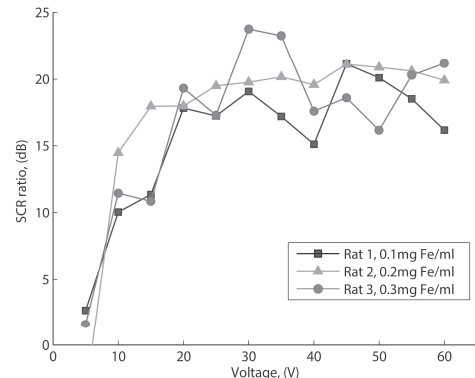


Fig. 5. The signal-to-clutter ratios for the three rats at different voltages. The SCR increases with voltage but for voltages exceeding 20-30 V the SCR stabilizes.

Paper VI

***In vivo* detection of ^{68}Ga -labelled superparamagnetic iron oxide in rat sentinel lymph nodes using PET/CT, Magnetomotive ultrasound and MRI**

Maria Evertsson¹, Pontus Kjellman², Magnus Cinthio¹, Roger Andersson^{1,3}, Thuy A Tran⁴, Rene in't Zandt⁴, Gustav Grafström⁴, Hanna Toffevall⁵, Sarah Fredriksson⁵, Christian Ingvar⁶, Sven-Erik Strand^{2,4}, Tomas Jansson^{3,7}

¹Biomedical Engineering, Faculty of Engineering LTH at Lund University, Lund, Sweden

²Medical Radiation Physics, Clinical Sciences Lund, Lund University, Lund Sweden

³Medical Services, Skåne University Hospital, Lund, Sweden

⁴Lund University Bioimaging Center, Lund University, Lund, Sweden

⁵Genovis AB, Lund, Sweden

⁶Department of Surgery, Skåne University Hospital, Lund Sweden

⁷Clinical Sciences Lund, Biomedical Engineering, Lund University, Lund, Sweden

Address correspondence to: Maria Evertsson, Biomedical Engineering, Faculty of Engineering, LTH, Lund University PO Box 118, 22100 Lund, Sweden

Phone: +46 46 222 76 91, E-mail: maria.evertsson@bme.lth.se

Keywords: Multimodal imaging, magnetomotive ultrasound, ^{68}Ga -labeled superparamagnetic iron oxide nanoparticles (SPIONs), PET/CT, sentinel lymph node

Abstract

Combining whole body SPECT/PET imaging with high resolution imaging techniques (multimodality imaging - MMI) would enhance lesion detectability. Magnetomotive ultrasound (MMUS) imaging is a new ultrasound technique, which enables *in vivo* detection of superparamagnetic iron oxide nanoparticles (SPIONs) with high spatial resolution (down to 50 microns). In MMUS, an external time-varying magnetic field is employed to induce movement in SPION-containing tissue, and the resulting tissue movement can be detected with ultrasound. Herein we present a MMI study where we have used this novel imaging technique in combination with PET/CT and MRI. To demonstrate the technique *in vivo*, we used a multimodal contrast agent consisting of ^{68}Ga -labeled SPIONs in a sentinel lymph node (SLN) rat model. The model is based on a clinical scenario; one hour post injection of ^{68}Ga -SPIONs, the animals were imaged with combined PET/CT. After two to four days, the same animals were imaged with MMUS. In addition, MRI was used to evaluate the amount of particles in each SLN. All SLNs were detectable in the PET images. The MMUS and MRI measurements were in close agreement. Four of six SLNs could be detected with MMUS. The MRI measurements revealed that the two lymph nodes undetectable with MMUS contained the lowest concentrations of particles. This study shows that MMUS can be a complementary imaging modality to standard methods providing high resolution and late imaging. By combining these three imaging modalities, we envisage that an improved identification and localization of for example SLN can be achieved but also that other applications of targeted SPIONs for a variety of malignancies may emerge.

1. Introduction

Non-invasive imaging for cancer staging is today conducted using nuclear imaging methods such as single-photon emission computed tomography (SPECT) and positron emission tomography (PET), both sensitive methods that provide whole body imaging with a spatial resolution of 5-10 mm. Localization and quantification of activity distribution can be achieved, but the two modalities visualize function and not anatomy. For anatomical imaging with high spatial resolution, computed tomography (CT), magnetic resonance imaging (MRI) and ultrasound (US) are used. Hybrid systems such as PET/CT and PET/MRI have been developed and are today in clinical routine [1-3]. By incorporating high-resolution ultrasound imaging as bedside surgical guidance, preferably after the decay of the radioactivity used, additional

benefits, such as reduced exposure to health care personnel, will be achieved. One possible approach to implement this type of multimodality imaging, is to use contrast agents based on nanoparticles [4].

Superparamagnetic iron oxide nanoparticles (SPIONs) is one example that has been used as MRI contrast agents for nearly two decades [5, 6]. By labeling the particles with radionuclides, detection with PET and SPECT is possible [1, 2, 7, 8].

Ultrasound is the most commonly used imaging technique in today's health care. The technique possess several advantages as being cost effective, non-invasive, nonionizing, portable and it provides real-time images with anatomical and physiological information. Imaging of nanoparticles with conventional ultrasound is not possible since nanoparticles are too small to backscatter ultrasound at a detectable level. To overcome this limitation, new ultrasound techniques, which indirectly image the nanoparticles, have been developed. One such new technique is magnetomotive ultrasound (MMUS) imaging, which enables detection of SPIONs *in vivo*. In MMUS, SPIONs are set in motion with an external time varying magnetic field. In turn, the tissue associated with the nanoparticles will be set in motion, and this movement can be detected with ultrasound [5, 9, 10]. The MMUS technique has potential for numerous applications in the medical imaging field by e.g. enabling real time images of molecular events [9]. One benefit would also be to enable late imaging of suspected tissues after SPECT/PET whole body malignancy detection, thus omitting radiation exposure at e.g. surgical procedures.

One such application, where we believe MMUS will be beneficial, is in sentinel lymph node (SLN) detection, providing high-resolution bedside surgical guidance during SLN surgery. The SLN is the first lymph node receiving lymphatic drainage from a primary tumor and it is therefore the first place tumor cells infiltrate when metastasizing [11-13]. By examining the SLN for the presence of metastatic cells, it can be determined whether the cancer has disseminated.

In this study, we suggest a clinical scenario where PET, MRI and MMUS are combined using ⁶⁸Ga-labeled SPIONs as a multimodal contrast agent. High sensitive and quantitative PET imaging together with high resolution anatomical MRI could be performed for pre-operative staging and then, as an intraoperative guide, MMUS could be used to visualize the SLN profiting on the very same particles for contrast. Since the retention time of the SPIONs in the SLN is long, together with the fact that the MMUS signal is only dependent on the concentration of the SPIONs, intraoperative SLN detection can be performed several days after nanoparticle administration, when the radioactivity has decayed. The blue dye, currently in clinical use to guide the surgeon at SLN resection, can thereby be excluded and replaced by MMUS, consequently omitting the risk of allergic complications associated with the dye [14]. Because of the rather rapid uptake of SPIONs in the SLN, a radionuclide with a relatively short half-life can be used, resulting in a low absorbed dose to the patient and omitting radiation exposure to the surgical staff. Thus, our suggested technology shift has the potential for more rational handling of SLN resection.

The present animal study was designed to test this hypothetical clinical scenario of multimodal imaging where PET/CT images were acquired one hour after nanoparticle injection followed by MMUS imaging either two or four days later. In this experiment, the MRI was used to evaluate the presence of SPIONs in the SLN.

2. Material and methods

2.1 Nanoparticles

The superparamagnetic nanoparticles used in this study were obtained from Genovis AB, Lund, Sweden. The nanoparticles consisted of a Fe₃O₄ core with a diameter of 10 ± 2 nm and were coated with polyethylene glycol (PEG) to make the particles biocompatible and to prevent aggregation. Their hydrodynamic diameter was determined to 40 ± 5 nm with dynamic light scattering (Malvern Zeta Sizer Nano Series, Malvern Instruments Ltd, Worcestershire, UK).

⁶⁸Ga (T1/2=67.7 min, β+=89% and EC=11%) was eluted from a ⁶⁸Ga/⁶⁸Ge-generator system (IDB, Holland) with 6 mL of 0.6 M hydrochloric acid in 0.3-0.5 mL fractions. Fractions containing 40-80 MBq of ⁶⁸GaCl₃ were used for labeling.

The pH of the ⁶⁸GaCl₃ eluate was adjusted with 5-6 µL 5 M NaOH and 100-200 µL 0.25 M sodium acetate to pH 5.5 before the nanoparticles were added to the radionuclide solution. The reaction mixture was incubated in a heating box under gentle shaking conditions at 50°C for 25-30 min.

The labeled ⁶⁸Ga-SPIONs were separated from free ⁶⁸Ga using a column containing ferromagnetic spheres (Miltenyi Biotech, Germany). Attaching a magnet to the column and filtering the reaction mixture, the ⁶⁸Ga-SPIONs were trapped within the column while the free ⁶⁸Ga and buffer solution flow through. The magnet was removed and the ⁶⁸Ga-SPIONs were eluted with saline. The labeling efficiency was approximately 75-92%.

To ensure an equal injected activity between animals, with respect to radioactive decay and injection volume, SPIONs were labeled in four batches.

The activity of the injections was kept as constant as possible (4.4-8.0 MBq), which lead to a variation in nanoparticle concentration (1-4 mg Fe/ml).

2.2 Animals

Six 6-weeks-old female Wistar rats were subcutaneously injected with 0.1 mL ⁶⁸Ga-SPION solution in the right hind paw while under isoflurane anesthesia. After injection, the anesthesia was removed and the animals were allowed to wake up and move around for one hour before a PET/CT scan was performed.

The study was made in compliance with local and national regulations approved by the Local Ethics Committee for Animal Research, Lund, Sweden.

2.3 PET/CT imaging

One hour post injection, each animal was anesthetized with isoflurane and placed on an animal bed (Minerve, Bioscan, USA). The animal was thereafter imaged with a dual-modality PET/CT system (NanoPET/CT, Bioscan, USA). The injected paw was placed in a lead cylinder during the measurements to shield the injection site from adding too much background counts in the lymph node image. A five minutes CT scan was performed, followed by a PET scan where three images were collected in 15 min intervals for 45 minutes. After the measurements, the animals were returned to their cages.

Reconstruction of images was performed using an ordered subset expectation maximum (OSEM) iterative method with the following parameters: energy window 400-600 keV, single

slice rebinning to 2D LOR, ring difference 16 and coincidence 1-3. Morphological information was provided by CT images acquired with 55 kV_{peak}, 360 projections, medium or maximum zoom and reconstructed with RamLack filter. The PET and CT images were exported to VivoQuant (inviCRO, Boston, USA) for co-registration and analysis.

The SLN in each animal was delineated in the PET images and activity calculations of the ⁶⁸Ga-labeled SPIONs present were performed using a standard sample of ⁶⁸Ga activity measured in the same geometry as the rat. In the contralateral leg, a volume of the same size as the one in the injected leg was delineated at the lymph node position and the same calculations were performed.

2.4 MMUS imaging

The animals were divided into two groups with three individuals in each and MMUS imaging was performed either two or four days after nanoparticle administration, respectively. The imaging was performed with a high frequency ultrasound scanner; VisualSonics Vevo 2100 (VisualSonics Inc., Toronto, ON, Canada). The entire MMUS setup is illustrated in Fig. 1. Each animal was anesthetized with isoflurane and its right knee was positioned between the ultrasound transducer (MS550D, 25 to 35 MHz bandwidth, center frequency 32 MHz) and an iron core surrounded by an electromagnet (in-house design). An electrical signal, produced by a function generator (HP 33120, Agilent Technologies Inc., Santa Clara, CA) was used to switch a power source at a frequency of 5 Hz. The voltage setting on the power source was varied between 10-60 V in steps of 10 V to produce six magnitudes of the magnetic field after application to the electromagnet. At each power level, three different cross sections were obtained for each animal, except from animal 5 where only two cross sections were collected due to a technical problem. The signal generated by the function generator, i.e. the reference signal, was fed into the ultrasound system via the ECG-input, enabling a synchronized measurement acquisition. For each measurement, ultrasound data was collected for 3 seconds at a recording rate of 50 frames per second. The ultrasound data was exported to Matlab (The MathWorks Inc., Natick, MA) where it was post-processed with our own in-house developed MMUS algorithm [15].

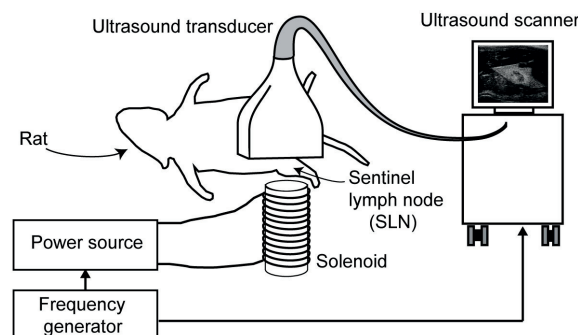


Figure 1. MMUS experimental setup. The animal is placed over the solenoid iron core and a time-varying magnetic field is applied. The nanoparticles will thereby be set in motion and thus, their surrounding tissue. A high frequency ultrasound scanner registers the movement and after post signal processing of the ultrasound data, the MMUS signal is obtained.

2.5 Frequency and phase tracking MMUS algorithm

The purpose of the algorithm is to isolate the MMUS signal from motion artifacts caused by e.g. heartbeats and respiration, which have a much larger magnitude. Since the particles move in compliance with the magnetic field, motion at 5 Hz is what the algorithm tracks in the ultrasound speckle echoes over time. All other frequencies will be suppressed and filtered out. A discrimination with regard to the phase of the nanoparticles is also performed, where only pixels showing movement with the same phase (± 0.35 radians) as the phase of the excitation signal are accepted as nanoparticle movement. For a more detailed description of the algorithm, see reference [15].

The popliteal lymph nodes are situated in the knee inside a fat capsule. At higher excitation voltages, the generated magnetomotion can be observed outside the SLN in the surrounding fatty tissue [15]. We have chosen to include all of this motion in evaluation of the MMUS displacement signal. In a previous study [16] we showed that magnetomotion propagates from the area containing SPIONs, but here it could also be a result of magnetomotion generated outside the imaging plane. In either case, the detected magnetomotion reflects the total deposited energy, which motivates us to include also magnetomotion appearing vertically inside the fat capsule. Thus, the SLN as well as the area of the fat capsule extending above and below the SLN was outlined in the B-mode grayscale image, as shown in Fig 4. For each pixel in the outlined area, the magnetomotive movement, i.e. the movement at the precise frequency and phase (± 0.35 radians) as the nanoparticles, was calculated using our algorithm. To obtain a value to represent the magnetomotive movement in each lymph node, the average magnetomotive movement of all pixels in the outlined area was calculated. Finally, to obtain a value to represent the magnetomotive movement in each animal, the average magnetomotive movement of all cross-sections (3 per SLN) and at all voltages (6 per cross section, 10-60V in steps of 10) in that specific animal was calculated. Thus the presented value of the magnetomotive movement, for each animal, was obtained from 18 individual images of that animal (except from animal 5 where only two cross section were collected).

After the MMUS examination, the animals were sacrificed by an overdose of isoflurane. Thereafter the SLN and the popliteal lymph node from the contralateral side were harvested together with their surrounding tissue for further MR analysis.

2.6 MR imaging

An 11.7 T vertical wide bore MR scanner (Agilent Technologies) was used to image the excised lymph nodes using a micro-imaging RF coil (13 mm diameter, Neos Biotech, Spain). For all six animals both the SLN and control lymph node, still encapsulated in some of the surrounding tissue (muscle and fat), were put in an Eppendorf tube, which was placed inside the MRI scanner. T2*-weighted MR-images were acquired (3D gradient echo, TE 1.48 ms, TR 15 ms, field of view: $20 \times 10 \times 10$ mm, pixel resolution after zero filling: $39 \times 39 \times 39$ μm , 4 averages, 16 min scan time.).

The 3D dataset containing 256 MR images of 512×256 voxels was exported to ImageJ [17]. To evaluate the MRI images, the hypointense MRI signal i.e. the lack of signal inside the lymphatic tissue, represented as black in the MR images, was calculated. An assumption was made that the number of black pixels in the hypoenhancement was proportional to the amount of SPIONs, which in turn affects the MRI signal. The cross section with the highest effect on the MR-signal

was located in the 3D volume and an image of this cross section was saved. The black pixels in the SLN, and sometimes also in its closest surrounding (depending on signal extent), were filled in Adobe Photoshop (Adobe systems) using the Magic wand tool. The number of selected pixels was thereafter calculated using a Matlab script.

3. Results

3.1 PET/CT imaging

With combined PET/CT, ^{68}Ga -labeled SPIONs were successfully detected in all six animals. As an example, a coronal PET/CT image of animal 1 is shown in Fig. 2A. The center of the red cross displays the position of the popliteal lymph node (SLN). An accumulation of ^{68}Ga -labeled SPIONs can be seen in the SLN, as well as in the second and third lymph nodes (iliac). A similar accumulation of nanoparticles was found in all six animals. The lead cylinder, in which the animal's injected paw was placed, is visualized to the bottom right in the image.

MMUS signal was detectable in four of the six animals. Fig. 2B shows a MMUS image of the SLN in the same animal as in Fig. 2A. The high-resolution MMUS image corresponds to the area outlined with a white rectangle in the PET/CT image and the fat capsule, surrounding the SLN, is outlined in the image. The nanoparticles, accumulated in the SLN, induces a magnetomotive displacement in the SLN and its surroundings. A color-coding in regard with this displacement calculated is done, displaying the location of the SLN.

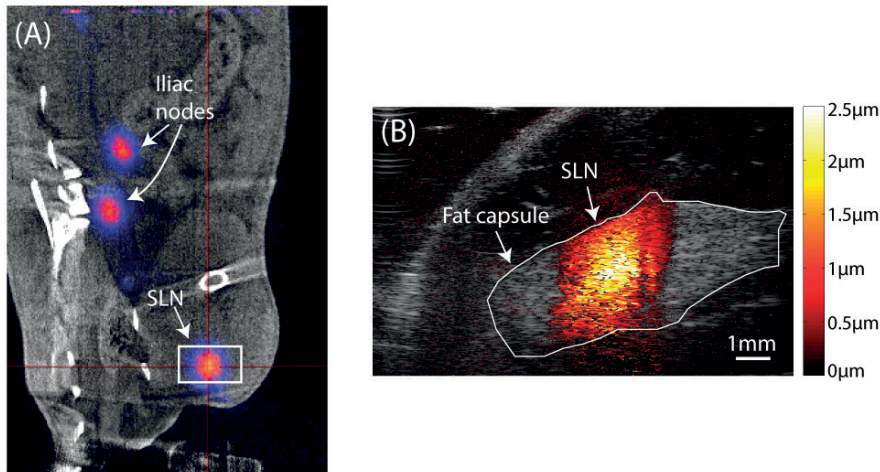


Figure 2. Panel (A), coronal PET/CT image of animal 1. The center of the red cross shows the position of the SPION-accumulated SLN. SPION accumulation is also seen in two iliac lymph nodes. The lead cylinder shielding the injected paw is shown to the bottom right in the image. Panel (B), MMUS image of the SLN in animal 1. The image is a magnification of the area outlined with a white rectangle in the PET/CT image. The fat capsule surrounding the lymph node is outlined in the image and the induced magnetomotive displacement, shown as a color-code in the image, reveals the location of the SLN.

The percent injected activity (%IA) in the SLNs, determined from the 45 minute PET scan, is plotted in Fig. 3. The mean %IA (\pm standard deviation) in all SLNs was $2.6 \pm 2.9\%$, whereas the mean %IA in the contralateral lymph node was $0.1 \pm 0.05\%$, which was considered background. For all animals, there was a much higher activity in the SLN compared to the control lymph node.

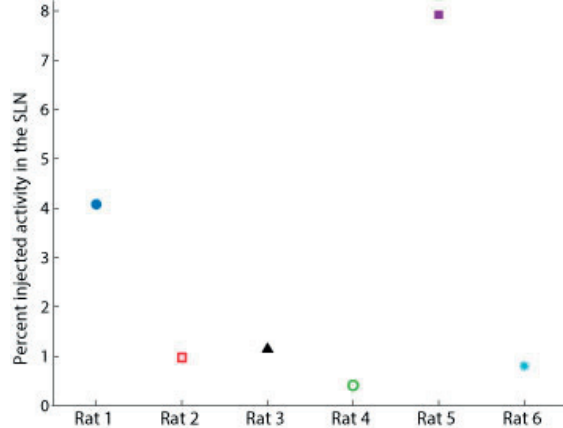


Figure 3. The graph shows the percent injected activity in the SLN for all six animals.

3.2 MMUS imaging

A typical MMUS sequence is shown in Fig 4. Panel A shows a B-mode image of a sentinel lymph node and its surrounding fat capsule. The lymph node, the area in which the MMUS displacement is calculated in this study, and the fat capsule are outlined in the image as yellow, green and white respectively. In panel B the total movement, i.e. the movement at all frequencies and with all phases, is overlaid as a color code on the B-mode image. The displacement magnitude is shown in the color bar to the right. Panel C shows the MMUS image. In this image, only pixels showing displacement with the same frequency and phase (± 0.35 radians) as the magnetic field are color coded and overlaid on the B-mode image. Note that the difference of the maximum displacement is more than 70 times larger for panel B than panel C.

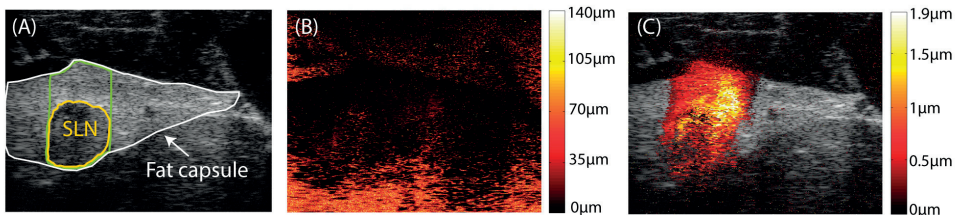


Figure 4. The SLN and surrounding fat capsule in animal 5. The images are obtained at electromagnet excitation voltage 5 Hz 60 V. Panel (A), B-mode ultrasound image where the SLN (yellow), the area where the MMUS displacement is calculated (green) and the fat capsule (white) are outlined. Panel (B), the total movement, i.e. the movement at all frequencies and phases, is superimposed as a color code on the B-mode image. Panel (C) MMUS image, displacement is only color-coded when occurring with the same frequency and phase (± 0.35 radians) as the magnetic field. The color-coding is overlaid on the B-mode image. Note that the maximum displacement magnitude is more than 70 times larger in panel (B) than panel (C).

In Fig.5, the MMUS images of the SLN and its surrounding fat capsule in animal 1, 2, 3 and 5 are shown. All images are obtained at 5 Hz 40 V electromagnet excitation voltage. No detectable MMUS displacement was found in animal 4 and 6. The images are color-coded with regard to displacement according to the color bar on the right hand side of each image. The mean (\pm standard deviation) magnetomotive displacement in the SLNs in the displayed cross sections was : $0.71 \pm 0.77 \mu\text{m}$ for animal 1, $0.87 \pm 0.64 \mu\text{m}$ for animal 2, $0.16 \pm 0.16 \mu\text{m}$ for animal 3 and $0.57 \pm 0.46 \mu\text{m}$ for animal 5. The mean (\pm standard deviation) magnetomotive displacement in each SLN (displacement in all cross sections and at all voltages) was: $0.78 \pm 0.29 \mu\text{m}$ for animal 1, $0.53 \pm 0.14 \mu\text{m}$ for animal 2, $0.21 \pm 0.10 \mu\text{m}$ for animal 3 and $0.56 \pm 0.14 \mu\text{m}$ for animal 5. Due to a technical failure only two cross sections were obtained in animal 5.

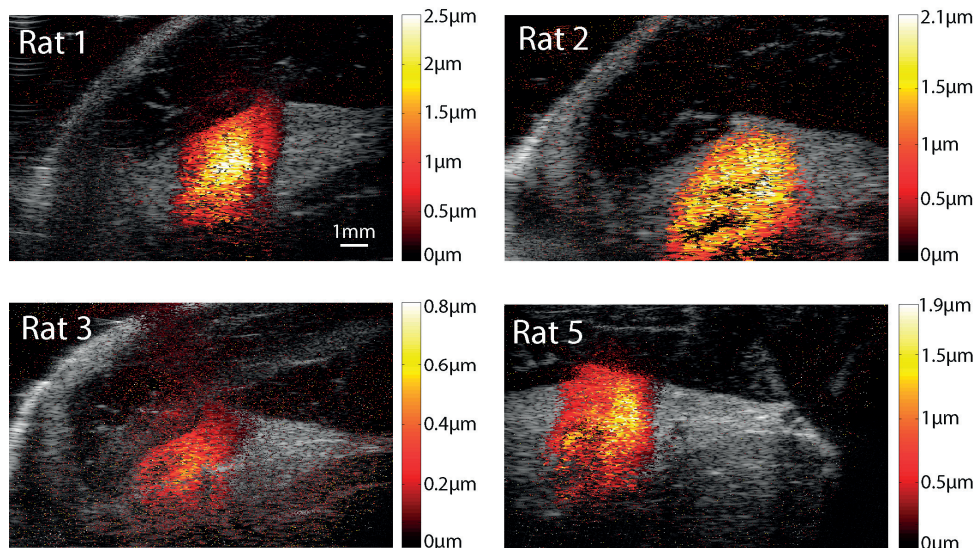


Figure 5. MMUS images of the SLN and its surrounding fat capsule in animal 1, 2, 3 and 5. All images are obtained at 5 Hz 40 V electromagnet excitation voltage. The color represents magnetomotive displacement according to the color bar to the right.

3.3 MR imaging

In Fig. 6, MR-images of the SLN and the control lymph node and their surrounding tissue (fat capsule and muscle tissue), are shown for animal 2 and 4. For all animals, the two nodes were placed in one Eppendorf tube and imaged with the MR scanner. The green arrow heads point at the SLNs whereas the yellow arrows point at the popliteal LN removed from the control side. The area of hypointense MRI signal in the SLN, shown as black, indicates the amount of SPIONs present. The black areas in between and around the excised tissues are a result of the air surrounding them.

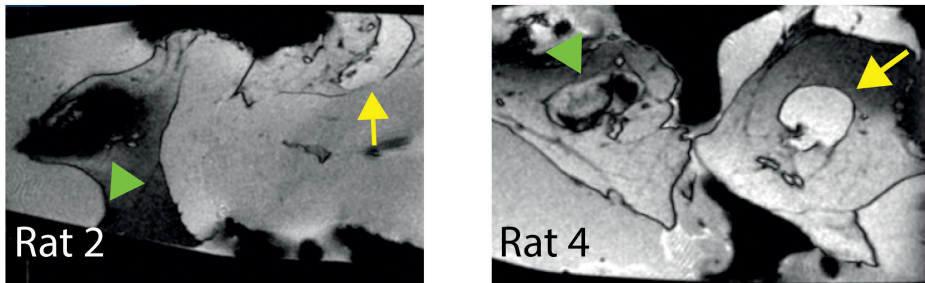


Figure 6. MR-images of the excised tissues containing removed SLN (green arrow head) and control node (yellow arrow) for animal 2 and 4. Both lymph node samples (and also some of their surrounding tissue) were placed in an Eppendorf tube during MRI acquisition. The SPIONs present in the SLN are shown as signal voids (black). The black areas around and in between the two tissue samples (lymph nodes and their surrounding tissue parts) stem from air pockets in the samples.

The magnitude of the MR-signal was in this study defined as the number of black pixels in the SLN at the cross section with the largest MR-hypoenhancement, obtained from the 3D volume built up of each lymph node sample. To compare MMUS and MRI, a correlation graph was made. The animals where MMUS displacement was found were correlated against the same animals' MRI signals. The result is shown as the linear part in Fig. 7, where the measurement values are displaced as *. The correlation coefficient, r , where calculated to 0.999 and the p-value to 0.001, which indicates a strong correlation between the two imaging modalities. The two animals, not detectable with MMUS, are displayed as Δ in the graph. These two values give an indication of the MMUS, which is denoted as a dash line in the graph.

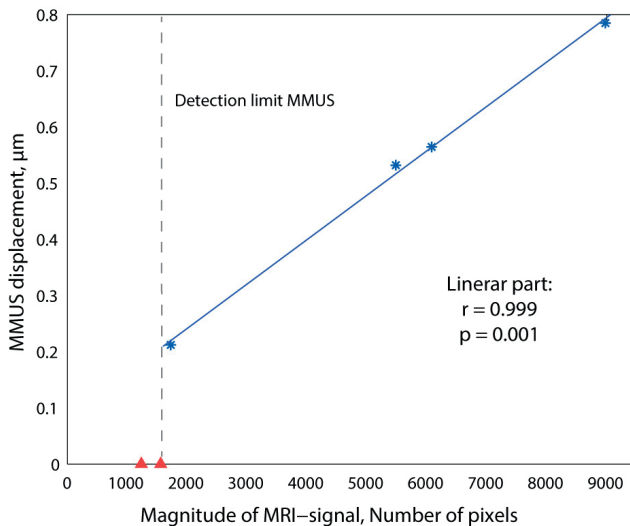


Figure 7. The graph shows the correlation between the MMUS and MRI signals for the four rats with detectable MMUS signal (the linear part). The measurement values are displayed as *. The two rats where no MMUS signal was found, are displayed as Δ in the graph, and give an indication of the detection limit of MMUS which is presented as a dashed line in the graph.

4. Discussion

To our knowledge, this study is the first of its kind where a multimodal imaging method with PET/CT and MRI is combined with MMUS. This combination of imaging modalities enables usage of hybrid PET/MR systems, with sensitive PET imaging and high resolution MRI followed later by MMUS intraoperatively.

We here used imaging of SLNs to prove the multimodality technique in a clinically relevant situation. The results from this SLN *in vivo* study show that it is possible to perform multimodal imaging with PET, MMUS and MRI in the same animal using ^{68}Ga -labeled SPIONs. Our suggested hypothetical clinical scenario, where PET/CT imaging was performed one hour after nanoparticle injection followed by MMUS imaging either two or four days later, was successful. The sentinel lymph nodes in all six animals were detectable with PET, and the MMUS and MRI measurements were in correlation.

4.1 PET

The SLN could clearly be detected in all six animals in the PET/CT images. After the nanoparticle injection, the animals were awake for one hour before the PET scan was performed. Since lymph flow is, to a large degree, propelled by contraction of adjacent skeletal muscles, large variation in lymph node accumulation can be expected as seen in Fig. 3. The mean activity uptake (\pm standard deviation) in the SLNs was found to be $2.6 \pm 2.9\%$. This is in compliance with other published data on SLN accumulation of injected nanoparticles/colloids [7].

4.2 MMUS/MRI

In the animals where MMUS displacement could be detected, the results were in strong correlation with the results from the MRI scans (Fig. 5-7) (correlation coefficient=0.999 and a p-value=0.001). In turn, the MR-images revealed that the concentration of SPIONs was lowest in the two animals' SLNs where no MMUS signal was observed. The concentration of nanoparticles in animal 4 and 6 is most probably not large enough to set the nanoparticles' surrounding tissue in detectable MMUS motion. This kind of concentration threshold has been reported previously [15, 18] and in Fig. 5, this detection limit is denoted as a dashed line. One way to lower the threshold value is probably to apply a stronger magnetic field and thereby increase the magnetic force acting on the nanoparticles. Another way could be to use nanoparticles with a higher susceptibility.

Additionally, animal 4 received the injection with the lowest particle concentration and for animal 6, there was a leakage to the blood, as seen in the elevated liver uptake in the PET image. These two parameters are most probably partly responsible for the lower SPION concentration in these animals' SLNs.

The animals in the group injected 4 days before the MMUS examination (animal 1, 2 and 3) were all successfully imaged with MMUS whereas only one animal (animal 5) in the group injected 2 days before could be imaged with MMUS. It can be argued that this is a result of the particles not having enough time to migrate to the SLN. Yet from previous studies, we have established that the period between injection and imaging allowed in this study is more than sufficient for SLN uptake [7, 19-21]. The reason is most probably due to the low concentration injected in animal 4 and the liver uptake in animal 6. The concentration of SPIONs in the injected volume was also highest for animal 1 and 2, which affect the result as well.

This study has shown the potential of the MMUS technique as a candidate for multimodal imaging together with PET and MRI. To make the technique more suitable for clinical use, a new probe design that would facilitate the magnetic field excitation is under development.

By labeling the nanoparticles with targeting molecules, e.g. antibodies or peptides, the particles could also be used for target specific molecular imaging. A new dimension of possibilities and field of applications would then open up for the MMUS technique.

5. Conclusion

In this study, we have for the first time, to our knowledge, presented a multimodal imaging method where PET/CT and MRI was used in combination with MMUS. To prove the technique in a clinical relevant situation, we have imaged sentinel lymph nodes, where ⁶⁸Ga-labeled SPIONs were utilized as a multimodal contrast agent. The combination of imaging modalities is a proof of concept for whole body screening of patients with PET/MR, whereas localized non-invasive imaging thereafter can be performed bedside with the MMUS.

Acknowledgement

This study was supported by grants from the Kamprad Family Foundation, VINNOVA, The Swedish Research Council, The Knut and Alice Wallenberg foundation. Lund University Bioimaging Center (LBIC), Lund University is gratefully acknowledged for providing experimental resources.

References

- [1] T. Beyer, D. W. Townsend, T. Brun, P. E. Kinahan, M. Charron, R. Roddy, J. Jerin, J. Young, L. Byars, and R. Nutt "A Combined PET/CT Scanner for Clinical Oncology", *J Nucl Med Mol*, 2000; 41; 1369-1379
- [2] A. W. Sauter, H. F. Wehrle, Ar. Kolb, Ma. S. Judenhofer and B. J. Pichler, "Combined PET/MRI: one step further in multimodality imaging", *Trends in Molecular Medicine*, 2010;16; 508-515
- [3] T. Beyer, D. W. Townsend, J. Czernin, L. S. Freudenberg, "The future of hybrid imaging—part 2: PET/CT", *Insights Imaging* 2011; 2; 225–234
- [4] T. Jansson, S. Andersson-Engels, S. Fredriksson, F. Ståhlberg, S. E. Strand, "Superparamagnetic iron oxide nanoparticles as a multimodal contrast agent for up to five imaging modalities" *Clin Transl Imaging*, 2015; 3: 247–249
- [5] J. Oh, M. D. Feldman, J. Kim, C. Condit, S. Y. Emelianov, and T. E. Milner, "Detection of magnetic nanoparticles in tissue using magneto-motive ultrasound," *Nanotechnology*, 2006; 17: 4183–4190
- [6] G. Bao, S. Mitragotri, and S. Tong, *Multifunctional nanoparticles for drug delivery and molecular imaging*. *Annu Rev Biomed Eng*, 2013. 15: p. 253-82
- [7] R. Madru, T. A Tran, J. Axelsson³, C. Ingvar⁴, A. Bibic, F. Ståhlberg, L. Knutsson, S. E. Strand, "⁶⁸Ga-labeled superparamagnetic iron oxide nanoparticles (SPIONs) for multi-modality PET/MR/Cherenkov luminescence imaging of sentinel lymph nodes", *Am J Nucl Med Mol Imaging* 2014; 4:60-69

- [8] R. Madru, P. Kjellman, F. Olsson, K. Wingårdh, C. Ingvar, F. Ståhlberg, J. Olsrud, J. Lätt, S. Fredriksson, L. Knutsson, S. E. Strand, "99mTc-Labeled Superparamagnetic Iron Oxide Nanoparticles for Multimodality SPECT/MRI of Sentinel Lymph Nodes", *J Nucl Med* 2012; 53: 459-463
- [9] M. Mehrmohammadi, J. Oh, S. Mallidi, S. Y. Emelianov, "Pulsed Magneto-motive Ultrasound Imaging Using Ultrasmall Magnetic Nanoprobes", *Molecular Imaging*, 2011; 10: 102–110
- [10] A. G. Pope, G. Wu, F. Y. McWhorter, E. C. Merricks, T. C. Nichols, T. J. Czernuszewicz, C. M. Gallippi, A. L. Oldenburg, "Contrast-enhanced imaging of SPIO-labeled platelets using magnetomotive ultrasound", *Phys Med Biol.* 2013; 58: 7277–7290
- [11] J. Buscombe, G. Paganelli, Z. E. Burak, W. Waddington, J. Maublant, E. Prats, H. Palmedo, O. Schillaci, L. Maffioli, M. Lassmann, C. Chiesa, E. Bombardieri, and A. Chiti, "Sentinel node in breast cancer procedural guidelines," *Eur. J. Nucl. Med. Mol. Imaging*, 2007; 34: 12: 2154–2159
- [12] E.C. Hsueh, A.E. Giuliano, "Sentinel Lymph Node Technique for Staging of Breast Cancer", *Oncologist* 1998;3:165-170.
- [13] A.H. Chakera, B. Hesse, Z. Burak, J.R. Ballinger, A. Britten, C. Caraco, et al. "EANM-EORTC general recommendations for sentinel node diagnostics in melanoma", *Eur J Nucl Med Mol Imaging* 2009;36:1713-1742.
- [14] S.K. Somasundaram, D.W. Chicken D.W, M.R. Keshtgar, "Detection of the sentinel lymph node in breast cancer". *Br Med Bull*, 2007; 84; 117-131
- [15] M. Evertsson, M. Cinthio, S. Fredriksson, F. Olsson, H. W. Persson, and T. Jansson, "Frequency- and phase-sensitive magnetomotive ultrasound imaging of superparamagnetic iron oxide nanoparticles," *IEEE Trans. Ultrason. Ferroelectr. Freq. Control*, 2013; 60: 481–491
- [16] T. Jansson, M. Evertsson, E. Atilé, R. Andersson, S. Fredriksson, H. W Persson, I. Svensson, M. Cinthio, "Induced tissue displacement in magnetomotive ultrasound imaging - simulations and experiments", in Proc. IEEE Ultrasonics Symp., 2014; 639-642
- [17] C.A. Schneider, W.S. Rasband, K.W. Eliceiri, "NIH Image to ImageJ: 25 years of image analysis". *Nature Methods*, 2012; 9: 671-675
- [18] M. Mehrmohammadi, J. Oh, S. Aglyamov, A. Karpiouk, and S. Y. Emelianov, "Pulsed magneto-acoustic imaging," in *Proc. 31st Annu. Int. IEEE Engineering in Medicine and Biology Society Conf.*, 2009; 4771–4774.
- [19] M. Evertsson, P. Kjellman, M. Cinthio, S. Fredriksson, R. in 't Zandt, H. W. Persson, and T. Jansson, Multimodal Detection of Iron Oxide Nanoparticles in Rat Lymph Nodes Using Magnetomotive Ultrasound Imaging and Magnetic Resonance Imaging" *IEEE Trans UFFC*, 2014; 61: 1276-1283
- [20] M. Evertsson, M. Cinthio, P. Kjellman , S. Fredriksson, R. Andersson, H. Toftevall, H. W Persson, T. Jansson, "*In vivo* magnetomotive ultrasound imaging of rat lymph nodes – a pilot study", in Proc. IEEE Ultrasonics Symp., 2015.
- [21] P. Kjellman, R. in 't Zandt, S. Fredriksson, SE. Strand,"Optimizing retention of multimodal imaging nanostructures in sentinel lymph nodes by nanoscale size tailoring." *Nanomedicine*, 2014 Jul; 10, 1089-1095



LUND UNIVERSITY

ISBN: 978-91-7623-745-8 (print)

ISBN: 978-91-7623-746-5 (pdf)

ISRN: LUTEDX/TEEM – 1103 – SE

Report-nr: 4/16